# ACTIVE TISSUE EQUIVALENT DOSIMETER:

# DEVELOPMENT OF A DOSIMETER FOR THE

# INTERNATIONAL SPACE STATION

By

OLIVER IAN CAUSEY

Bachelor of Science in Physics
The University of Tulsa
Tulsa, OK
2014

Submitted to the Faculty of the
Graduate College of the
Oklahoma State University
in partial fulfillment of
the requirements for
the Degree of
DOCTOR OF PHILOSOPHY
July, 2018

ACTIVE TISSUE EQUIVALENT DOSIMETER:

DEVELOPMENT OF A DOSIMETER FOR THE

INTERNATIONAL SPACE STATION

Dissertation Approved:

Eric Benton

Dissertation Adviser

Mario Borunda

Joe Haley

Andy Arena

ACKNOWLEDGEMENTS

There are not enough pages and there is not enough time to give thanks to everyone that made this project possible. This project could not have been completed without the efforts of many people. I would first like to thank everyone that had a direct impact on the project.

First, I would like to acknowledge Eric Benton for advising me throughout this project. No one can describe exactly what an adviser does for a doctoral student. However, anyone that has committed years of their life to one of these projects knows that an adviser cannot be thanked enough.

Art Lucas has been a huge part of this project. In many ways, this project is due to art. His ideas helped realize the commercial use of TEPC many decades ago. His insights helped me bring this project its current state.

Barb Lucas was a huge help throughout the design phase of ATED. Her insights into electromagnetic interference produced significant noise reduction in ATED.

The Physics and Chemistry instrument shop personnel are owed thanks for all of the hard work they put into ATED. Larry Vaughn, in particular, helped me overcome design hurdles throughout the years. This project could not have been completed without the shop and everyone there.

I owe a great deal of gratitude to the personnel at the National Institute of Radiological Sciences. The beam time at HIMAC was essential in bringing me to an understanding of electronics and the use of TEPC. This project could not have been completed were it not for all of the help we received in Japan.

Much thanks is owed to Buddy Gersey. He drove hundreds of miles to teach our group how to analyze TEPC data properly. He proved himself priceless when the original model was lost in an accident on a FedEx truck. He called me and taught me a calibration technique for TEPC over the phone. ATED's launch to the space station would have been delayed months if it were not for Buddy.

The personnel at LANSC helped at the beginning of this project when they granted us beam time for the early ATED prototype. Measuring neutron spectra at a high energy spallation source is a unique experience.

Michael Sprague from XP Power helped significantly during the power system

design process for ATED.

Jim Norton from Custom Products & Services helped significantly during the materials design for the gassing system of ATED.

People from my personal life should be thanked as well. I would not have made it this far without the following people.

Thank you, Jean Causey (née Rees) and John Causey for producing me and guiding through my younger years. My curiosity was inspired early in my life.

Thank you, JoAnn Causey (née Barmann) for ensuring that I made it this far in life.

I would like to thank Alesia Balch (née Green) for watching my son during the first six months of his life so that I could finish this project.

Thank you, Maurie Balch, for everything you have done to help me through this project. You supported me through the most challenging parts of putting a detector on the International Space Station.

Thank you, Apollo Causey. You have been my inspiration for some time now.

Name: OLIVER CAUSEY

Date of Degree: JULY, 2018

Title of Study: ACTIVE TISSUE EQUIVALENT DOSIMETER: DEVELOPMENT OF A DOSIMETER FOR THE INTERNATIONAL SPACE STATION

Major Field: PHYSICS

A Tissue Equivalent Proportional Counter (TEPC) named the Active Tissue Equivalent Dosimeter (ATED) has been developed to measure absorbed dose from radiation on the International Space Station (ISS) and at aviation altitudes on commercial aircraft. The astronauts on the ISS and people in aircraft are exposed to the higher-than-normal absorbed dose rates from radiation. Galactic Cosmic Rays (GCR), Solar Energetic Particles (SEP) from Solar Particle Events (SPE), and the particles trapped in Earth's magnetic field pose the most risk for an increase in absorbed dose rates from radiation for astronauts on the ISS. There are very few tissue equivalent dosimeters on the ISS. There are controversial claims that Solar Particle Events (SPE) during solar storms and Terrestrial Gamma Flashes (TGF) during thunderstorms can cause dangerously high-absorbed dose rates for aircrew and passengers on commercial airlines. There are currently no radiation monitors on commercial aircraft in the United States. We have designed ATED to address these concerns. Extensive in-house design and redesigns of subsystems were required to ensure the system was robust enough to handle space flight. This development included methods for noise reduction, writing software, creating hardware to make the system fully embedded/stand-alone, and implementing Commercial-off-the-Shelf (COTS) parts. Adhering to NASA's strict safety guidelines required extensive testing at NASA's Johnson Space Center (JSC). The testing at JSC included characterization of radiation emission by ATED, characterization of transient signals from ATED to the ISS power source, and characterization of power conditions under which ATED can operate. Development of the unit also required extensive calibration and characterization using the Heavy Ion Medical Accelerator in Chiba, Japan (HIMAC). ATED launched to the ISS on the Orbital ATK resupply mission OA-9 on May 21, 2018. The resupply vessel docked to the ISS on May 24, 2018. The first data was transmitted down from ISS on July 19, 2018.

TABLE OF CONTENTS

Content Page

LIST OF TABLES

Table Page

LIST OF FIGURES

Figure Page

Figure Page

Figure Page

Figure Page

Figure Page

# CHAPTER I

## INTRODUCTION

A tissue equivalent proportional counter (TEPC) named the Active Tissue Equivalent Dosimeter (ATED) has been developed to measure the absorbed dose rates and dose equivalent rates from ionizing radiation in the atmosphere at aviation altitudes and in Low-Earth Orbit (LEO) on the International Space Station (ISS). This unit is a stand-alone fully embedded system created to help assess the health risks associated with radiation.

Exposure to elevated levels of ionizing radiation leads to increased health risks, including the risk of cancer, cataracts in the eyes, and in extreme exposures acute radiation sickness and death. Two careers with higher-than-normal absorbed dose rates from radiation are astronauts and aircrew on commercial aircraft [Tobiska 2014, Fry 1989]. There are no procedures in place to measure or track absorbed dose from the ionizing radiation at aircraft altitudes in the United States. There are many radiation detectors on the ISS [Dachev 2017, Pinsky 2014, Szanto 2015, Smith 2016, Kroupa 2015, Badavi 2011, Zaconte 2010, Berger 2017, Arimoto 2018, Benton 2001, Badhwar 2002].

However, there are currently a limited number of tissue equivalent radiation monitoring units on the ISS. Having few tissue equivalent radiation monitors on ISS is undesirable since local shielding environments cause absorbed dose rates to differ on the ISS by more than a factor of two depending on location [Badhwar 1997].

There are three main sources of ionizing radiation ATED is measuring in LEO: Galactic Cosmic Rays (GCR), trapped ions in the Van Allen belts, and Solar Particle Events (SPE) [Dachev 2017]. GCR come from outside the solar system [Fry 1989]. The low energy GCR are attenuated by the complex magnetic structures and solar wind within the solar system. Significant protection from GCR in LEO comes from the geomagnetic field [NCRP98 1989]. However, the structure of the geomagnetic field creates a region known as the South Atlantic Anomaly (SAA) that traps particles in LEO with enough energy to increase absorbed dose rates in LEO [Badhwar 1997]. An SPE is unlikely to be measured during this project because the sun is currently in a period of low activity [Schwadron 2017].

However, an SPE could cause acute radiation sickness in astronauts if a strong enough event occurs during a space mission. The short-term effects of ionizing radiation are induced by relatively high radiation doses over a short period. The symptoms include, but are not limited to, reddening of the skin, nausea, the death of frequently dividing cells (such as those in the intestinal lining and hair), headaches, loss of the ability to focus, and many others. These symptoms may eventually lead to death if the dose is high enough. NASA is most concerned with the astronauts' long-term cancer risks associated with the increased absorbed dose from radiation because the long-term risks are more likely occur [NCRP98 1989].

The main sources of absorbed dose from radiation at aviation altitudes are secondary particles, mostly neutrons, caused by the primary particles from GCR and solar wind interacting with the atmosphere and matter in aircraft. There are reasons to believe that solar energetic particles from Solar Particle Events (SPE) could contribute significantly to absorbed dose rates during these rare events [Reedy 1996]. There are also controversial claims that Terrestrial Gamma ray Flashes (TGF) produced in thunderstorms can generate dose equivalents as high as 0.1 Sv [Dwyer 2005]. 0.1 Sv is five times the recommended annual limit for absorbed dose [ICRP60 1991]. Such claims have yet to be investigated via systematic measurements. ATED could substantiate or discredit these claims by measuring absorbed dose in aircraft.

Absorbed dose, *D*, is calculable from measurements made by ATED. ATED is designed to measure lineal energy, *y*, which is the energy deposited in the active volume of the detector by ionizing radiation [Brackenbush 1990]. ATED's active volume has a response to ionizing radiation similar to the response that living tissue has to ionizing radiation [Rossi 1996]. The spectrum from ATED has three major components: counts from radiation, noise, and the clipping region. Nearly all of the noise has been eliminated by impedance matching and implementing a star ground in the unit. The system was optimized to maximize the range of measurable lineal energy between the noise and clipping regions.

ATED was designed and constructed at Oklahoma State University. The unit consists of a detector head, a multi-channel analyzer (MCA), a Gaussian shaping amplifier, two AC-to-DC low voltage power supplies, a high voltage power supply, a Raspberry Pi 3 computer, and the unit housing. The operating system and MCA software are originally open source. Both the operating system and MCA software were edited extensively to make this system

fully automated. Other supporting software was also written to support automation and create an embedded system to allow the system to run self-sufficiently on ISS.

Calibration experiments were necessary to ensure proper functioning of the ATED unit. The first set of experiments took place at Los Alamos National Laboratory (LANL). These measurements were taken to test the power distribution of ATED and to gain a general understanding of TEPC measurement techniques. Electrical characterization of the gaussian amplifier circuit took place at Oklahoma State University (OSU). Gain settings for the detector head were calibrated at the Heavy Ion Medical Accelerator in Chiba (HIMAC) in Japan in February 2017. Beam exposures for absorbed dose characterization took place at HIMAC in Japan in June 2017.

Demonstration of the unit as a radiation dosimeter in a complex mixed radiation field is the final goal of the project. ATED was successfully launched to the ISS in May 2018. Data from this experiment will demonstrate the capabilities of the ATED unit by comparing ATED measurements to other radiation monitors on the ISS. ATED measured data will also be compared to calculations using radiation transport modeling software. Altitude dependence of absorbed dose rate in the SAA will be examined using measurements from ATED. The absorbed dose rate from low energy electrons at high latitudes will be examined using ATED data.

# CHAPTER II

## RADIATION ENVIRONMENTS AND DOSIMETRIC DEFINITIONS

### *2.1 Radiation in LEO*

The radiation environment in Low-Earth Orbit (LEO) and in the atmosphere are complicated fields. LEO has three main sources: Galactic Cosmic Rays (GCR), Solar Particle Events (SPE), and the trapped radiation belts [NCRP98 1989]. The radiation environment in the atmosphere has two main sources: GCR and SPE. The following sections describe the radiation environments in LEO and in the atmosphere at aviation altitudes.

#### *2.1.1 Galactic Cosmic Rays*

Galactic cosmic rays (GCR) are fully ionized nuclei believed to be accelerated by the turbulent magnetic fields in shock waves created during supernova explosions [Cronin 1997]. GCR composition has been measured to be approximately 85% protons, 12% helium ions, 2% electrons and positrons, and 1% heavier ions [NCRP98 1989]. The distribution of GCR is considered nearly isotropic in near-Earth space. GCR achieve energies up to $10^{21}$ eV, but particles with such high energies are extremely rare [Cronin 1997]. The GCR spectrum has a broad peak at approximately 1 GeV within the heliosphere near Earth [NCRP98 1989]. GCR is responsible for approximately half of the

absorbed dose from radiation in the ISS orbit [Badhwar 2002].

Low energy GCR is attenuated by the solar wind [NCRP98 1989]. Figure 2.1 shows the effect that the solar wind cycle has on GCR. The intensity of solar wind is periodic, i.e., the solar cycle, with minima and maxima each occurring every eleven years [NCRP98 1989]. The higher flux of the solar wind during solar maximum attenuates the flux of the incoming low energy GCR because of the increased interactions with GCR [Zhao 2014]. There is a higher overall flux of GCR near Earth during solar minima because of the decreased interaction with the solar wind [Schwadron 2017].

Low energy GCR is deflected by the magnetic field near Earth [Badhwar 2001]. The magnetic field near Earth has a complicated structure: in its most basic form, the geomagnetic field can be approximated as a dipole but possesses higher order moments as well [Shcherbakov 2015]. The Sun's magnetic field, carried along with the solar wind, interacts with the geomagnetic field in ways that increase the complexity of the field, stretching it out into a teardrop shape [Smart 2009]. Figure 2.2 shows a simplified representation of the complex Earth-Sun interaction.

The Earth's magnetic field offers significant protection from radiation in LEO by deflecting low energy GCR away from the magnetic equator [ICRP 2001]. The Geomagnetic Cutoff Rigidity, *R*, in units of gigavolts or GV, characterizes the deflection effect that the geomagnetic field has on GCR [Smart 2009]. Rigidity of a particle is a measure of a particle's resistance to deflection by a magnetic field given by Equation 2.1:

$$R = \frac{p}{q}, \tag{2.1}$$

where $p$ is the momentum of the particle and $q$ is the charge of the particle. Cutoff rigidity is the minimum value of rigidity a particle must possess to overcome deflection by the local magnetic field [Smart 2009]. The Geomagnetic Cutoff Rigidity changes with the location because the geomagnetic field varies with location. The Geomagnetic Cutoff Rigidity also varies in time because the geomagnetic field is constantly changing [Smart 2006]. Figure 2.3 is a map of the Geomagnetic Cutoff Rigidity calculated for two epochs. The calculations shown in Figure 2.3 show both spatial and temporal dependence of the Geomagnetic Cutoff Rigidity. The rigidity is highest near the Earth's equator because the geomagnetic field is nearly parallel to the Earth's surface at the equator. The parallel field deflects incoming ions more than anywhere else in the field. Charged particles normally incident to the geomagnetic field below the energy defined by the geomagnetic cutoff rigidity are attenuated; only high energy GCR penetrate the geomagnetic field at low latitudes [Smart 2009].

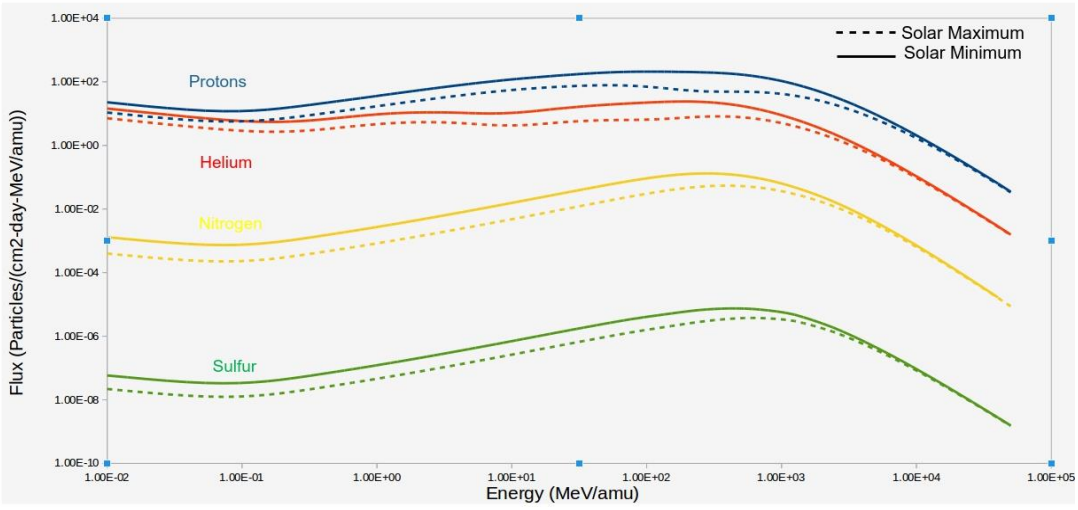


Figure 2.1: 10 day GCR energy spectra flux affected by the solar cycle for protons, Helium, Nitrogen, and Sulfur. The plotted data is from the solar 2010 solar minimum and the 2001 solar maximum. Significant attenuation occurs at GCR energies below ~ 1 GeV/amu during solar maxima. [Badhwar1997].

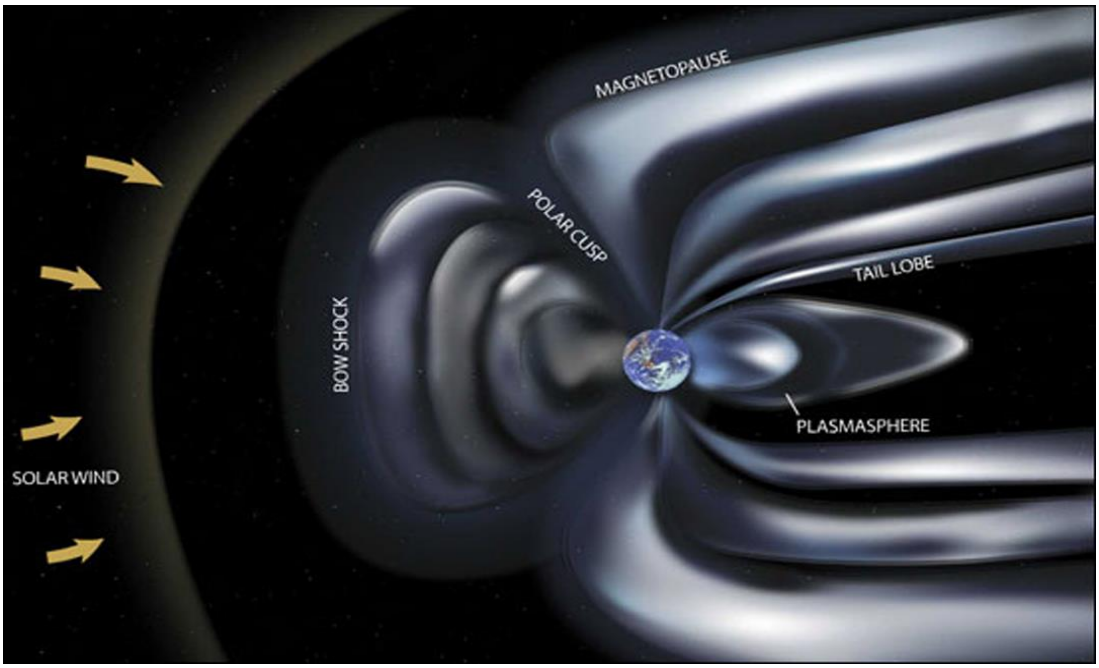

Figure 2.2: The Earth-Sun magnetic interaction increases the complexity of the already complex geomagnetic field. The field is approximately parallel to the surface of the Earth at the equator. [NASA 2006]

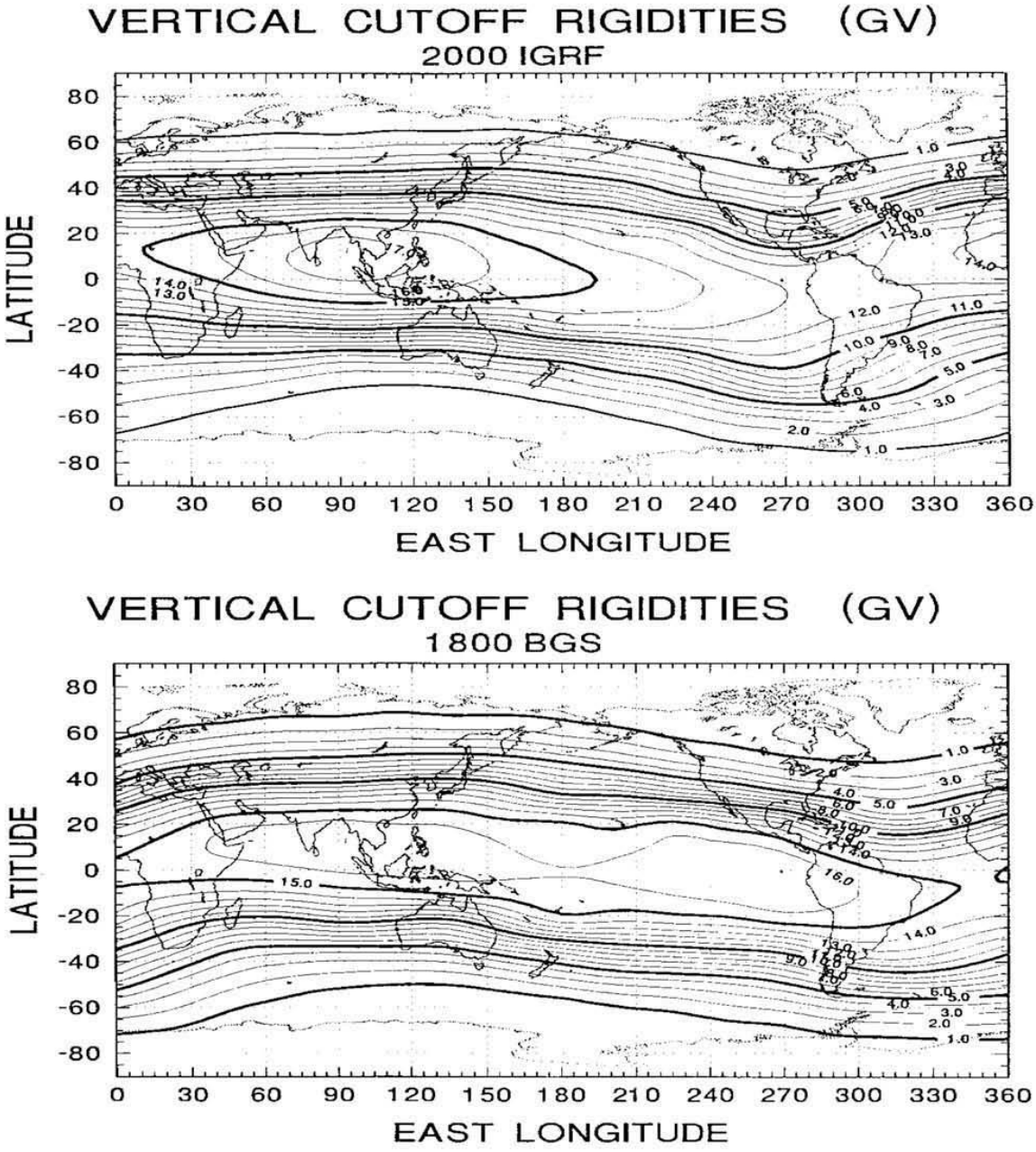


Figure 2.3: Contour plots of Geomagnetic Cutoff Rigidities for the 1800 and 2000 epochs. Each contour is separated by increments of one GV. Note the increasing value towards the equator (zero degrees latitude). The cutoff values shift with external magnetic fields. Solar events can cause shifts over time scales on the order of hours or less [Smart 2009].

### *2.1.2 Trapped Radiation Belts in LEO*

There are two main regions in the geomagnetic field that trap energetic charged particles: the inner radiation belt and the outer radiation belt [Mcelroy 1975, Van Allen 1959].

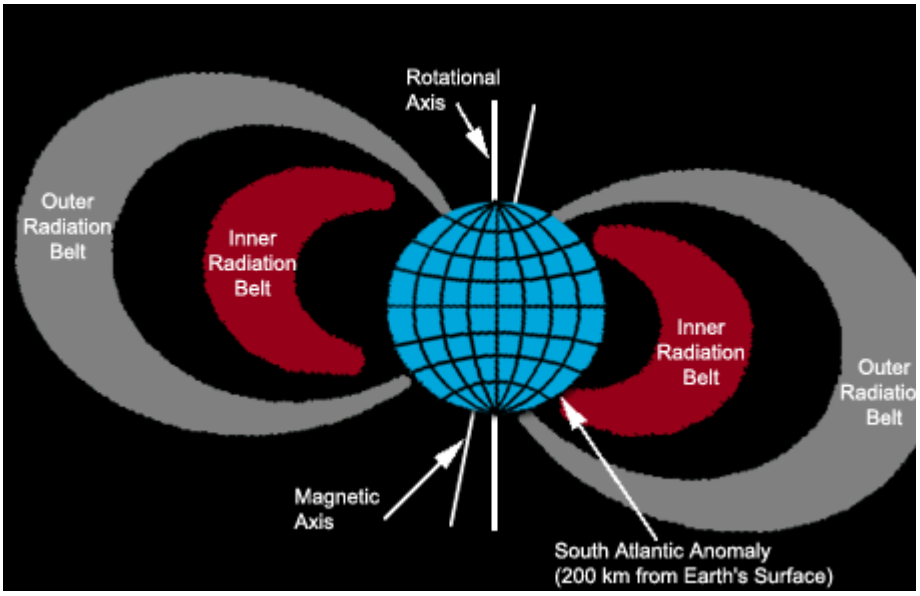


Figure 2.4: Cross-sectional representation of the two main belts associated with the geomagnetic field. Note the SAA penetration into the ISS LEO [Srag 2016].

#### *2.1.2.1 The Inner Radiation Belt*

The inner belt consists of mainly two types of particles: electrons with energies up to <1 MeV and protons with energies up to ~250 MeV [Fennel 2015, Badhwar 1997]. The inner radiation belt ranges from an altitude of approximately 1000 km to 6000 km [Mcelroy 1975]. However, the inner radiation belt reaches altitudes as low as 200 km at the South Atlantic Anomaly (SAA), as shown in Figure 2.4. Previous measurements have shown that roughly 50% of absorbed dose from radiation in the ISS orbit comes from protons in the SAA [Badhwar 2002]. The density of particles in the SAA increases exponentially with altitude [Benton 2001]. The ISS is constantly losing altitude because

of atmospheric drag. The loss in altitude requires regular increases in altitude to keep the station in orbit. ATED will measure the changes in absorbed dose rate associated with the changes in altitude as the station's orbit pass through the SAA will be measured by ATED.

*2.1.2.2 The Outer Radiation Belt*

The outer belt consists of mainly electrons of energies ranging from 0.1 to 10 MeV [Lugaz 2016]. The electrons contribute to absorbed dose at high latitudes in the cusps of the magnetic field [Badhwar 1997]. A scientific goal of ATED is to measure the dosimetric quantities from the electrons at high latitudes.

*2.1.3 Solar Particle Events (SPE)*

The magnetic fields on the sun's surface are more active during solar maximum than at any other time; SPE are expected to occur mostly during solar maximum [Reedy 1996]. There are two types of SPEs: those associated with solar flares and those caused by Coronal Mass Ejections (CME) [Benton 2001].

Flare events are rich in electrons of energy < 100 keV, are short-lived and follow the Interplanetary Magnetic Field (IMF) lines. IMF lines are the spiral-shaped portion of the solar magnetic field that is trapped in the outward moving solar wind, as depicted in Figure 2.5.

The other main source of ionizing radiation in LEO comes from the sun in the form of Solar Energetic particles associated with CME. Many complex magnetic structures exist internal and external to the Sun's surface. During a CME, the motion of these

magnetic fields accelerate ions and the magnetic fields on or near the surface of the sun. The accelerated ions and magnetic fields reach high enough energies to penetrate into LEO and add to absorbed dose rates in on the ISS and in the Earth's atmosphere. The CME events are dominated by large fluxes of protons with energies > 1 MeV. The CME events are more gradual than the flare events and travel perpendicularly to the IMF lines [Turner 2000].

Measuring an absorbed dose rate from an SPE would be very exciting because SPE are rare. However, the sun is currently in an extremely "quiet" solar minimum [Schwadron 2017]. It is expected that an absorbed dose measurement from SPE is unlikely during the ATED experiment.

*Figure 2.5: Artist rendering of IMF. IMF is the portion of the solar magnetic field that propagates through the solar system as solar wind traps it in an outward motion [SIDC 2015].*

### *2.1.4 Secondary Particles*

Most of the energy lost by primary particles traversing a medium occurs via two types of interactions: ionization of the medium and nuclear interactions. The space radiation environment contains particles with energies high enough to produce secondary particles upon nuclear interaction with matter. Target fragmentation and projectile fragmentation produce secondary particles [ICRU28 1978].

As shown in Figure 2.6, target fragmentation occurs in an interaction between an energetic nucleon and a stationary nucleus in the spacecraft, its contents, or in an astronaut. The energetic nucleon can be a primary particle (GCR, trapped proton, or a solar particle) or a secondary particle from a previous interaction. The resultant secondaries are dependent upon the energy, cross section, and constituents of the incident nucleus as well as the constituents of the target nucleus [ICRU28 1978].

As depicted in Figure 2.7, projectile fragmentation occurs when a high-energy heavy ion is incident on a stationary target nucleus. Similar to target fragmentation, the different parameters (nuclei compositions, cross section, or energy) of the interaction can lead to different types of resultant secondary particles.

The secondaries from both target fragmentation and projectile fragmentation propagate and can lead to further interactions in the spacecraft and in astronauts. The production of secondary particles leads to a very complicated radiation environment within the spacecraft; more dosimeters on ISS would greatly increase the understanding of the complex radiation environment in which the astronauts live.

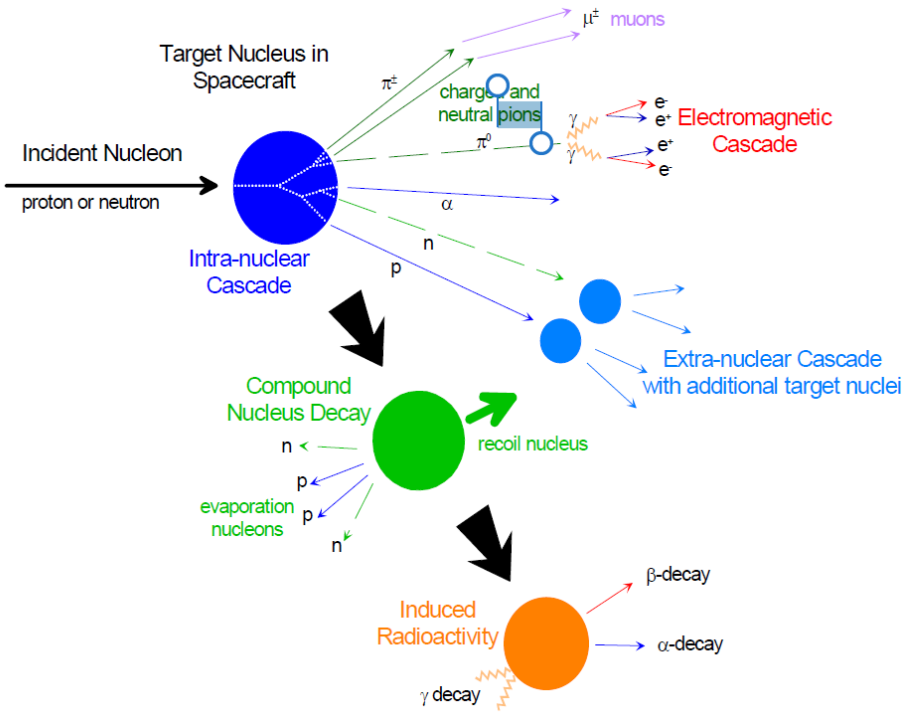


Figure 2.6: A depiction of target fragmentation. An incident particle undergoes a nuclear interaction with a nucleus in the medium in the space station [Benton 2004].

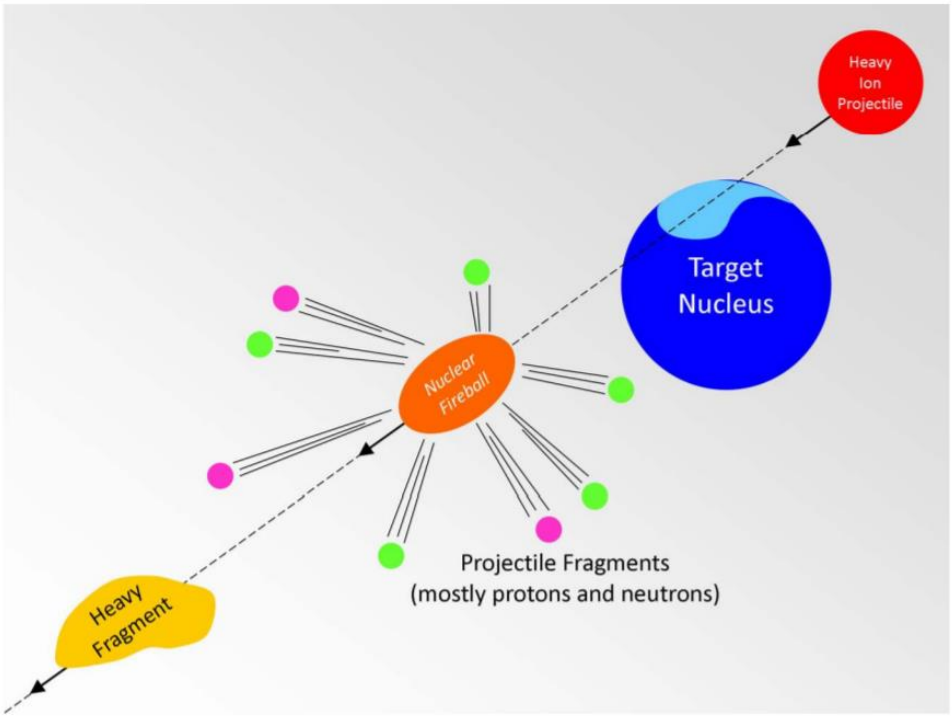


Figure 2.7: Projectile fragmentation of an HZE particle interacting with a stationary nucleus [DeWitt 2011].

## *2.2 Radiation at Aircraft Altitudes*

### *2.2.1 Extra-Terrestrial Radiation Sources*

Most of the absorbed dose from radiation at aviation altitudes is due to GCR and solar charged particles interacting with the Earth's magnetosphere and atmosphere. Dose equivalent rates at altitudes between 11 km and 13 km have been modeled to be as high as 10 µSv/h [Reitz 1993]. With the ICRP recommended annual dose equivalent of 20 mSv, these dose rates can be reached with approximately 2000 hours of flight time [ICRP60 1991]. This would require eight hours a day for five days a week year-round to achieve these limits. This many hours at altitude never occur for flight crew. However, solar energetic particles from SPE pose a potential risk that has yet to be measured at aircraft altitude [Reitz 1993]. Models of terrestrial gamma flashes (TGF) have shown potential risks for aircrew at aviation altitudes [Dwyer 2005]. Future ATED models will measure true absorbed dose rates and dose equivalent rates from SPE and test the claims of TGF.

SPE enhancement at aircraft altitudes has a potential for increased absorbed dose rates for people on airplanes. SPE spectra have been measured in LEO but not at aircraft altitudes. There may be increased risk to aircrew from the increased flux of high LET particles during SPE. Hardening of the SPE spectrum from interactions with the atmosphere increases absorbed dose rates from SPE [NCRP98 1989, Reitz 1993].

Radiation interactions with the atmosphere can be modeled using radiation interactions with water. We have calculated the shielding from atmosphere at aviation

altitudes to be equivalent to approximately 61 cm water. Depending on the Z and energy of incident radiation, this thickness of atmosphere can have differing effects. These effects can range from completely stopping all primary and secondary particles for lower energy particles to increasing the absorbed dose rates from high-energy particles at aviation altitude [Reitz 1993, ICRU28 1978].

*2.2.2 Terrestrial Radiation Sources: Terrestrial Gamma-Ray Flashes (TGF)*

Terrestrial gamma-ray flashes (TGF) are high-energy bursts of gamma-rays that occur during lightning storms [Gjesteland 2010]. TGF were first discovered in 1997 by the Burst and Transient Source Experiment (BATSE) on the Compton Gamma Ray Observatory (CGRO) satellite and have since been measured by other means [Grefenstette 2008]. Current models show that these gamma-ray bursts can be produced in large electric fields that can be attributed to storm clouds [Gjesteland 2010, Grefenstette 2008, Dwyer 2005]. Models have also shown that people in aircraft near a gamma-ray burst are exposed to dose equivalents as high as 0.1 Sv. [Dwyer 2010]. 0.1 Sv is five times the recommended dose equivalent by the ICRP [ICRP60 1991]. This claim is highly controversial and probably can only be addressed by systematic empirical measurements.

There are currently no data to substantiate or discredited the models. Flying ATED or future models of this TEPC on commercial, military, or business aircraft would generate data that will test these models. Newer models will be flown on aircraft until there is enough measured data to statistically analyze dosimetric quantities and their rates at aviation altitude due to TGF.

*2.3 Definitions of Dosimetric Quantities*

The definitions in section 1.2.1 are extensions of terms as defined by the International Commission on Radiation Units & Measurement (ICRU) [ICRU85 2011] and definitions of terms as defined by the International Commission on Radiological Protection (ICRP) [ICRP103 2007].

*2.3.1 Fluence and Flux*

Particle fluence, $\Phi$, is derived from SI units. Fluence has the units of $m^{-2}$ and is defined as:

$$\Phi = \frac{dN}{da}, \tag{2.2}$$

where *dN* is the number of particles incident on a cross-sectional area, *da.*

Particle flux has the traditional definition of particles per unit area per second ($cm^{-2}s^{-1}$). However, flux can also be defined as the time derivative of fluence:

$$\dot{\Phi} = \frac{d\Phi}{dt}, \tag{2.3}$$

where *dt* is a change in time. The units normally associated with flux are $cm^{-2}sr^{-1}s^{-1}$.

*2.3.2 Mass Stopping Power*

Mass stopping power, $S/\rho$, of a material of density, $\rho$, is the measure of mean energy, *dE*, lost by charged particles as they pass through a material some distance, *dl*, hence:

$$\frac{S}{\rho} = \frac{1}{\rho}\frac{dE}{dl}. \tag{2.4}$$

Expressing *E* in more convenient units of MeV allows for $\frac{S}{\rho}$ to be in units of $MeVm^2\ kg^{-1}$.

Mass stopping power can be broken down further as a function of its constituent parts:

$$\frac{S}{\rho} = \frac{1}{\rho}\left(\frac{dE}{dl}\right)_{el} + \frac{1}{\rho}\left(\frac{dE}{dl}\right)_{rad} + \frac{1}{\rho}\left(\frac{dE}{dl}\right)_{nuc} \tag{2.5}$$

where $\frac{1}{\rho}S_{el} = \frac{1}{\rho}\left(\frac{dE}{dl}\right)_{el}$ is the component of mass stopping power due to electronic interactions, $\frac{1}{\rho}S_{rad} = \frac{1}{\rho}\left(\frac{dE}{dl}\right)_{rad}$ is the component of mass stopping power due to Bremsstrahlung x-ray emission near the nuclei of the traversed medium, and $\frac{1}{\rho}S_{nuc} = \frac{1}{\rho}\left(\frac{dE}{dl}\right)_{nuc}$ is the component of mass stopping power due to coulomb interactions with the nuclei of the medium.

*2.3.3 Linear Energy Transfer*

Linear energy transfer (LET), $L_{\Delta}$, is the average energy lost by a particle due to interactions with electrons as it traverses some distance in a medium:

$$L_{\Delta} = \frac{dE_{\Delta}}{dl} \tag{2.6}$$

Where *dl* is the distance through the medium, the energy cutoff is denoted by the subscript $\Delta$, and this energy is typically in units of eV. Thus, a linear energy transfer of $L_{1000}$would have a cutoff or restriction of 1000 eV. For obvious reasons, this is also known as restricted linear electronic stopping power.

The unrestricted LET, $L_{\infty}$, is identical to $S_{el}$ and denoted as $L$:

$$L_{\infty} = S_{el} = L \tag{2.7}$$

All instances of $L$ shall be assumed to be in units of $keV/\mu m$ for the remainder of this document unless otherwise noted.

*2.3.4 Lineal Energy Transfer*

The lineal energy, $y$, is a stochastic quantity. It is a measurement of energy, $\varepsilon_s$, deposited in matter divided by the mean distance traveled through the matter, $\bar{l}$:

$$y = \frac{\varepsilon_s}{\bar{l}} \tag{2.8}$$

The units are the same as LET: $keV/\mu m$. In the case of a TEPC with a spherical active volume of measurement, the mean distance traveled through the active volume is equal to 2/3 the diameter of the volume:

$$\bar{l} = \frac{2}{3}d \tag{2.9}$$

*2.3.5 Absorbed Dose and Dose Rate*

Absorbed dose, $D$, is the mean energy deposited by ionizing radiation divided by the mass into which the ionizing radiation is imparting its energy:

$$D = \frac{dE}{dm}. \tag{2.10}$$

Absorbed dose is measured in units of joules/kg. The ICRU defines a special case of this unit for absorbed dose: Gray (Gy). 1 Gy = 1 J/kg. Absorbed dose measured in a detector in a beam of mono-energetic particles is proportional to the fluence, $\Phi$, of the particles traversing the active volume of the detector. The fluence is multiplied by the average energy, $\varepsilon_{ave}$, deposited into the active volume of the detector divided by the mass of the detector's active volume:

$$D = \frac{\Phi \varepsilon_{ave}}{m}. \tag{2.11}$$

The average energy deposited into the active volume of the detector for a mono-energetic beam is the lineal energy, *y*, of the particles in the beam multiplied by the mean chord length, $\bar{l}$:

$$\varepsilon_{ave} = y\bar{l} = \frac{2}{3}yd, \tag{2.12}$$

where *d* is the diameter of the active volume. This yields a dose of the following form:

$$D = 1.602 * 10^{-16}\frac{2\Phi yd}{3m}, \tag{2.13}$$

where $1.602*10^{-16}$ converts keV to Joules. Absorbed dose in a mixed radiation field requires summing over the different particle energies and the associated fluxes:

$$D = 1.602 * 10^{-16}\frac{2d}{3m}\sum_i \Phi_i y_i \ . \tag{2.14}$$

The particles with energy, $y_i$, have fluence, $\Phi_i$. Absorbed-dose rate, $\dot{D}$, is the time derivative of the dose:

$$\dot{D} = \frac{dD}{dt}. \tag{2.15}$$

The units of dose rate are J $kg^{-1}$ $s^{-1}$ or Gy $s^{-1}$.

*2.3.6 Dose Equivalent*

Dose Equivalent, *H,* is the product of absorbed dose, *D*, and the quality factor *Q*:

$$H = QD, \tag{2.16}$$

where the quality factor, $Q$, as a function of LET, *L,* is:

$$Q(L)\begin{cases} 1 & L < 10\frac{keV}{\mu m} \\ .32\,L - 2.2 & 10 \le L \le 100\frac{keV}{\mu m} \\ \frac{300}{\sqrt{L}} & L > 100\frac{keV}{\mu m} \end{cases} \tag{2.17}$$

Since *y = 3/2 L*, *Q* can be defined as a function of lineal energy:

$$Q(y)\begin{cases} 1 & y < 15\frac{keV}{\mu m} \\ .32\ \frac{2*y}{3} - 2.2 & 15 \le y \le 150\frac{keV}{\mu m} \\ \frac{300}{\sqrt{\frac{2*y}{3}}} & y > 150\frac{keV}{\mu m} \end{cases} . \quad (2.18)$$

The units of dose equivalent are Joules $kg^{-1}$. Dose equivalent has the special unit name of Sievert (Sv) for Joules $kg^{-1}$. Dose equivalent is used because extensive studies have shown that cell death rates for a given absorbed dose have a dependence on the LET (or lineal energy) of the incident ionizing radiation.

# CHAPTER III

## TISSUE EQUIVALENT PROPORTIONAL COUNTERS

### *3.1 Gas Filled Detectors*

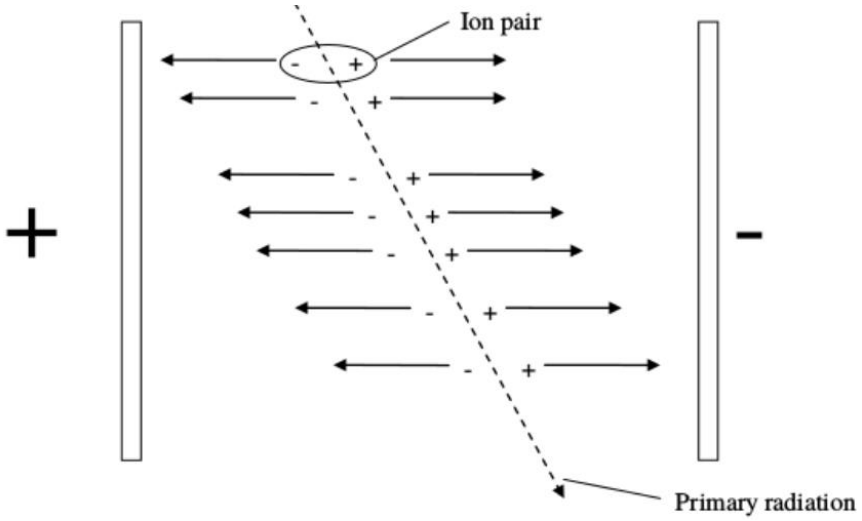


Figure 3.1: Ion pairs created in a gas filled detectors [Collums 2012].

Gas filled detectors consist of two electrodes separated by some distance that is filled with gas [Boag 1966]. As ionizing radiation traverses the active volume of a detector, it collides with molecules in the gas. As illustrated in Figure 3.1, the ionization process creates ion pairs by removing electrons from their respective molecules. Each ion pair consists of a large positive ion with charge, $q = e$, and a relatively light electron with charge, $q = -e$. The electric force accelerates the ion pairs in the electric field of the detector:

$$\vec{F} = q\vec{E}, \tag{3.1}$$

where $\vec{F}$ is the force on the ion with charge, $q$, in an electric field, $\vec{E}$. Force on a particle is also equal to its mass, $m$, times its acceleration, $\vec{a}$:

$$\vec{F} = m\vec{a}. \tag{3.2}$$

Equating the right-hand side of Equations 3.2 and 3.1 and solving for acceleration:

$$\vec{a} = \frac{q}{m}\vec{E}. \tag{3.3}$$

The ion pairs are in the same electric field and have the same magnitude of charge; the magnitude of the acceleration is a function of *1/m*. The masses of the positive ions are on the order of $10^3$ electron masses. The electrons are highly mobile an electric field due to their low mass. The acceleration of the positive ions is approximately $10^{-3}$ times the acceleration of the electrons in the gas. The mobile electrons are accelerated to the anode by the electric field in the detector. A circuit that is connected to the anode then measures the electrons. The electrons are usually measured by total charged collected or some voltage drop across the circuit [Boag 1966].

Gas filled detectors fall into one of three categories: ionization chambers, proportional counters, and Geiger-Muller counters. The category is dictated by the operating voltage of the gas filled detector. Figure 3.2 shows five regions for three types of ionizing radiation: alpha particles, beta particles, and gamma rays. The actual voltage ranges associated with each region are dependent on both the geometry and constituent materials of a detector's active volume.

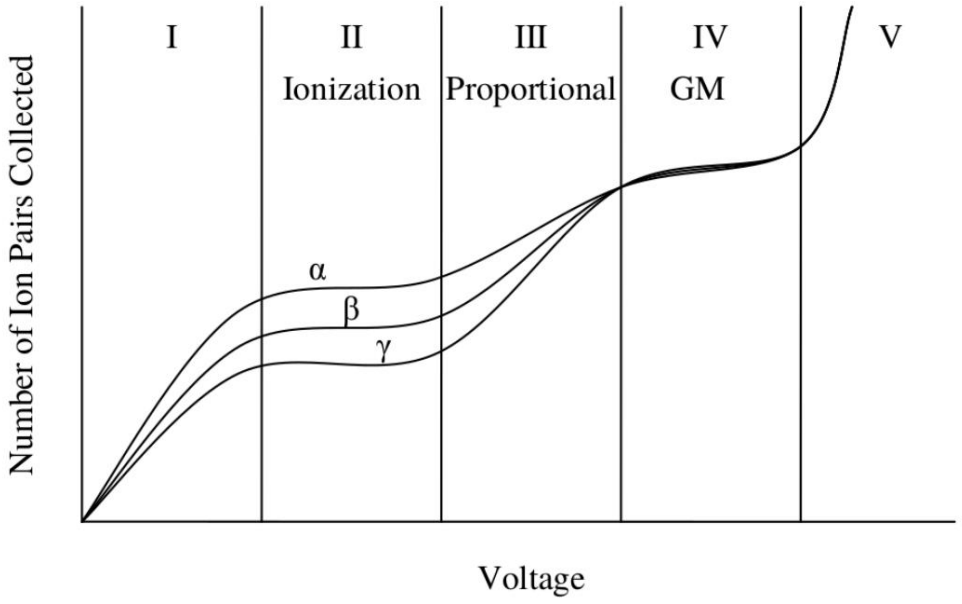


Figure 3.2: Gas filled detector voltage regions [Collums 2012].

The number of collected electrons for devices with operating voltages in region I is not proportional to the amount of energy deposited into the active volume of those instruments because of recombination. Recombination of the ions is the result of the electrical force not being sufficiently high to accelerate the electrons to the anode.

The electrical force on electrons in instruments operating at voltages in region II is high enough to eliminate recombination. The output signal is proportional to the energy deposited in the active volume of the detectors for instruments operating at voltages in region II.

The electrical force is high enough in the active volume of instruments operating at voltages in region III to accelerate electrons enough to create secondary ionization avalanches and cause gas multiplication of the signal.

The output signal is not proportional to the energy deposited into the active volumes of instruments that operate at voltages in region IV. Single ionization events lead to large output signals in region IV.

The electrical force is so high that a single ion pair creation leads to perpetual ionization avalanches in instruments that operate at voltages in region V. ATED is operated in the proportional region at 900 VDC.

### *3.2 Proportional Counters*

A proportional counter is a gas-filled detector that produces an analog output signal that is proportional to the energy deposited by ionizing radiation in the active volume of the detector [Benjamin 1968]. Figure 3.3 illustrates incident ionizing radiation traversing the active volume of a proportional counter with a spherical active volume. The potential difference between the grounded spherical shell and the anode in a spherical proportional counter accelerates these electrons. The electrons collide with other molecules in the gas, creating further ionization [Rossi 1996, Benjamin 1968, Boag 1966]. These electrons create a voltage drop in the circuit which is amplified by a preamplifier and then by a shaping amplifier. The amplified signal will be stored on a computer.

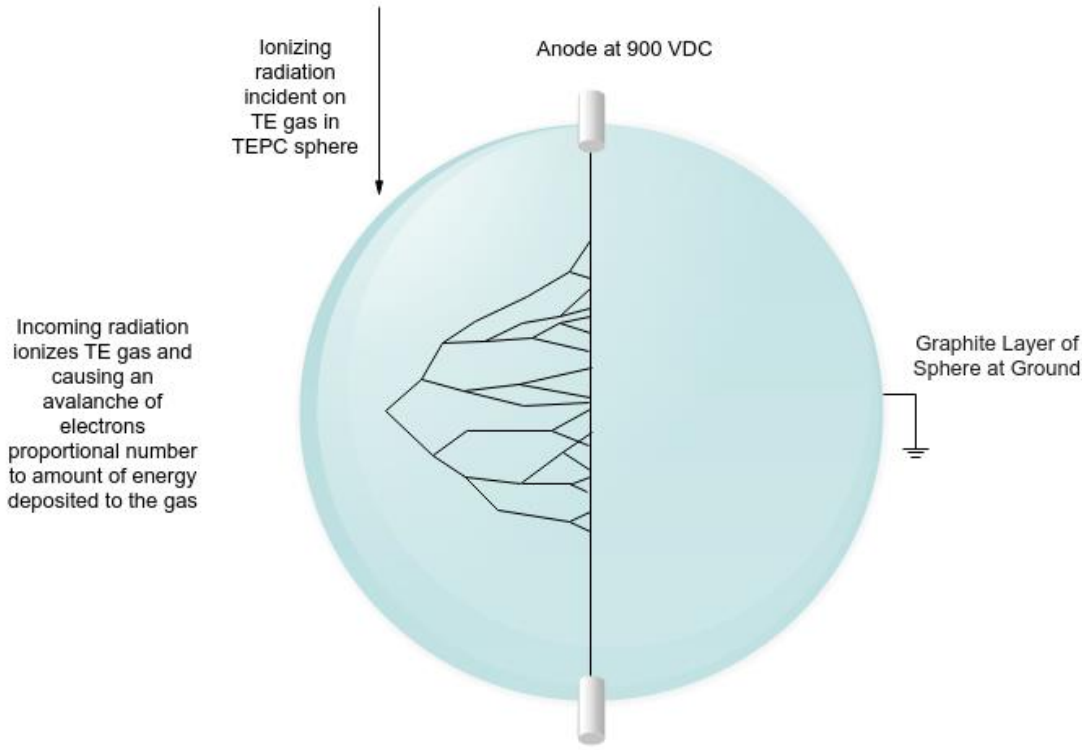


Figure 3.3: Spherical proportional active volume during an ionization process: electron cascades are accelerated towards the positively charged anode. 900 VDC was found to be in the proportional region for ATED.

### *3.3 Tissue Equivalent Proportional Counters (TEPC)*

Tissue Equivalent Proportional Counters (TEPC) are proportional counters that respond to ionizing radiation similar to how tissue responds to ionizing radiation. Energy deposited in the active volume of the detector by ionization and nuclear interactions usually mimics a one or two-micron diameter cell of tissue. The active volume of the detector contains a tissue equivalent gas that is ionized by ionizing radiation similar to tissue. The tissue equivalent gas is at a pressure that, by use of site equivalence, receives the same energy deposition by ionizing radiation as does a one-micron cell of tissue. The relatively high-density tissue equivalent plastic surrounding the tissue equivalent gas allows the detector to respond to interactions with neutrons

similar to how tissue responds to interactions with neutrons [Rossi 1996, Benjamin 1968, Boag 1966].

### *3.3.1 TEPC Active Volumes and Microdosimetry*

To understand the lineal energy measurements of a TEPC, we must first derive and understand some basic principles of microdosimetry. We discuss the simulated active volume and the average chord length of a TEPC so that we can further understand the energy deposition process. Understanding the energy deposition process will allow us to understand the measurement process and better analyze the spectra measured by a TEPC.

#### *3.3.1.1 Simulated Active Volume Diameter: Microdosimetric Principles*

A spherical TEPC active volume simulates a spherical volume of tissue with a much smaller diameter; any ionizing radiation field will deposit the same amount of energy into the active volume of the detector per unit mass as it would deposit into the simulated volume of tissue. This is referred to as site equivalence. Site equivalence is described by the following equation [ICRU36 1985, Brackenbush 1990, Rossi 1996]:

$$\bar{\varepsilon_g} = \overline{\varepsilon_w}\,, \tag{3.4}$$

where $\bar{\varepsilon_g}$ is the average energy deposited into the tissue equivalent gas of the TEPC, and $\overline{\varepsilon_w}$ is the average energy deposited into an as yet undefined volume of water. Note, water is assumed to be equivalent to tissue in terms of energy absorption from ionizing radiation. The energy deposited in the gas can be defined as follows [ICRU85 2011, ICRU36 1985, Rossi 1996]:

$$\bar{\varepsilon_g} = \left(\frac{S_g}{\rho_g}\right)_{el} * \rho_g \, \bar{l}_g, \tag{3.5}$$

where $(\frac{S_g}{\rho_g})_{el}$ is the electronic mass stopping power, of a material of density, $\rho_g$ , and $\bar{l}_g$is the average chord length traversed by incident ionizing radiation through the TE gas. The mass stopping power of tissue equivalent materials are equal to the mass stopping power of water [ICRU36 1985, Rossi 1996]:

$$(\frac{S_w}{\rho_w})_{el} = (\frac{S_g}{\rho_g})_{el}, \tag{3.6}$$

where the *w* subscripts indicate the simulated tissue site and the *g* subscripts indicate the active volume site. Substituting equation 3.6 into equation 3.5, substituting the given results into equation 3.4, and canceling the equivalent terms yields [ICRU36 1985, Rossi 1996]:

$$\rho_w \bar{l}_w = \rho_g \bar{l}_g . \tag{3.7}$$

The density of water is 1 g/cm$^3$. Equation 3.7 becomes:

$$\bar{l}_w = \rho_g \bar{l}_g . \tag{3.8}$$

Equation 3.8 gives the average chord length of the simulated spherical volume as a function of the density and average chord length of the active spherical volume of the detector. We now derive the average chord length for an isotropic field of particles traversing a spherical volume. This result is substituted in Equation 3.8 to yield the result for the diameter of the simulated spherical volume as a function of density and diameter of the active spherical volume.

*3.3.1.2 Average Chord Length*

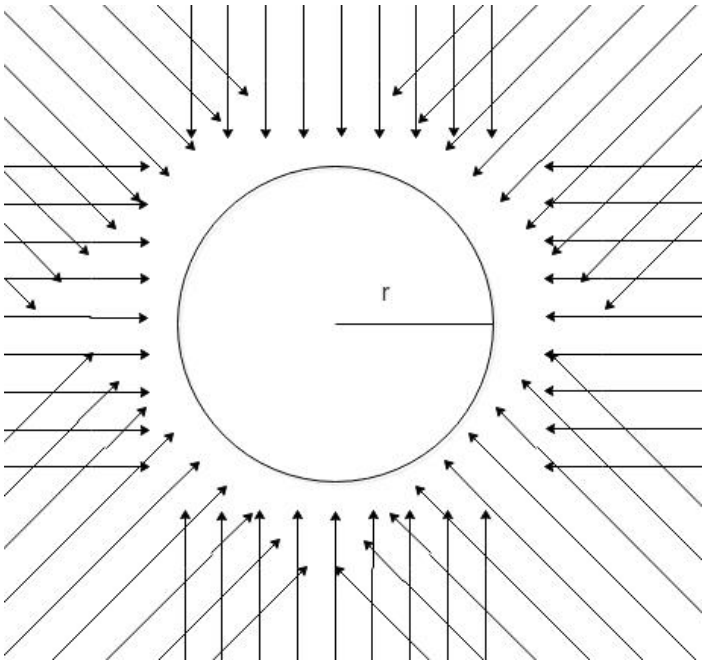


Figure 3.4: Cross-section of a sphere in an approximated isotropic radiation field. Adapted from: [Collums 2012]

Consider an isotropic radiation field incident on a sphere of radius r. Figure 3.4 approximates such a field. For an isotropic radiation field, symmetry allows removing all but one direction of the field to yield the same result for the chord length distribution of a sphere as shown in Figure 3.5.

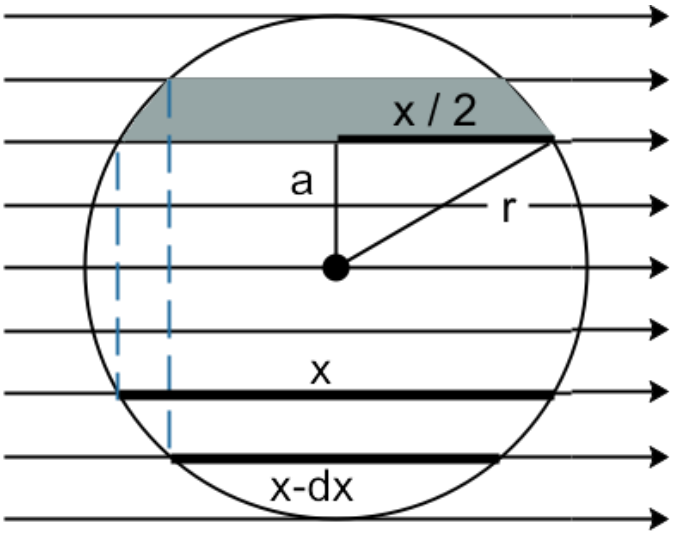


Figure 3.5: Unidirectional uniform radiation field incident on a sphere of radius r. Adapted from: [Collums 2012]

The probability that incident radiation has an impact parameter between lengths *a* and $a + da$ is the same probability that the radiation will traverse the spherical segment in gray in Figure 3.5. This probability as a function of impact parameter, *a*, is [Rossi 1996]:

$$P(a)da = \frac{2\pi a da}{\pi r^2}. \tag{3.9}$$

From the right triangle in Figure 3.5, the impact parameter, *a*, as a function of the chord length, *x*, as:

$$a(x) = \sqrt{r^2 - \left(\frac{x}{2}\right)^2}. \tag{3.10}$$

Differentiating to find da:

$$da = \frac{-x dx}{4\sqrt{r^2 - \left(\frac{x}{2}\right)^2}}. \tag{3.11}$$

Substituting equations 3.11, and 3.10 into equation 3.9:

$$P(a)da = \frac{-xdx}{2r^2}. \tag{3.12}$$

The probability for the radiation to pass through the sphere with impact parameter between some lengths *a* and *a + da* is equal to the probability that the particle will have chord length between some lengths *x* and *x - dx*. This implies:

$$P(a)da = -P(x)dx. \tag{3.13}$$

Giving the chord length probability distribution:

$$P(x) = \frac{x}{2r^2}. \tag{3.14}$$

The distribution is given in terms of diameter, *d*, of the sphere to simplify calculations,

$$P(x) = \frac{2x}{d^2}. \tag{3.15}$$

The average chord length, $\bar{l}$, is given by the integral:

$$\bar{l} = \int_0^d P\,(x)xdx. \tag{3.16}$$

Integrating gives the average chord length for incident radiation in an isotropic radiation field. The average chord length of a sphere is two-thirds its diameter:

$$\bar{l} = \frac{2d}{3}. \tag{3.17}$$

Replacing the $\bar{l}_i$ terms in Equation 3.8 with 2/3 $d_i$ and cancelling like terms:

$$d_w = \rho_g \, d_g. \tag{3.18}$$

Equation 3.18 is the relationship between an active volume of a TEPC and the volume it simulates; the diameter of the volume simulated by a TEPC is equal to the density in the active volume of the TEPC multiplied by the diameter of the TEPC active volume.

### 3.3.2 Lineal Energy Spectra

Substituting equation 3.18 and equation 3.17 into equation 2.8 and canceling like terms yields lineal energy as a function of chord length traversed in a TEPC active volume (Rossi 1996):

$$y = \frac{L \, \rho_g \, x}{\frac{2}{3}d}. \tag{3.19}$$

where $L$ is the LET of a particle, $\rho_g$ is the density of the gas in the active volume of the detector, $d$ is the simulated diameter, and $x$ is the simulated chord length traversed by the particle. This function is plotted in Figure 3.6 with the LET spectrum associated with the ideal lineal energy spectrum.

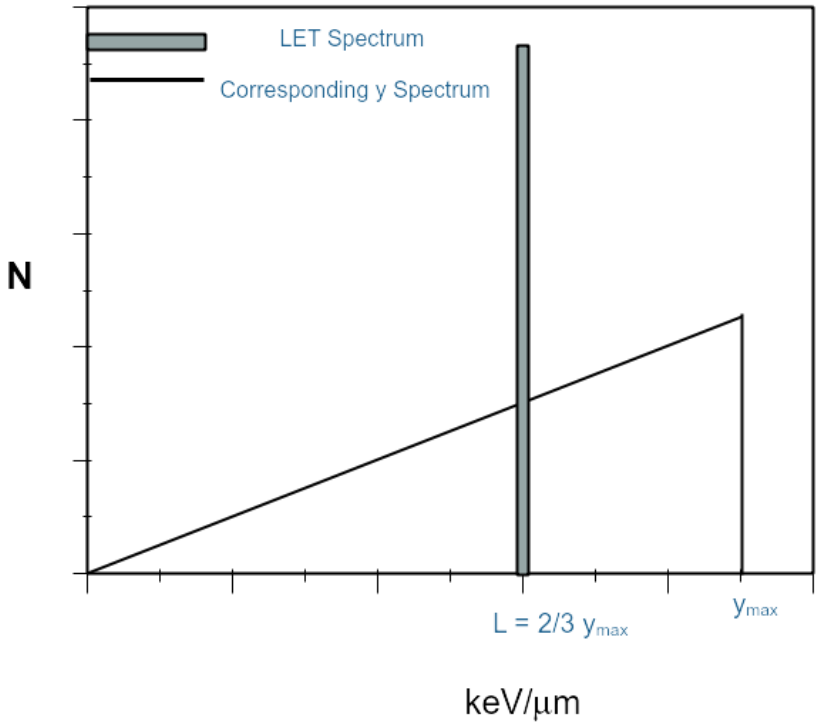


Figure 3.6: Ideal lineal energy spectrum and associated LET spectrum for the proportional counter. Adapted from [Rossi 1996]

The ideal maximum lineal energy value in a lineal energy spectrum is 3/2 of the LET of the traversing particles in an isotropic radiation field [Rossi 1996].

*3.3.2.1 Representing Microdosimetric Distributions*

Plotting representations of spectra from measurements made with a TEPC must be chosen for the specific applications of the plot [Rossi 1996]. We will consider measurements of neutrons from a Plutonium Beryllium neutron source made with ATED.

Let us first consider plotting the raw spectrum of counts, *f(y)*, versus lineal energy, *y*, as shown in Figure 3.7. One issue inherent to this representation is that *f(y)* spans five orders of magnitude [Rossi 1996]. *f(y)* appears to have substantial counts only in the range of *y* up to approximately 15 keV/µm.

As shown in Figure 3.8, representing the measurement as a log(f(y)) vs. log(y) shows characteristics that were unnoticeable in the linear-linear plot [Rossi 1996].

Namely, the proton edge (~147 keV/µm) and the electron edge (~12 keV/ µm) become apparent in this representation [Rossi 1996, Moro 2015]. These are two calibration points on the spectrum that are discussed in detail in Chapter 5.

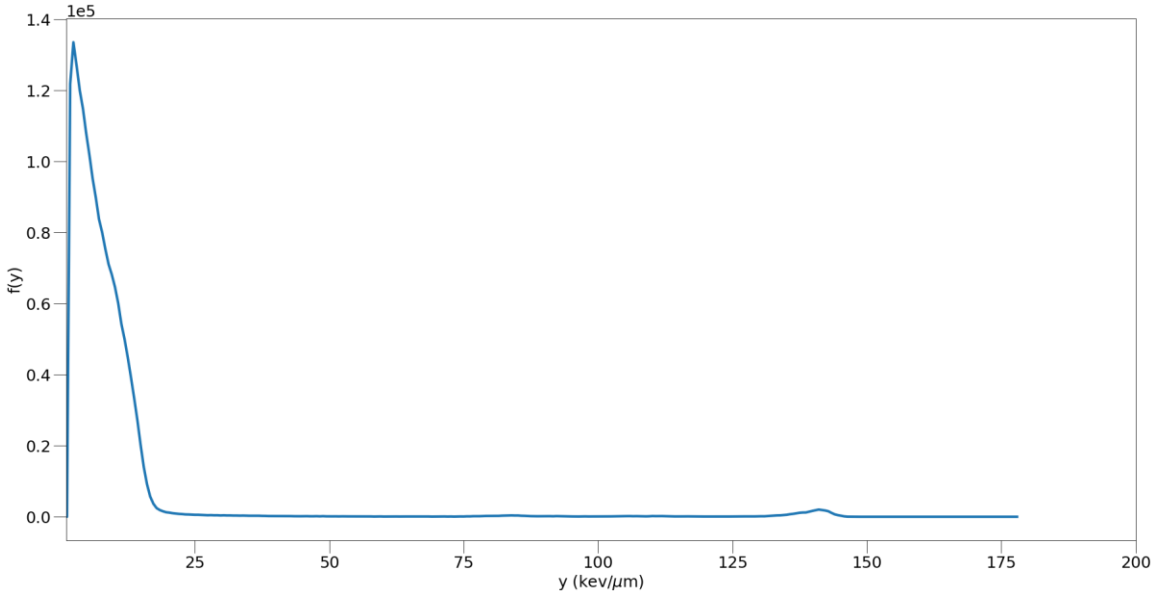


Figure 3.7: f(y) vs. y for a PuBe neutron source.

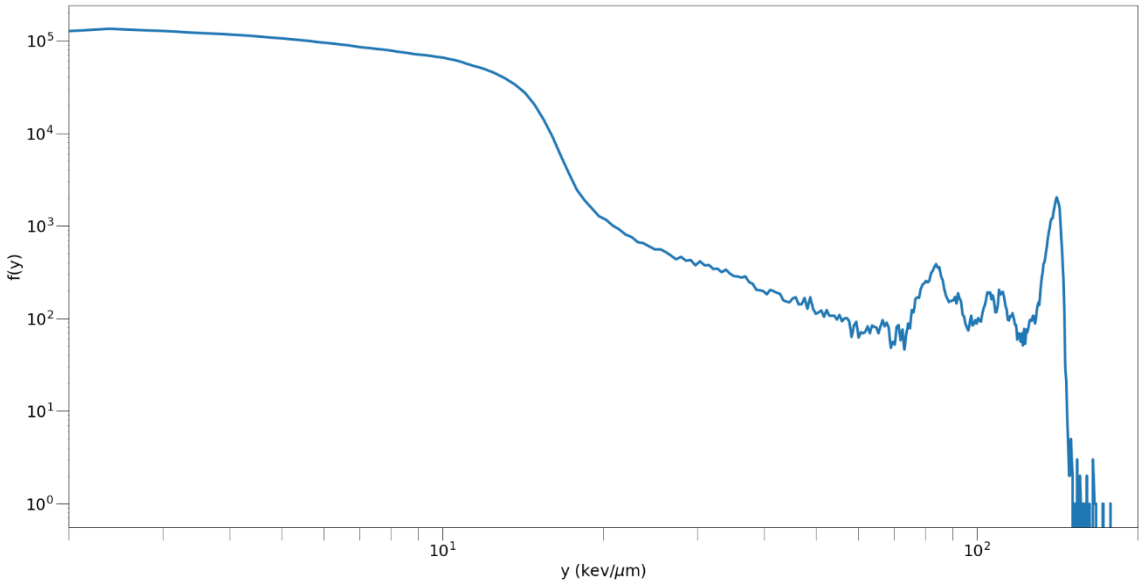


Figure 3.8: log(f(y)) vs log(y) for PuBe neutron source.

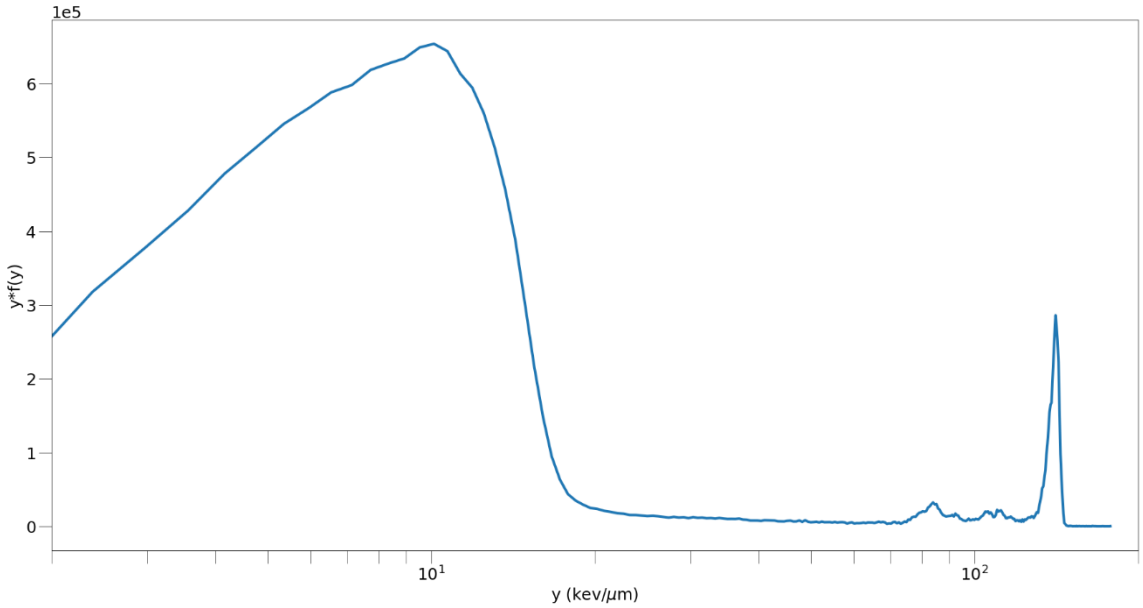


Figure 3.9: y*f(y) vs log(y) for PuBe neutron source.

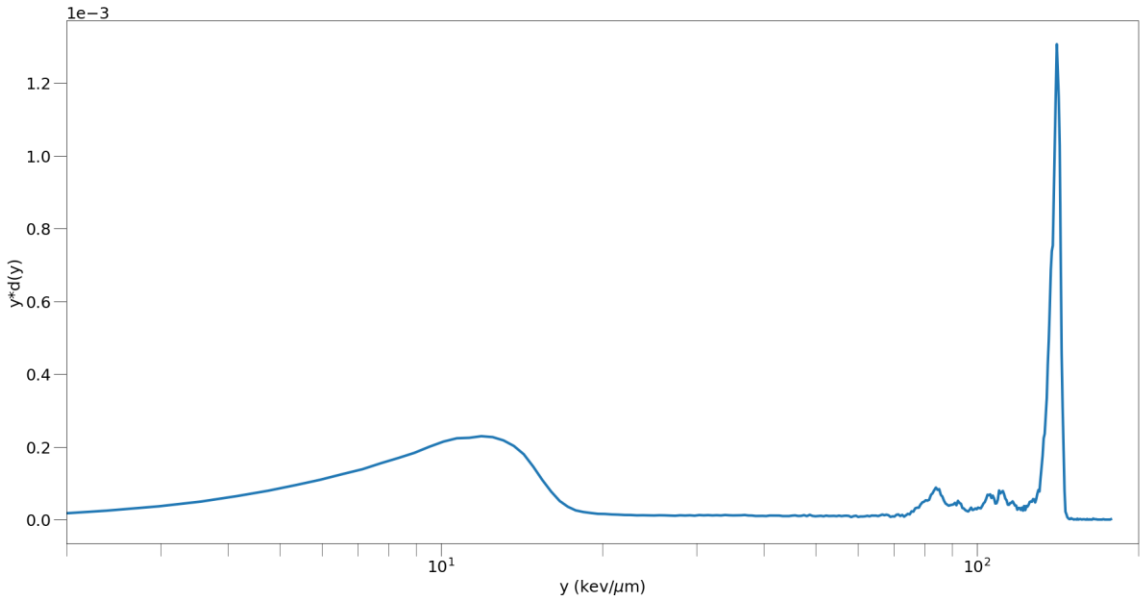


Figure 3.10: y*d(y) vs log(y) for PuBe neutron source.

The primary use of our TEPC is taking measurements for dosimetry. So let us define a distribution, *d(y)*, that is proportional to absorbed dose [Rossi 1996].

$$d(y) = y * f(y) \tag{3.20}$$

Figure 3.9 shows *d(y)* vs *log(y).* However, the spectrum is distorted in such a way that the visual representation of the area under the curve is not proportional to absorbed dose because of the log representation of the abscissa. By multiplying *d(y)* by *y,* the area under the curve becomes proportional to absorbed dose. Figure 3.10 is a plot of *y*d(y)* vs. *log(y).* This representation shows all desired characterizations of the dose while keeping the spectral characterizations for the calibration points [Rossi 1996].

A comparison of Figure 3.7 and 3.10 may be surprising. Figure 3.10 shows that a large contribution of the absorbed dose is from particles with lineal energy above 100 keV/µm. The counts above 100 keV/µm in Figure 3.7 appear negligible when compared to the counts from the particles with lineal energies below 15 keV/µm.

### *3.3.3 Dose Calculations*

TEPC absorbed dose measurements simulate living tissue, making their measurements the most dependable among dosimeters. Tissue equivalent active volumes are constructed in such a way that allows them to simulate living tissue on a small scale [Brackenbush 1990]. This is achieved in two ways: using tissue equivalent (TE) plastic for the chamber wall and using a low-pressure TE gas [Rossi 1996]. The energy deposited by radiation is deposited by means of ionization or nuclear interaction. The deposited energy is measured by TEPC to yield measured absorbed dose and dose equivalence [Braby 1985, Boag 1966, Rossi 1996].

#### *3.3.3.1 Absorbed Dose*

Absorbed dose is given in units of energy per mass (Gy = Joules/kg). To calculate absorbed dose from TEPC lineal energy measurements, we must know the mass of the

gas in the active volume of the detector and the total energy deposited into the active volume of the detector. Since TEPC measure deposited lineal energy, all that is required is a relationship between deposited lineal energy and absorbed dose [Rossi 1996, Collums 2012]:

$$D(y) = y * f(y)\frac{\bar{l}}{m} * 1.602 * 10^{-16} J/eV \tag{3.20}$$

where *m* is the mass of the gas in the active volume of the detector, $\bar{l}$ is the mean chord length of the detector active volume, *y* is the lineal energy, $1.602 * 10^{-16}$ converts eV to Joules, and *f(y)* is the counts as a function of lineal energy. This implies that absorbed dose is proportional to the amount of energy deposited per unit length. The absorbed dose, *D*, is calculated by summing over the energies of the spectrum [Rossi 1996, Collums 2012]:

$$D = \sum_{y_i} y_i * f(y_i)\frac{\bar{l}}{m} * 1.602 * 10^{-16} J/eV \tag{3.21}$$

where $y_i$ is the lineal energy for a given channel, and $f(y_i)$ is the counts in the channel associated with lineal energy $y_i$.

*3.3.3.2 Dose Equivalent*

Inserting Equation 3.21 into Equation 2.16 yields dose equivalent as a fully specified function of lineal energy.

$$H = Q(y) * \sum_{y_i} y_i * f(y_i)\frac{\bar{l}}{m} * 1.602 * \frac{10^{-9} J}{eV}, \tag{3.22}$$

where the quality factor, $Q(y)$, is:

$$Q(y)\begin{cases} 1 & y < 15\frac{keV}{\mu m} \\ .32\ \frac{2*y}{3} - 2.2 & 15 \le y \le 150\frac{keV}{\mu m} \\ \frac{300}{\sqrt{\frac{2*y}{3}}} & y > 150\frac{keV}{\mu m} \end{cases} . \quad (3.23)$$

# CHAPTER IV

## ACTIVE TISSUE EQUIVALENT DOSIMETER

Active Tissue Equivalent Dosimeter (ATED) is the current model of a device that has been in development for several years. Prototyping of the subsystems of the unit began with NIM-bin devices. After proof-of-concept was shown using NIM-bin devices, in-house prototypes started as passive components on breadboards. This would lead to either fabricating printed circuit boards, buying commercial-off-the-shelf (COTS) parts, or some combination of these.

Many COTS parts were chosen to optimize reproducibility of measurements. Another benefit of using COTS parts is that they typically have signal input and output impedances of 50 Ω. Having components with matching impedance maximizes the signal to noise ratio (SNR). Maximizing SNR allows particles with low lineal energy to be detected. Particles with low lineal energy also have low absorbed dose per particle. But the majority of measured data is in the region associated with low lineal energy particles in low-Earth orbit. Over time this region accumulates approximately 50% of the absorbed dose on ISS [Badhwar 2002].

*4.1 The Detector*

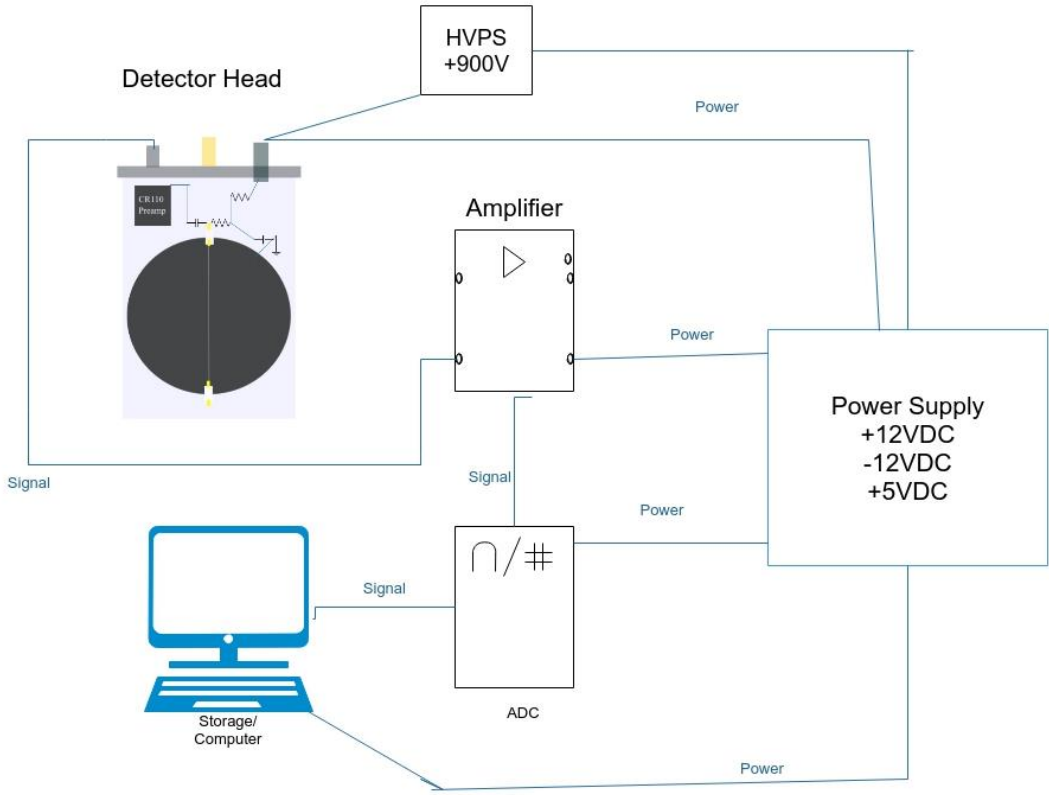


Figure 4.1: The TEPC setup for these experiments includes a detector head, Gaussian shaping amplifier, power supply, high voltage power supply, spectrometer and a computer.

ATED is a tissue equivalent proportional counter (TEPC) designed to determine the absorbed dose and dose equivalence from the measured energy deposited in the detector by ionizing radiation passing through the active volume of the detector. Ionizing radiation ionizes the molecules in the tissue equivalent gas as it traverses ATED's active volume. This creates ion pairs that consist of highly mobile negatively charged electrons and positively charged nuclei in the gas. The electrons in ATED are accelerated during ionization by the 900 VDC potential difference between the grounded spherical shell and the anode causing the electrons to interact with other molecules in the gas. These

interactions create an avalanche effect that deposits electrons onto the anode and causes a capacitor to discharge. This creates a voltage drop in the circuit. This voltage drop is proportional to the absorbed dose deposited in the gas [Boag 1966, Rossi 1996].

A Cremat CR-100 rev. 2 preamplifier inverts the signal and amplifies the magnitude of the voltage drop, and the signal is transmitted to a Cremat CR-200-1μs pulse shaping amplifier external to the detector head. Unlike previous TEPC models, the preamp is in the pressurized detector head to minimize noise. The pulse-shaping amplifier again amplifies the signal and reshapes it into a Gaussian shape. The Gaussian signal is then transmitted to the spectrometer. The spectrometer converts the signal's pulse height into a channel number using an analog to digital converter. Counts build up in channels over time to yield a spectrum associated with the incident radiation, as shown in Figure 4.2. The spectrometer sends this spectrum to the computer for storage.

*4.2 The Spectrum*

ATED uses an Amptek MCA-8000D spectrometer. The electronics' capabilities allow for measurements only between channels 3 and 6300. The channel number is proportional to lineal energy; a count in a higher channel number indicates that the corresponding incident ionizing particle deposited more energy into the active volume of the detector.

*4.2.1 Example Spectrum: 422 MeV Fe*

Figure 4.2 is the spectrum of a mono-energetic beam of 422 MeV iron ions, as measured by ATED at the HIMAC heavy ion accelerator in Chiba, Japan. The characteristic peak of high LET measurements is at channel number 2340. The region marked noise contains some noise counts. The majority of counts in the noise region are due to secondaries created from the iron ions interacting with the acrylic wall in the detector head. The pileup/clipping region is apparent at channel 6350.

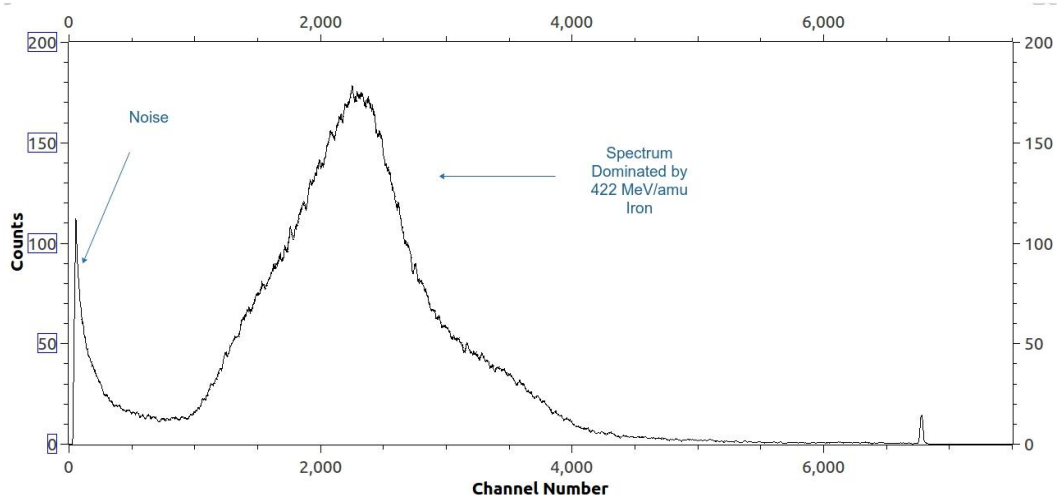


Figure 4.2: Spectrum from a mono energetic beam of 422 MeV iron ions

Figure 4.3 shows ATED's measurement of a mono-energetic beam of 422 MeV iron ions after traversing an absorber equivalent to 40 mm of water. Traveling through the absorber has two effects that make the beam no longer mono-energetic: the absorber reduces the energy (slows down) the iron beam, and some of the absorber and iron particles undergo nuclear fragmentation reactions during interactions that occur as the iron traverses the absorber [ICRU28 1978]. Slowing down the beam increases the lineal energy of the beam and shifts the peak of the spectrum to the right [Rossi 1996].

Fragmentation of the projectile (beam) and target (absorber) yields particles of lineal energy that are noticeable in the noise portion (lowest channel numbers) of the spectrum and in the higher channel numbers of the spectrum [Rossi 1996].

The difference between these two experiments is shown in Figure 4.4. Figure 4.3 is a representative spectrum of the bottom experiment in Figure 4.4. Figure 4.2 is a representative spectrum of the top experiment in Figure 4.4.

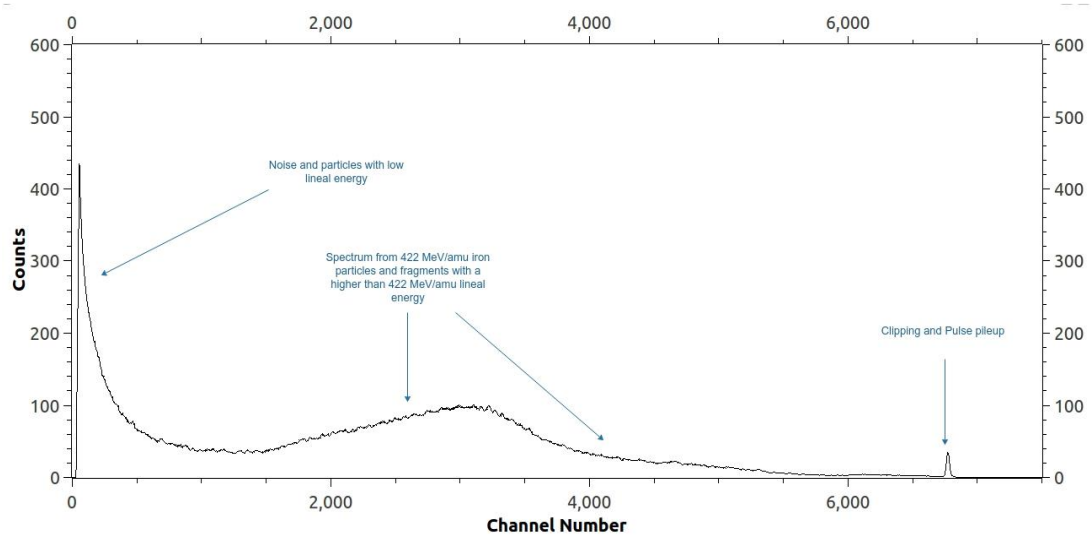


Figure 4.3: 422 MeV/amu iron ions measured with ATED after traveling through plastic equivalent to 40.03 mm of water.

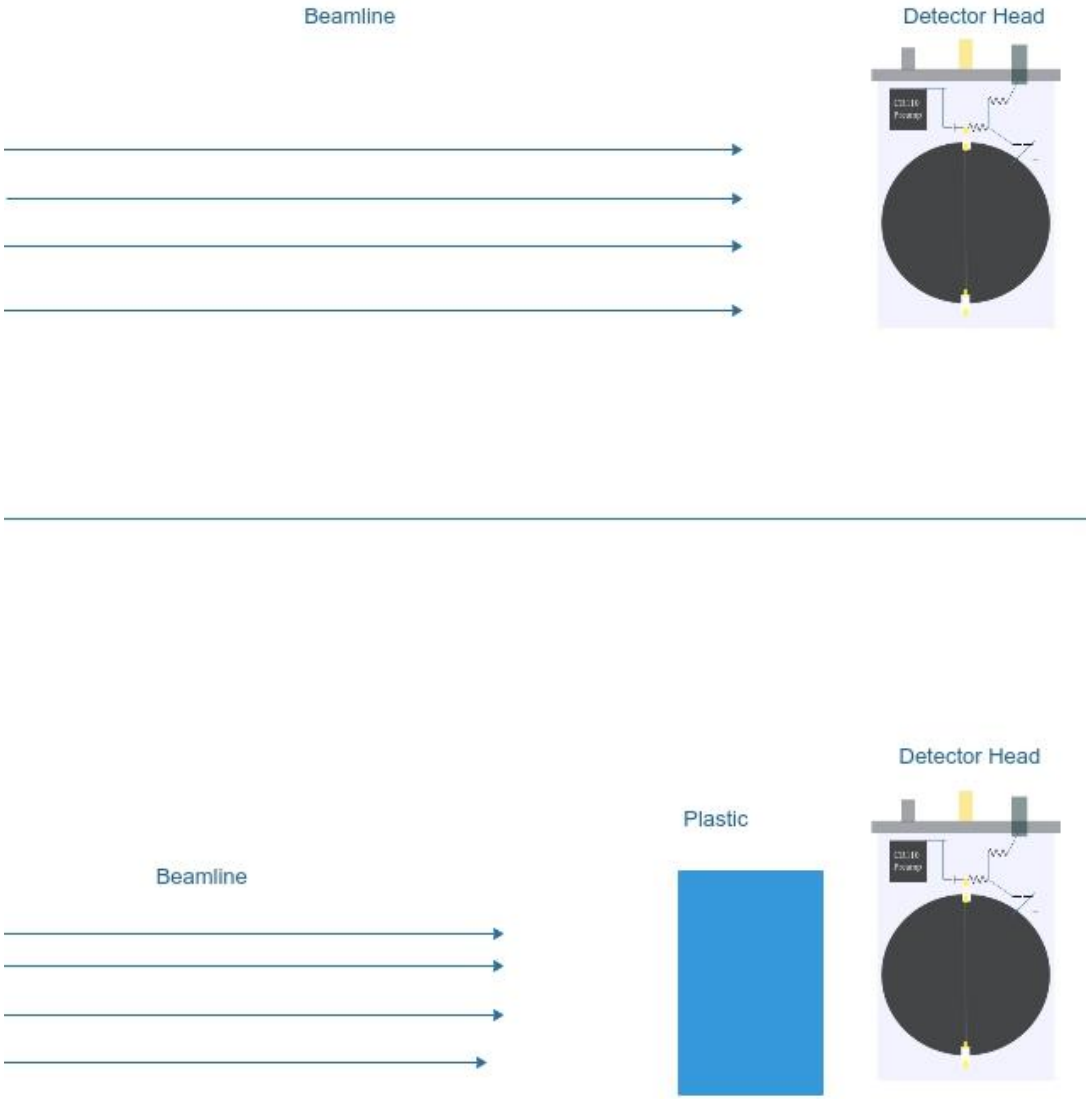


Figure 4.4: Top: Measurement made with bare beam incident on detector. Bottom: Measurement of bare beam incident on plastic.

*4.2.2 Electronic Noise and Low Lineal Energy Particle Detection*

The measurements in Figure 4.2 and Figure 4.3 contain less than 100 counts of noise while the rest of the counts are measurements of energy deposited in the detector by radiation. Reducing the noise to this level was the most time consuming portion of detector design. The three main methods used for noise reduction were choosing components that generate minimal noise, impedance matching at signal connections, and implementing a star ground in the system. These methods together reduced the noise in ATED to less than 0.01% of the noise in the original prototype.

The final choice of ATED components and grounding scheme were made by testing various models of each component and testing many different grounding schemes. The main selection requirement was the minimization of noise to allow for measurements of particles with low lineal energy. The noise was tested in-house using three methods: testing noise levels with no signal source, testing noise levels with a pulse generator, and testing noise levels using active sources.

Connecting a signal generator to the shaping amplifier eliminates the detector head from the circuit. This allows for easier localization of noise sources. With a signal generator connected, the various subcomponents were methodically changed during testing. The final choices minimized the signal from noise. Various grounding schemes were tested with each set of components used.

The detector head was connected to the circuit for testing after optimizing the noise levels of the rest of the instrument. Systematic testing of the noise with and without signal sources was conducted with the detector head connected. Testing included

changing the orientation of components within the detector head, a complete redesign of the detector head, and an overhaul of the method for grounding the detector head.

Impedance matching was necessary between each component of the detector system. Impedance matching required matching the impedance between the following interfaces: the detector head and the Gaussian shaping amplifier, the Gaussian shaping amplifier and the spectrometer, and the spectrometer and the computer. The amount of reflected signal was minimized by matching the input/output impedances of adjacent components in the signal path of ATED. Minimizing the reflection of the analog signals in the connections reduces SNR. It is not possible to match impedances for a wide range of signal frequencies. This required optimizing the matching of impedance for frequencies and amplitudes expected for measurements of ionizing radiation in space and the atmosphere.

A star ground was obtained by connecting all of the grounds from each component of a system to one location on the system. The star ground was obtained in ATED by connecting all of the grounds from each component to the chassis of the ATED unit. Star grounds minimize ground loops in electrical systems. Ground loops create signals in the system that appear identical to measured particles in the spectrum. These signals are still present in the ATED spectra but have been reduced by over 90% by the use of the star ground. The star ground also partially fulfills bonding/grounding requirements for an instrument on ISS. ATED could not have flown on ISS if a star ground was not implemented in the design.

*4.2.3 Pileup and Clipping Region*

Counts from two phenomena are placed in the clipping region of the spectrum by the spectrometer: clipping of high LET signals and clipping of signals from pulse pileup in the amplifier circuit.

Clipping in the amplifier circuit occurs when a particle of high enough lineal energy is incident on the active volume of the detector head. The amplitude of the signal that would be generated by the particle is larger than the amplifier is capable of producing. The top of the signal is "clipped" off, and all counts from particles above a threshold energy deposition are put into the upper most channel by the spectrometer. These counts must be ignored in absorbed dose calculations as they could be measurements of particles with arbitrarily high lineal energy.

Pulse pileup occurs when the detector's electronics add the signals of two or more particles that are incident on the detector's active volume. This happens when two or more particles simultaneously ionize the gas in the active volume of the detector. Pulse pileup can also occur when signals from separate particles come so rapidly that the supporting electronics are unable to distinguish a single peak. This forces the hardware to send one larger amplitude signal to the software. The signal is clipped if the signal amplitude from pulse pileup is large enough. Pulse pileup due to high flux particles is extremely unlikely in LEO and in the atmosphere. Very little or no added absorbed dose rate is expected to occur from pulse pileup during the ISS experiment.

*4.4 ATED Components*

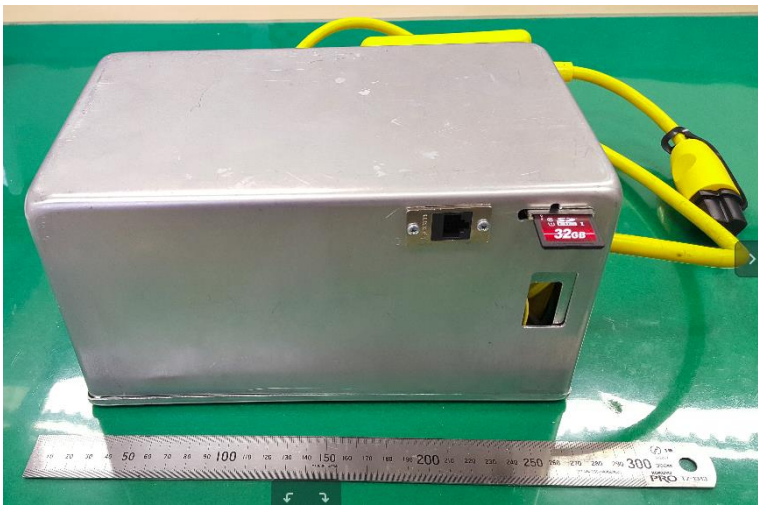

Figure 4.5: ATED.

*4.4.1 Detector Head*

ATED was designed to be used as a long-term TEPC. Long-term use requires design of the detector head that minimizes any leaking of the TE gas. The gas valve in the new design is a copper tube that is pinched-off using a technique called cold welding pinch-off. A 1/4" oxygen-free copper tubing from Vacuum Process Engineering in Sacramento, CA was used as the gas inlet tube. The copper tube underwent chemical treatment and heat treatment at the above company to maximize the effectiveness of the cold weld process. The tool for pinch-off cold-welding is shown in Figure 4.6.

Torr Seal® (vacuum seal epoxy) was used around all electrical feedthroughs and around the detector head lid to achieve minimal TE gas leakage.

The active volume acrylic spherical shells are 3" in diameter. This size was chosen to maximize the cross-section of interaction with rare high-energy particles in

LEO. The acrylic spherical shell is 3 mm thick and tissue equivalent. This detector head simulates a human cell of approximately 2.0 microns in diameter. The detector head lid was designed in-house at the OSU E. V. Benton Radiation Physics Laboratory and machined at the OSU Physics and Chemistry Instrument Shop.

Figure 4.6: Pinch-off tool used to cold-weld the copper gas inlet tube.

Figure 4.8 shows the internal layout of the detector head. The Cremat 110 preamplifier being inside the detector head has two significant benefits: noise reduction and impedance matching. The detector head can is grounded and acts as a Faraday cage; the detector head eliminates any external signals from adding noise to the detector signal before it is amplified. The Faraday cage increases SNR significantly. ATED would not be able to measure low lineal energy particles if the preamplifier was outside of the detector head.

The detector active volume impedance is matched to the shaping amplifier through the use of the Cremat CR-110 preamplifier. The Cremat preamplifier output has an impedance of approximately 50 Ω. This impedance is a close match to the shaping amplifier evaluation board impedance. The nearly matched impedance minimizes reflection of the signal. Impedance matching yields a larger SNR.

The CR-110 rev. 2 preamplifier has a gain of 1.4 V/pC. The rise time is 7 ns. The Decay time constant is 140 µs. The maximum charge detectable per event is 2.1 pC. The preamplifier requires ± 12 V. Power supply current for the preamplifier is 7.5 mA for the positive polarity and 3.5 mA for the negative polarity. The preamplifier dissipates a 70 mW.

Figure 4.7: Detector head.

Figure 4.8: Detector head Active volume and preamplifier with supporting electronics

*4.4.2 Gaussian Pulse Shaping Amplifier*

A Cremat CR-200-1µs non-inverting Gaussian shaping amplifier chip is used. The input noise voltage is 36 µV RMS. The shaping amplifier requires ± 12 V. The quiescent power supply current is 7 mA. The maximum output current is 20 mA. The shaping time is 1 µs.

The commercial-off-the-shelf (COTS) Cremat CR-160-R7 evaluation board was chosen as the supporting electronics for the chip. This COTS circuit allows for the following controls of the signal: gain, DC-offset, and polarity of signals detected. Both the signal input and the signal output of the Cremat CR-160-R7 have impedances of approximately 50 Ω. The input impedance matches the output impedance from the Cremat preamplifier. The output impedance matches the input impedance of the spectrometer.

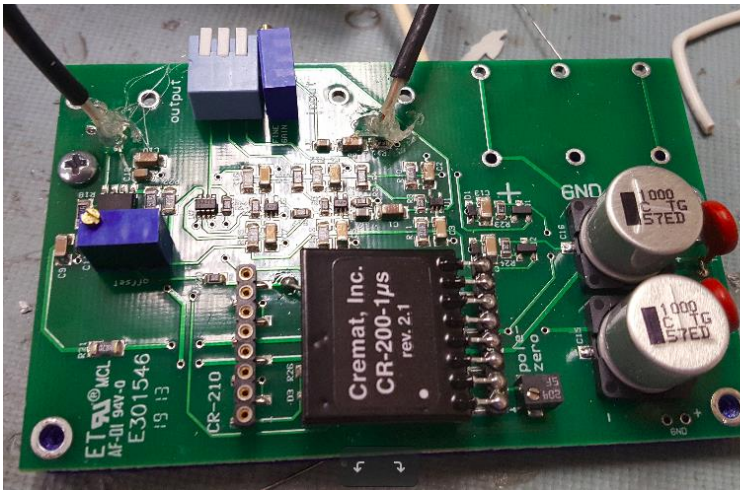


Figure 4.9: Cremat CR-160-R7 board with CR-200 amplifier chip.

*4.4.3 Spectrometer*

Any programmable multichannel analyzer with suitable specifications could be used as ATED's spectrometer. The spectrometer chosen for this experiment is the Amptek model MCA-8000D multichannel analyzer. The unit is capable of analyzing signals up to frequencies of 100MHz at 16 bits for digital pulse height measurements, at a conversion time of 10 ns. The MCA-8000D has a differential nonlinearity $< \pm 0.6\%$ and an integral nonlinearity $< \pm 0.02\%$. There are two TTL compatible gates for coincidence and anticoincidence modes. The unit Supports USB, RS-232, and Ethernet communication interfaces.

The unit is capable of using between 128 and 16384 total channels for measuring spectra. 8192 channels are used for ATED. Channel numbers between 3 and 6300 will contain useful data from the shaping amplifier. The range of channel 3 to 6300 corresponds to lineal energies between 1 and 3000 keV/μm.

The amplifier is connected to the spectrometer via a BNC coaxial cable. The signal input impedance of the spectrometer is approximately 50 Ω; the signal input impedance approximately matches the signal output impedance of the shaping amplifier: the SNR is increased.

The spectrometer is connected to the computer via a USB cable. The spectrometer is powered by +5 VDC.

*4.4.4 Power Supplies*

The ±12 VDC for the amplifier circuits is supplied by an XP Power ECL15UT02-T AC-DC power supply. The +5 VDC for the spectrometer and computer is supplied by an XP Power ECL25US05-S AC-DC power supply. These units can operate with AC input voltages of 85 – 264 VAC or DC input voltages of 120 – 370 VDC. The load input power for each unit is < 0.3 W. Each unit has an efficiency of 72 – 84%. These unit have a 3000 VAC input to output isolation to minimize noise and crosstalk between the power source and the internal components of ATED.

*4.4.5 High Voltage Power Supply*

An EMCO Q12 DC to high voltage DC converter was chosen to supply the high voltage to the detector head. The Q12 unit yields a high voltage (0 - 1200 VDC) proportional to the input voltage (0-8 VDC). The unit can consume a maximum of 0.5 W of power.

Approximately 900 VDC was found to be an acceptable operating voltage for ATED to perform as a proportional counter. Testing determined that the Q12 unit will yield 897 VDC with an input voltage of 6.3 VDC.

A Texas Instruments TPS7A4700 positive adjustable linear voltage regulator evaluation board is used to control the input voltage to the EMCO unit. The voltage regulator was chosen for this experiment after extensive testing showed that this model reduced the amplitude of transient signals. The transient signals propagate over the +12 VDC bus. Transient signals create noise in the power supply for the amplifier circuits. By

reducing the transients, less noise is present in the final signal sent to the MCA from the shaping amplifier.

The TPS7A4700 operates with an input voltage range of +3 VDC to +36 VDC. The output voltage noise is 4 µV. The power-supply ripple rejection is ≥ 55 dB. The unit can operate at output currents as high as 1 A. The unit can operate at an output voltage of +1.4 VDC to +34 VDC.

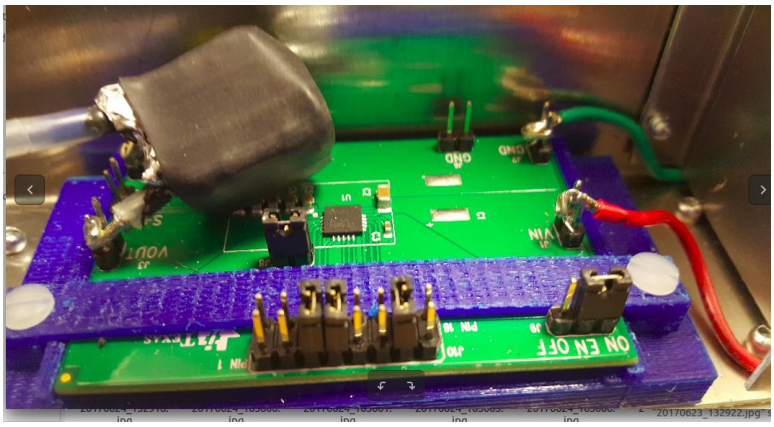

Figure 4.10: Emco Q12 (in black heatshrink) and the Texas Instruments voltage regulator circuit board

*4.4.6 Computer*

The Raspberry Pi model 3 is used to control the spectrometer and store the spectra. The Raspberry Pi runs an ARMv8-A 64 bit architecture on a Broadcom BCM2837 SoC. The CPU is a 1.2 GHz 64-bit quad-core ARM Cortex-A53. The GPU is a Broadcom VideoCore IV. SDRAM memory is 1 GB shared with the GPU.

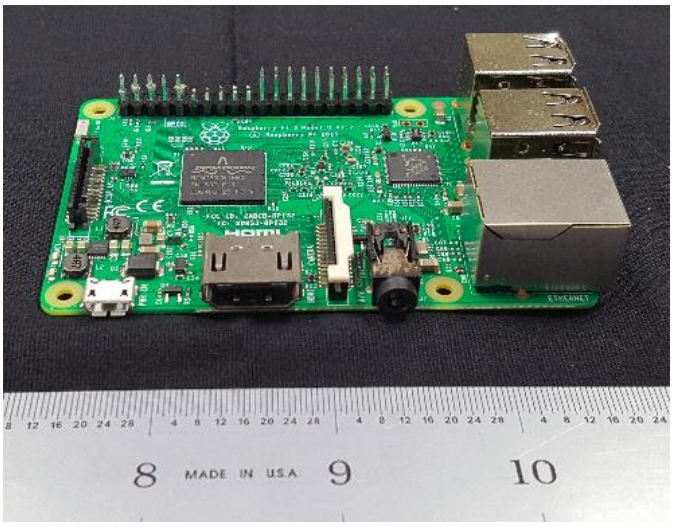

Figure 4.11: Raspberry Pi Model 3

*4.4.7 Detector Housing*

An aluminum square box purchased from Zero Manufacturing is used for the detector case. NASA required rounded smooth edges with no burrs to minimize any risks of injury to astronauts while the unit is on ISS.

By having a small housing, the lengths of all of the signal lines are minimized. Since all wires act as antennas, reducing the length of internal wires reduces the size of receiving antennas in the system. The smaller antennas minimize the noise transmitted between the internal components of ATED. The reduced noise increases SNR, which allows for low lineal energy particle detection.

The inside of the case contains substructures. Three of the substructures minimize noise in the signal's circuit: A Faraday cage surrounding the amplifier circuit, a Faraday cage surrounding the high voltage power supply, and a Faraday cage surrounding the low voltage power supplies. The OSU Physics and Chemistry machine shop was able to take

a basic design for the case's internal structures and further develop them into the current version:

Figure 4.12: ATED: top left: spectrometer, top right: computer, bottom left: amplifier, bottom middle: high voltage power regulator, bottom right: power supplies.

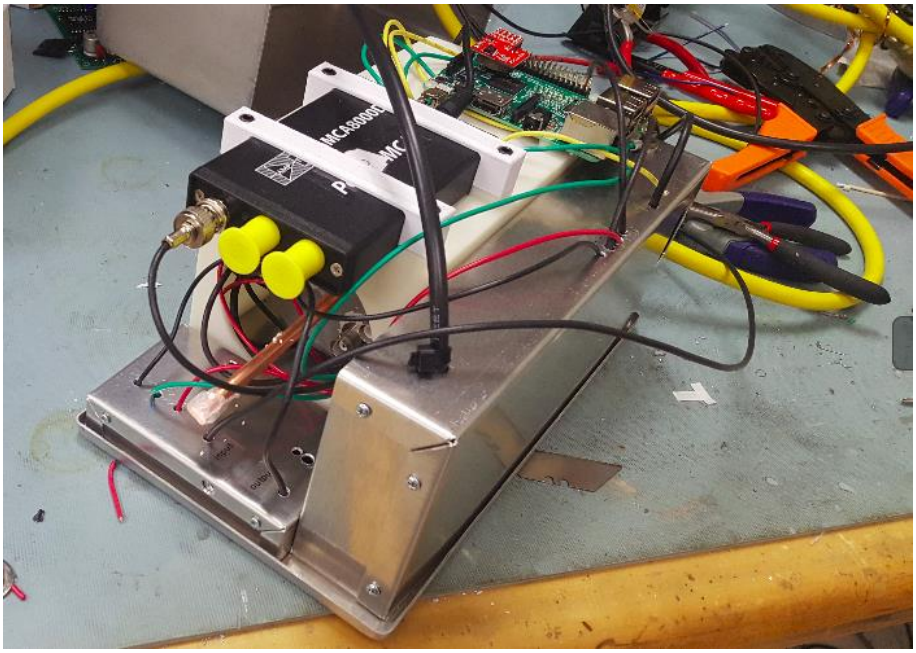

Figure 4.13: Internals of ATED model 1 with Faraday cages sealed.

### *4.4.8 Software*

#### *4.4.8.1 Operating System*

The operating system is an up-to-date Raspbian operating system downloaded from an online repository. Raspbian is a Debian-based operating system for the Raspberry Pi. Being a Linux operating system, Raspbian was able to be edited in ways that make the operating system more suitable for the ATED unit. The graphical user interface was removed. Various other components of the software are removed to limit the power consumption and processing power used by the computer while it is on the ISS.

The spectra are to be transmitted from the ISS to Earth monthly via satellite data down-link. A data down-link requires an interface between the ISS and ATED. A scheduler was written in the operating system that does the following every 24 hours: 1) copy all of the spectra from the hard drive to a folder named "raw" on the connected secure digital (SD) card, 2) copy all of the spectra into one zip file to a folder named "spectra" on the connected SD card, 3) delete all spectra on the hard drive.

#### *4.4.8.2 Software Development Kit (SDK)*

Amptek is the manufacturer of the spectrometer. Amptek supplies an SDK. This software package allows the user to control the spectrometer without the use of a graphical interface. Code was written in C++ and added to the SDK to do the following: 1) The spectrometer sends the current spectra to the computer and resets spectral data every 30 seconds, 2) the computer then saves the file to the local hard drive using time-stamp data to name the file.

*4.4.9 Detector Noise Reduction and Testing*

Noise reduction in the detector has at least five benefits: 1) fulfilling NASA requirements that mandate that electromagnetic interference (EMI) from ATED be below some threshold, 2) NASA requirements that transient noise to the power supply from ATED be below some threshold, 3) reduction in EMI from external equipment, 4) reduction in EMI between subsystems in ATED, 5) and reduction in transient noise in ATED signal path.

As shown in Figure 4.14, ATED underwent extensive EMI testing at NASA Johnson Space Center (JSC). ATED passed all EMI testing. The successful testing can be attributed in large part to the many Faraday cages surrounding every circuit in ATED's design.

NASA requires that ATED return minimal noise to the external power source. Figure 4.15 shows ATED undergoing testing to ensure the unit produced little noise and that the unit can function under varying input power conditions that may arise on ISS. The conditions tested included varying input power frequency from 50 Hz to 65 Hz, skipping a cycle of AC power, and varying input voltage from 110 VAC to 130 VAC. Measurements were taken for ATED nominal power consumption, peak power consumption, nominal current usage, peak current usage, and various other characteristics. ATED passed all tests within NASA requirements. Passing these tests can be partly attributed to the choice of power supplies and other COTS parts used in ATED. The power supplies eliminate transmission of transients back to the input power

line. The power supplies also operate over a wide range of input frequencies and voltages.

Figure 4.14: Top: RE02 Test Set up, Biconical Antenna, 100 MHz – 200 MHz, Horizontal Polarization (Left), Vertical Polarization (Right); Middle: RE02 Set up, Horn Antenna, 200 MHz - 1 GHz, Horizontal Polarization (Left), Vertical Polarization (Right); Bottom: RE02 Set up, Horn Antenna, 1 GHz – 15.5 GHz, Horizontal Polarization (Left), Vertical Polarization (Right).

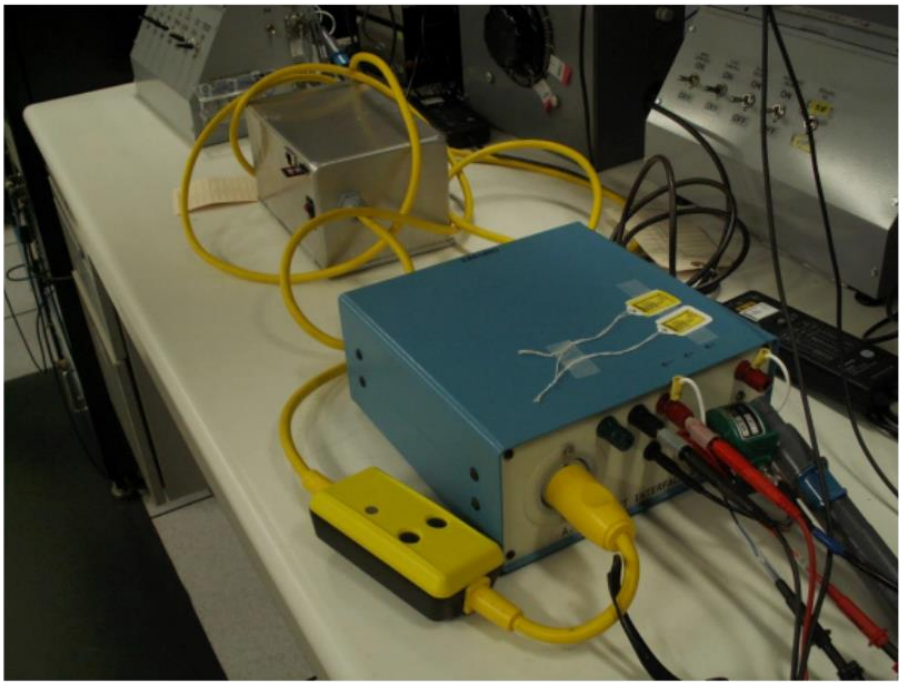

Figure 4.15: ATED at NASA JSC testing facility during various measurements and electrical characterization.

# CHAPTER V

## CHARACTERIZATION AND CALIBRATION TECHNIQUES FOR TEPC

### *5.1 Introduction*

A TEPC must be characterized and calibrated before it can make accurate dose measurements. This chapter covers the methods used to characterize and calibrate a TEPC for use as a dosimeter.

Previous prototypes of in-house TEPC detector heads were able to be opened. Opening the head allowed for calibrating the detector by inserting an americium alpha particle source, measurement of the alpha particles' lineal energies, and removal of the alpha particle source [ICRU26 1985]. Different calibration techniques are required for ATED since its detector head is a permanently sealed unit. It is standard to use a particle accelerator for high precision calibration of permanently sealed TEPC [ICRU36 1985]. Traveling to and being autorized beam time at particle accelerators for calibrating TEPC is extremely impractical. We used a calibration technique that is comparably precise to using a particle accelerator to calibrate a TEPC. This calibration technique uses readily available gamma ray sources and a neutron source. This technique eliminates the impracticalities associated with using high-energy particle accelerators to calibrate TEPC.

First, we discuss the uncertainties related to ATED dose measurements. Uncertainties in electronic signals due to the spectrometer and the amplifiers are negligible because extensive characterization and calibration of these components remove nearly all uncertainty associated with them. It is shown that the pressure and temperature of the active volume during the filling procedure produce uncertainties that require thorough analysis to ensure that dosimetric measurements are reliable enough to use a TEPC as a dosimeter. The uncertainty in the active volume radius also leads to an error in the measurement that requires correction. These uncertainties yield values of error in dose measurements. This error is well-below the standard accepted error of 15% for TEPC [Brackenbush 1990].

Next, we show a method for characterizing the Gaussian-shaping amplifier. The amplifier shows two regions that amplify signals differently: There is a linear response region and a logarithmic response region. The linear region is chosen to be used for measurements on the ISS. The linear region is nearly proportional, i.e., there is a y-intercept of approximately zero for the calibration curve relating the channel number of a measurement to the energy deposited in the detector by a measured particle. Calibration of the shaping amplifier is necessary for ATED to be used as an accurate dosimeter.

The logarithmic region needs further analysis. It is necessary to understand the underlying physics associated with the nonlinear response before using the data measured in this region. Both the stability and the counts per channel measured will require thorough investigation. However, if the COTS parts show repeatability of measurements, the logarithmic region measurements made on ISS can be analyzed for both dosimetric

and spectroscopic data after further characterization of the logarithmic response region of the shaping amplifier.

After characterization of the Gaussian amplifier, ATED was taken to the HIMAC heavy ion accelerator to perform calibration using well-characterized mono-energetic beams of fully ionized radiation. This method yields a calibration curve for lineal energy as a function of channel number on the spectrometer. Or inversely, channel number as a function of lineal energy.

The method used at HIMAC is the most accurate method for calibrating a TEPC [ICRU36 1985]. However, the original ATED was destroyed in an accident during shipping. It was infeasible to calibrate the newer ATED model at HIMAC. So, two other methods were employed to calibrate the newly built model. First, we calibrate ATED using the proton edge and electron edge measured using a neutron source. Then a newer method is found for a calibration that is approximately as accurate as the method used at HIMAC: using the proton edge as measured from a neutron source and the electron edge as measured from a gamma ray source.

Calibrating ATED using the proton edge of a neutron source and the electron edge from gamma ray sources yields a y-intercept in the lineal energy to channel number calibration curve that is almost identical to the results from the calibration technique that was used at HIMAC. We examine the underlying physics that describe why the new technique is more accurate than the calibration technique using only a neutron source for both the electron edge and the proton edge. The new calibration technique using a gamma

ray source and neutron source is more practical than using an accelerator for calibrating TEPC.

*5.2 Defining Uncertainties in ATED*

There is uncertainty associated with the analog to digital conversion in the spectrometer in ATED. There is also uncertainty associated with pulse height in the amplifier portion of ATED. The uncertainties associated with the electronics are reduced to a level that is insignificant by calibration

There are several sources of error in TEPC dosimetric measurements that cannot be calibrated. The main sources of error in TEPC dosimetric measurements come from the uncertainties in the active volume of the detector. The detector head is filled with tissue equivalent gas at 2666 ± 133 Pa (5.20 ± 0.5 Torr) at a temperature of 295 ± 2 K. The radius of the spherical active volume is 35.5 ± 0.5mm.

Let us define absorbed dose in terms of these measurements to find the uncertainty in dosimetric measurements. Absorbed dose is a measure of energy deposited in a system by ionizing radiation divided by the mass of the system [ICRU36 1985]:

$$D = \frac{\epsilon}{m}, \tag{5.1}$$

where $\epsilon$ is the energy deposited in the system and $m$ is the mass of the system. For an isotropic radiation field, $\epsilon$ will be the average energy deposited by $N$ particles passing through a mass.

$$\epsilon = N\bar{\epsilon}, \tag{5.2}$$

where $\bar{\epsilon}$ is the average energy deposited by the *N* particles passing through the system. $\bar{\epsilon}$ is the product of lineal energy, *y (keV/μm),* and the average chord length, $\bar{l}(\mu m)$.

$$\bar{\epsilon} = y\bar{l} \tag{5.3}$$

in units of keV. $\bar{l}$ is 2/3 of the simulated diameter for the spherical active volume of ATED. Substituting Equation 5.3 into Equation 5.2, and substituting that result into Equation 5.1 yields a dose measurement of:

$$D = \frac{Ny\bar{l}}{m}. \tag{5.4}$$

*N* and *y* are known to high precision by characterization and calibration of the instrument. The uncertainties in dose measurements are due to the uncertainties in the simulated volume and the uncertainties of the mass of the TE gas in the active volume of the detector head. With uncertainties, absorbed dose is:

$$D = \frac{Ny\bar{l}}{m} \pm \frac{\delta D}{|D|}, \tag{5.5}$$

where $\frac{\delta D}{|D|}$ is the relative uncertainty in the dose measurement. The uncertainty is defined as [Kline 1985]:

$$\frac{\delta D}{|D|} = \sqrt{(\frac{\delta \bar{l}}{|\bar{l}|})^2 + (\frac{\delta m}{|m|})^2}\ , \tag{5.6}$$

where $\frac{\delta \bar{l}}{|\bar{l}|}$ is the relative uncertainty in the mean chord length of the simulated volume and $\frac{\delta m}{|m|}$ is the relative uncertainty in the mas of the gas in the active volume of the detector.

*5.2.1 Uncertainty in Mass*

We must find the mass of the TE gas in the active volume of a TEPC to define the uncertainty in dosimetric measurements. Mass of a system can be defined as the number of molecules, *n*, multiplied by the average mass, $m_{avg}$, of the molecules of the system:

$$m = n * m_{avg} . \tag{5.7}$$

To find the mass of the gas in the active volume we need to know how many particles are in the sphere at the given pressure and temperature during the filling process of the detector head. The ideal gas law can be used to find the number of moles within the active volume of ATED:

$$n = \frac{P\,V}{R\,T}, \tag{5.8}$$

where *n* is the number of moles in volume, *V*, at temperature, *T*, and pressure, *P*. *R* is the universal gas constant. Uncertainty in the number of particles in the active volume is thus dependent on the uncertainty in the pressure of the detector, the temperature of the detector when, filled with gas, and the dimensions of the active volume. The relative error in the number of moles is calculated to be 5% [Kline 1985]. The number of moles in the active volume of ATED is:

$$n = 2.02 * 10^{-4} \pm 1.* 10^{-5}\, mol. \tag{5.9}$$

The TE gas consists of carbon dioxide, methane, and nitrogen with respective molar concentrations of 29.99%, 67.29%, and 2.751%. The respective molar masses for these molecules are 44.01 g/mol, 16.04 g/mol, and 14.01 g/mol. The molar mass values

are known to a precision that negates the need to include their uncertainty in the error propagation of ATED dose measurements. A total molar mass for the TE gas is:

$$m_{mol} = 24.37 \frac{g}{mol}, \tag{5.10}$$

which gives a total mass of the gas of:

$$m = n * m_{mol} = 4.90 * 10^{-6} \pm 2.5 * 10^{-7} kg. \tag{5.11}$$

This calculation yields a relative uncertainty in mass of approximately 5%:

$$\frac{dm}{|m|} \sim 5\%. \tag{5.12}$$

*5.2.2 Uncertainty in the Simulated Average Chord Length*

We next derive the uncertainty in dosimetric measurements due to uncertainty in the simulated average chord length of the TEPC. The average chord length for a spherical TEPC is 2/3 of the diameter of the simulated active volume.

*5.2.2.2 Uncertainty in Simulated Average Chord Length*

Density is mass over volume.

$$\rho_g = \frac{m_g}{v_g}. \tag{5.28}$$

Substituting Equation 5.28 into Equation 3.18:

$$\mathrm{d}_w = \frac{m_g}{v_g}\, \mathrm{d}_g\, . \tag{5.29}$$

Calculating uncertainty in Equation 5.29 due to mass and radius of the active volume of the detector yields a result for the diameter of the simulated spherical tissue [Kline 1985]:

$$\mathrm{d}_w = 2.0 \pm 0.09\ \mu m, \tag{5.30}$$

which yields a value for the average chord length:

$$\bar{l}_w = 1.33 \pm 0.09\ \mu m\ . \tag{5.31}$$

The relative uncertainty in the average chord length is approximately:

$$\frac{d\bar{l}}{|\bar{l}|} \sim 6.8\% \tag{5.32}$$

*5.2.3 Uncertainty in Absorbed Dose*

The absorbed dose, D, with a propagated error for a TEPC is given by Equation 5.33:

$$D = \frac{Ny\bar{l}}{m} \pm \frac{\delta D}{|D|}, \tag{5.33}$$

where the uncertainty in measured absorbed dose, $\frac{\delta D}{|D|}$, is found by inserting equations 5.12 and 5.32 into equation 5.6. This yields a total relative uncertainty in absorbed dose measurements of approximately 8.4%.

*5.2.4 Uncertainty in Dose Equivalent*

Dose equivalent is defined as absorbed dose, *D,* multiplied by a quality factor, *Q(y).* The uncertainty in the quality factor is negligible compared to the uncertainties defined above for absorbed dose; the relative uncertainty in measured dose equivalent is

equal to the relative uncertainty in the measured absorbed dose for ATED; the relative uncertainty in dose equivalent measurements made by ATED is approximately 8.4%.

### *5.3 Amplifier Circuit Gain Adjustment Testing*

To correctly measure absorbed dose, a TEPC should be able to measure deposited energy from the entire lineal energy spectrum. Every dosimeter is limited in the range of energies it can detect. This limitation makes it necessary to optimize the range of energies able to be detected to maximize the particles detected, which, in turn, requires calibration and characterization for the amplification circuitry associated with the dosimeter. Characterization of the amplifier gain control was done before exposing ATED to radiation sources to expedite the process of finding the optimal gain settings and maximizing useful particle accelerator beam time.

It is important to consider the effects of finding the optimal gain settings because there are benefits and shortcomings of both high gain and low gain settings in a TEPC. A high gain setting on the amplifier circuit yields better resolution for the particles with low lineal energy. However, larger amplification of the signal also removes particles with high lineal energy from the spectrum, because of the electronic clipping that occurs in the amplifier. A low gain setting allows particles with higher lineal energy to be detected. The measurements of particles with low lineal energy are lost because the counts are stored in the portion of the spectrum associated with noise when using low gain settings.

A BNC PB-5 pulse generator was connected to the amplifier circuit input to characterize the amplifier. The amplifier circuit amplifies signal pulses of known voltage amplitude. The output of the amplifier was connected to an Amptek MCA-8000D and

read out on a laptop as shown in Figure 5.1. The spectrometer converts the analog signal from the amplifier to a channel number based on pulse height (The pulse height is approximately proportional to the channel number). The fine-gain control is turned 180$^o$ clockwise, and then the channel number is again read out on the computer. The gain is then turned 180$^o$ counter-clockwise to its original orientation. The amplitude of the signal from the pulse generator was increased, and the process repeated 22 times. This result yields channel number increase as a function of starting channel number for a 180$^o$ clockwise turn of the fine gain:

$$\Delta ch(ch_i) = 0.063 * ch_i + 2.2 \tag{5.34}$$

where $\Delta ch$ is the increase in channel number from the original gain setting, and $ch_i$ is the channel number in the original gain setting. Having this result allows for much quicker calibration time during radiation source exposure because precise peak location adjustments can be made more quickly between exposures.

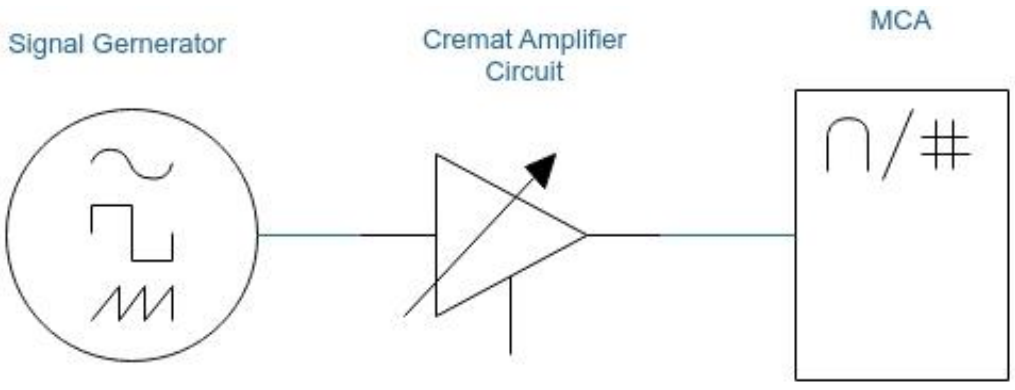


Figure 5.1: System setup for amplifier characterization. The signal path is from left to right in the figure.

*5.4 A Method for Characterization of Gaussian Pulse Shaping Amplifiers with Non-linear Amplification Regions*

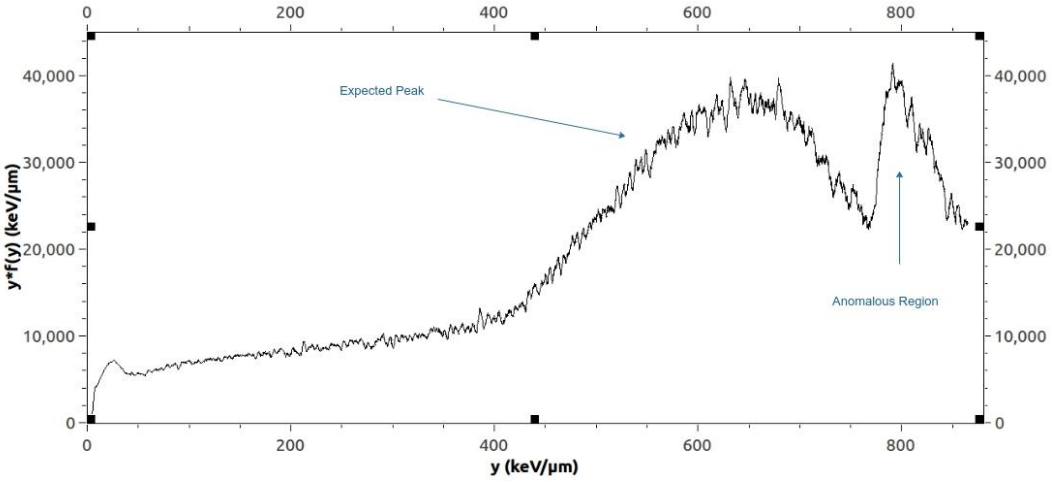


Figure 5.2: 422 MeV Fe incident on plastic equivalent to 60.32 mm of $H_20$. One main peak is expected. The anomalous region is indicative of the non-linear response of the amplification circuitry.

Figure 5.2 shows an anomaly in the high LET region of the spectra measured by ATED. An experiment is set up to test the shaping amplifier's response to input pulses. The experimental setup is shown in Figure 5.3. A pulse generator was connected to the Gaussian shaping amplifier circuit of the TEPC. The pulse generator sent signals of twenty-seven known pulse heights to the amplifier. The amplifier reshaped and amplified the signals, which were stored as a spectrum in the spectrometer. This spectrum consists of twenty-seven peaks vs. channel number. A plot of the data is shown in Figures 5.4, 5.5, and 5.6.

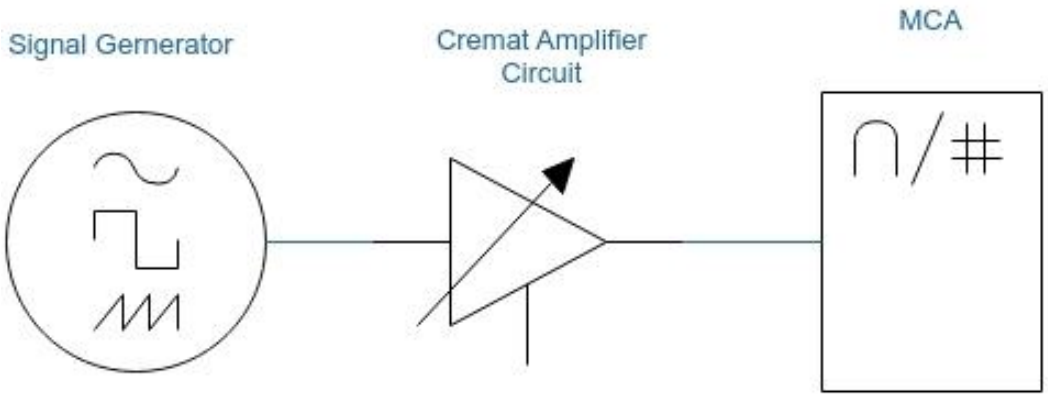


Figure 5.3: A pulse generator is connected to the Gaussian shaping Amplifier. The output of the amplifier is connected to the spectrometer.

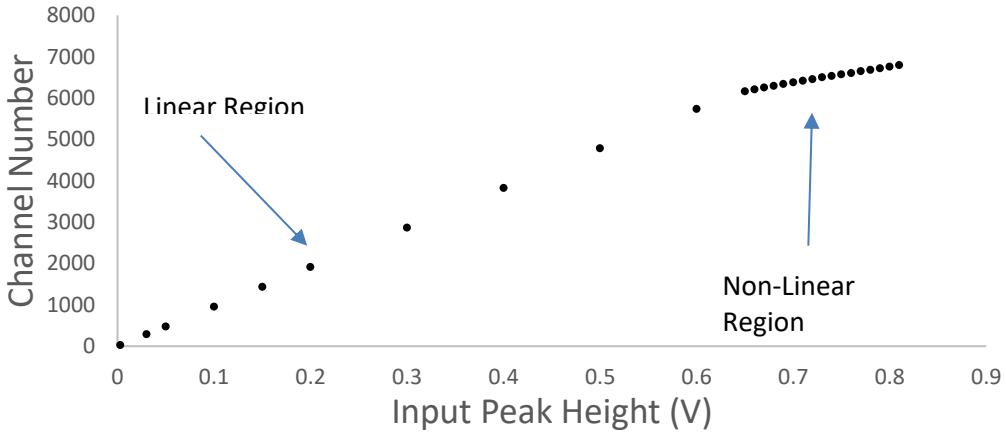


Figure 5.4: Spectrometer channel number versus input peak height from a pulse generator.

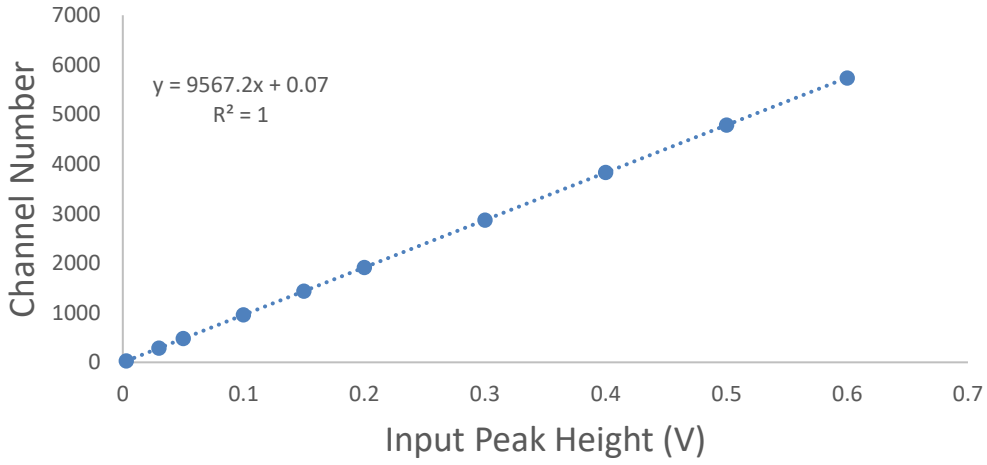


Figure 5.5: Linear region of the Gaussian-shaping amplifier.

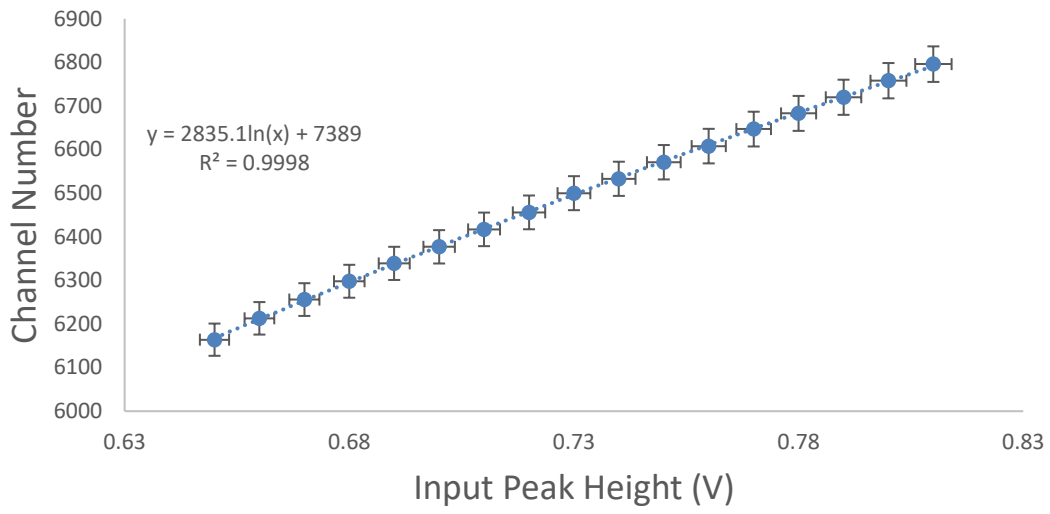


Figure 5.6: Logarithmic response region of the Gaussian-shaping amplifier.

The result is a piecewise relationship between channel number and input voltage. The input voltage is shown to be nearly proportional to the channel number in the linear region. The same y-intercept of 0.07 is also shown in section 5.5.1 to occur during calibration using a beamline. It is technically possible to correct this offset. However, an amplifier with the precision required to correct for this would be costly. Moreover, the characterization/calibration of the unit eliminates the need for a physical correction because software handles this correction automatically when converting spectrum measurements to dose. The linear region of the amplifier will be used for measurements with ATED while on the International Space Station. The logarithmic region should be studied more. Since the amplifier is proprietary, it is not possible to study the underlying physical properties of the circuitry that are causing the nonlinearity in the measurements. However, characterization of the stability should be thoroughly examined. If the logarithmic region yields repeatable results, then the relationship between counts and dose should be studied.

*5.5 Calibration*

*5.5.1 Mono-energetic beamline calibration*

The most precise method for calibrating a TEPC is to expose the TEPC to beams of mono-energetic ions at an accelerator and using the peaks of the spectra from these exposures as calibration points [ICRU36 1985, Rossi 1996]. ATED is exposed to three beamlines at HIMAC: 500 MeV Fe, 490 MeV Si, and 290 MeV C with respective lineal energies of 303 keV/µm, 85.5 keV/µm, and 17.6 keV/µm as shown in Figure 5.7.

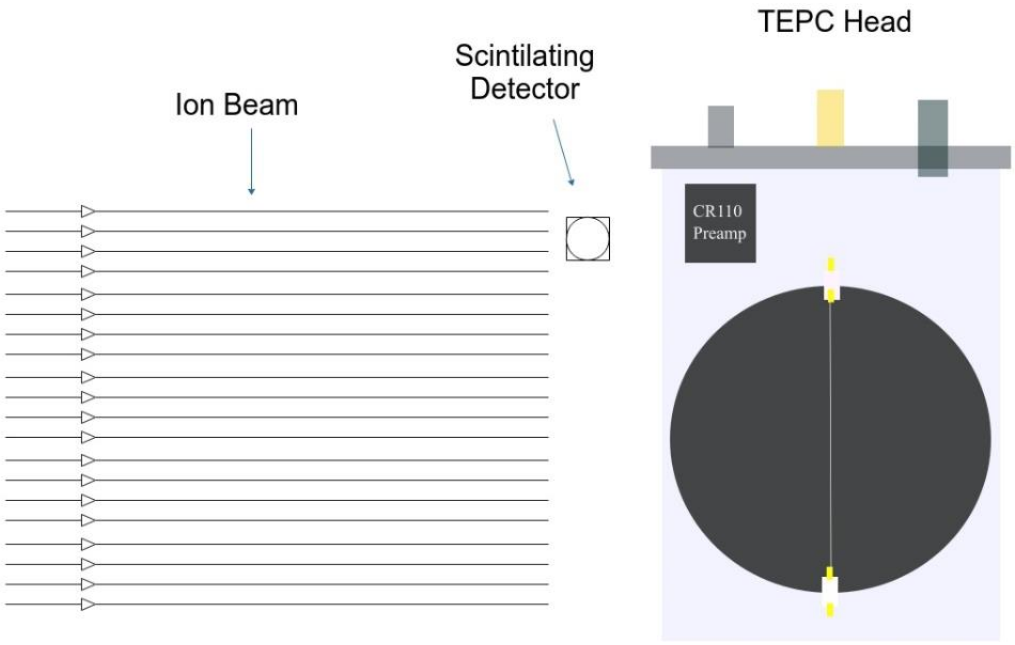


Figure 5.7: Representation of ion beam exposure at HIMAC. A scintillator counts total fluence (ion/cm2) during measurements for dose measurement comparison.

Gaussian distributions are fit to the peaks. The channel number of the peaks of the Gaussian distributions are chosen to be the channel number associated with the lineal energy of the beam. This yields a linear relationship between the known lineal energies of the beams and the channel number of the peak [ICRU36 1985, Rossi 1996].

The relationship between the lineal energy of the beams and the peak channel number of the measurements of the beams is shown in Figure 5.14. This method yields a result of nearly perfect proportionality between the lineal energy of a mono-energetic beam and measured peak height of y(ch) = 0.129*ch+0.0665 with an $R^2$ = 0.99999. The magnitude of the slope is scaled by the amplification settings used for these measurements. Increasing or decreasing the magnitude of the amplifier will increase or decrease the slope of the calibration curve, respectively.

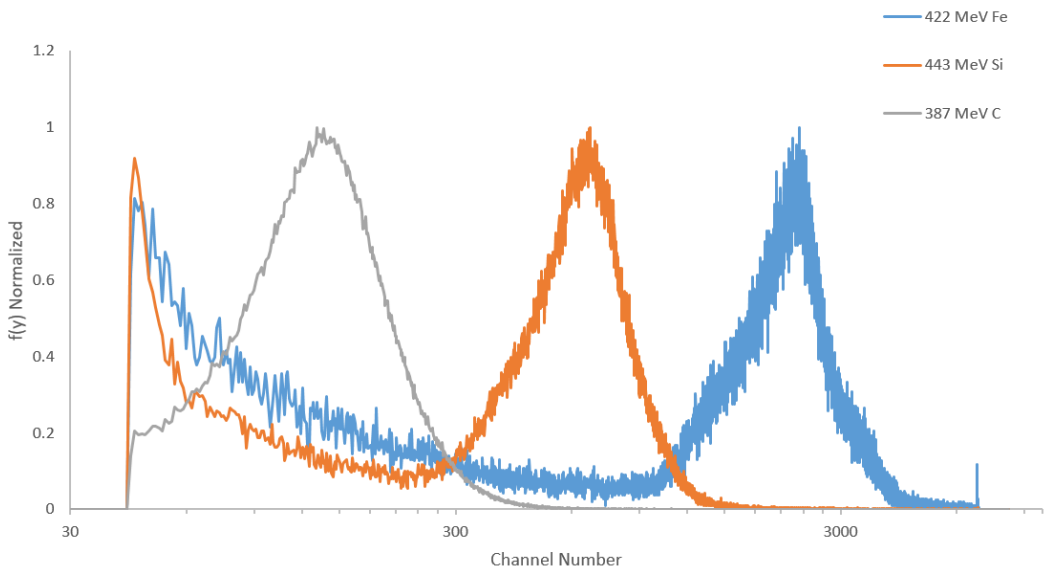


Figure 5.8: ATED measurements of three beamlines at HIMAC. Gaussian distributions are fit to yield the channel number of the peaks: 500 MeV Fe, 490 MeV Si, and 290 MeV C peaks at channel numbers 2340, 660, and 135, respectively.

### *5.5.2 Proton Edge and Electron Edge Calibration Using a Neutron Source*

Particles have a theoretical maximum amount of energy that they can deposit into a given volume of matter. In the case of protons, the maximum value is a lineal energy of y = 147 keV/μm [ICRU36 1985]. The maximum energy an electron can deposit is

approximately 12 keV/µm [Moro 2015]. In principle, a radiation source that can generate these energies of protons and electrons can be used to calibrate a TEPC [Moro 2015, Rossi 1996]. Producing a mono-energetic beam with the maximum lineal energy for electrons or protons is not practical. However, a neutron source can be used to interact with the nuclei in the TE wall of the TEPC to produce recoil protons [ICRU36 1985, Gersey 2018]. The resulting spectrum contains characteristics associated with the maximum lineal energies for electrons and protons: the electron edge and the proton edge [Gersey 2018, Rossi 1996, Moro 2015].

The energy spectrum from the ionization processes will have lineal energies from very low lineal energies up to the 147 keV/µm [ICRU 36, Rossi 1996]. Gamma rays produced during these interactions will also ionize the gas. The ionization process imparts a theoretical maximum lineal energy to electrons in the gas; the electrons have a spectrum of lineal energies ranging from some minimum to the maximum of approximately 12 keV/µm [Moro 2015].

As depicted in Figure 5.10, we use a plutonium-beryllium (PuBe) neutron source with an activity of approximately 220 mCi to obtain the proton and electron edges. The neutrons from the PuBe source have an average energy of 4.5 MeV. ATED is exposed to the PuBe source for ~13 hours. The neutron source is located 10 ± 0.4 cm from the center of the spherical active volume of ATED.

For neutron energies below 15 MeV, maximum energy is transferred during an interaction in elastic scattering of nuclei with a mass similar to the mass of the neutron [ICRU36 1985]. The TE plastic in the detector head is acrylic [$(C_5O_2H_8)_n$] which contains

a high density of protons, which have a similar mass to neutrons. Interactions between incident low-energy neutrons and the TE plastic lead to proton recoils (ejection of protons from the plastic into the active volume of the gas) [NCRP116 1993]. These protons ionize the gas in the active volume as shown in Figure 5.9.

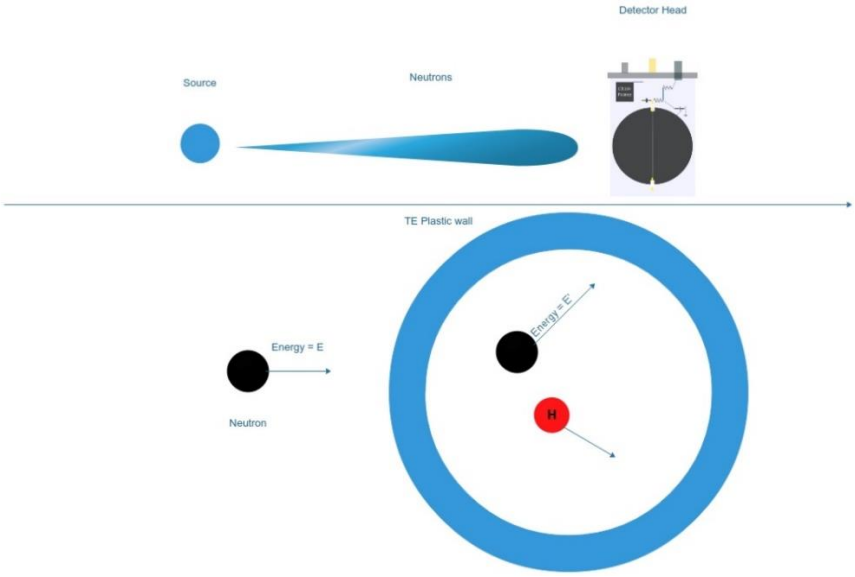


Figure 5.9: Top: A neutron source is used to irradiate the active volume of ATED. Bottom: Proton recoil occurring when an incident neutron elastically collides with a hydrogen nucleus (proton) in the wall of the TEPC active volume.

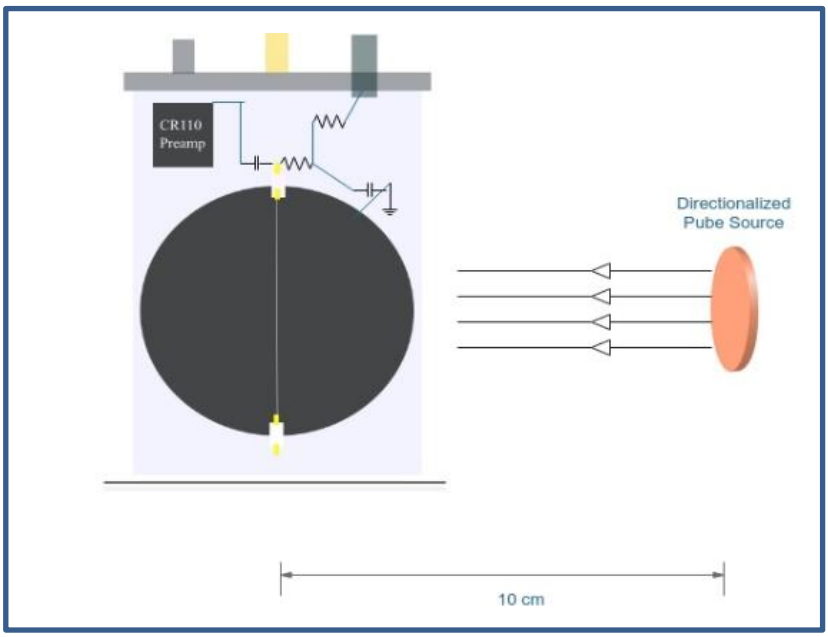


Figure 5.10: A diagram of the measurement orientation for obtaining a spectrum from the PuBe source using ATED.

*5.5.3 Electron edge using gamma source*

The electron edge can also be found using gamma ray sources. Gamma rays ionize the gas in the active volume of the detector. The electrons have lineal energies from some minimum (below the threshold of ATED detection) to some maximum value (~12 keV/µm) as described above [Moro 2015].

ATED was exposed to radioactive gamma ray sources for 5.25 hours. The resulting spectrum is shown in Figure 5.13. The electron edge from this measurement is used to find the channel number that corresponds to a lineal energy of 12 keV/µm [Moro 2015].

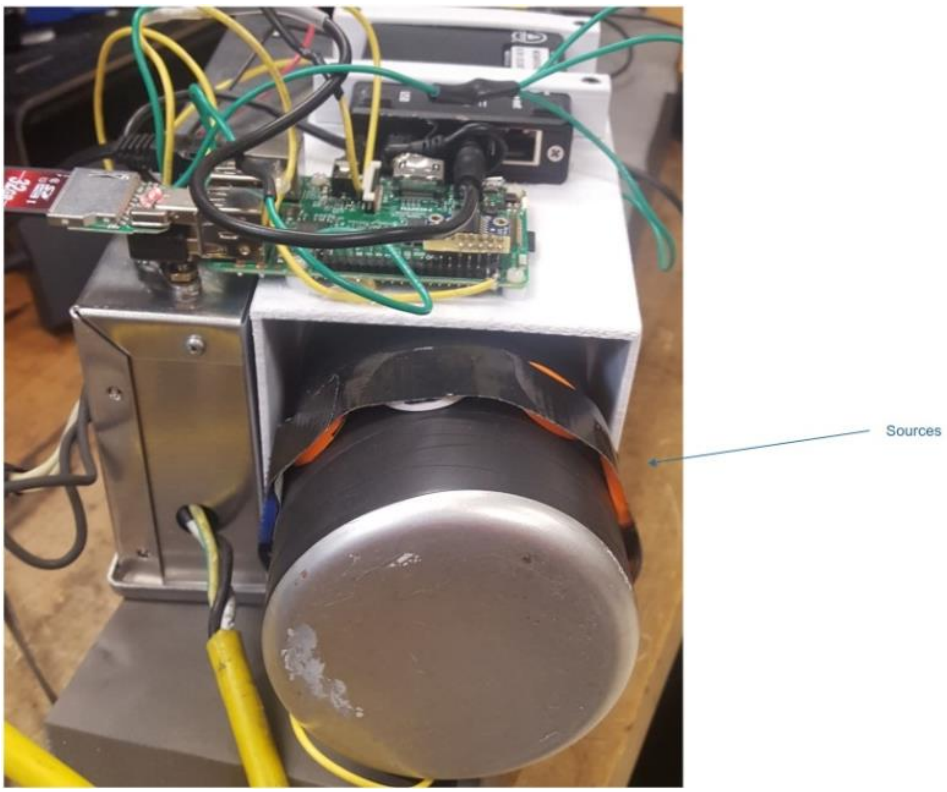


Figure 5.11: ATED electron edge calibration. ATED during measurement of the electron edge. There are 10 gamma sources ranging from 0.1-10uCi taped to the detector head.

## *5.6 Results*

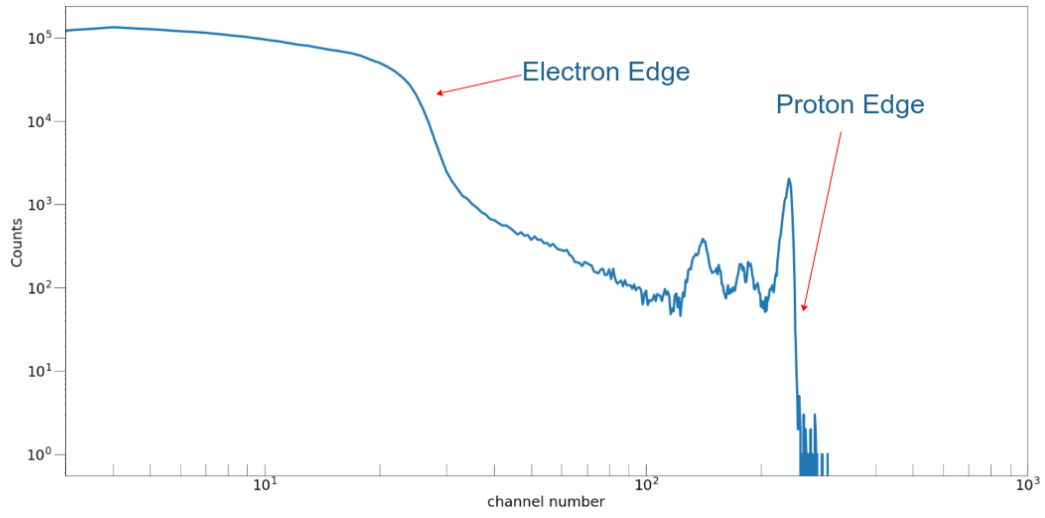


Figure 5.12: The spectrum from the neutron exposure calibration experiment showing the location of the electron edge and proton edge for the calibration method used for ATED. The electron edge occurs at approximately channel 28. The proton edge is at approximately channel 247.

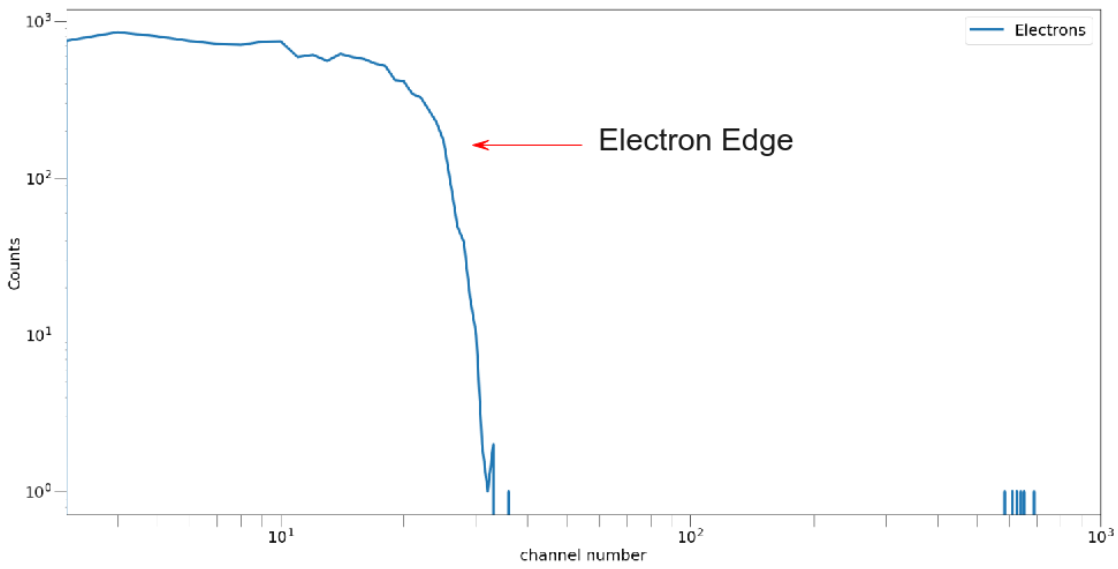


Figure 5.13: The spectrum from the gamma source exposure calibration experiment showing the location of the electron edge for the calibration method used for ATED. The electron edge occurs at approximately channel 20.

The integrated spectrum yields the calibration points. The proton edge calibration point is the channel on the counts versus channel number plot corresponding to an output of half of the maximum value, as shown in Figure 5.12 [Gersey 2018, Lucas 2018, ICRU36 1985]. This method is used for the electron edge, as well. Using the electron edge and proton edge from the neutron experiment yields channel number as a function of lineal energy as:

$$\mathrm{ch(y)} = 1.61 * \mathrm{y} + 8.55 \tag{5.35}$$

or inversely, lineal energy as a function of channel number as:

$$\mathrm{y(ch)} = 0.62 * \mathrm{ch} - 5.3. \tag{5.36}$$

Using the proton edge from the neutron experiment and the electron edge from the gamma experiment yields the following two results:

$$y(ch) = 0.59 * ch + 0.11 \quad (5.37)$$

$$ch(y) = 1.69 * y - 0.19. \quad (5.38)$$

The June 2017 HIMAC data yields channel number as a function of lineal energy

$$ch(y) = 7.72 * y - 0.51, \quad (5.39)$$

and lineal energy as a function of channel number as

$$y(ch) = 0.129 * ch + 0.07. \quad (5.40)$$

To compare the results we look at the calibration curves for lineal energy as a function of channel number for the three methods, as seen in Figure 5.15. The differences in slope between the results of the HIMAC data and the gamma/neutron experiment are due to intentionally setting the gains at different values. The amplifier gain settings were unchanged between the calibration using the neutron source and the gamma source. The slope for the calibration curves between both methods using the neutron source should be the same since the gain is unchanged. The two methods result in different slopes for their respective calibration curves. The differing slopes imply that at least one of the two methods using the neutron source yields an incorrect calibration fit between channel number of the spectrometer and the lineal energy of incident radiation.

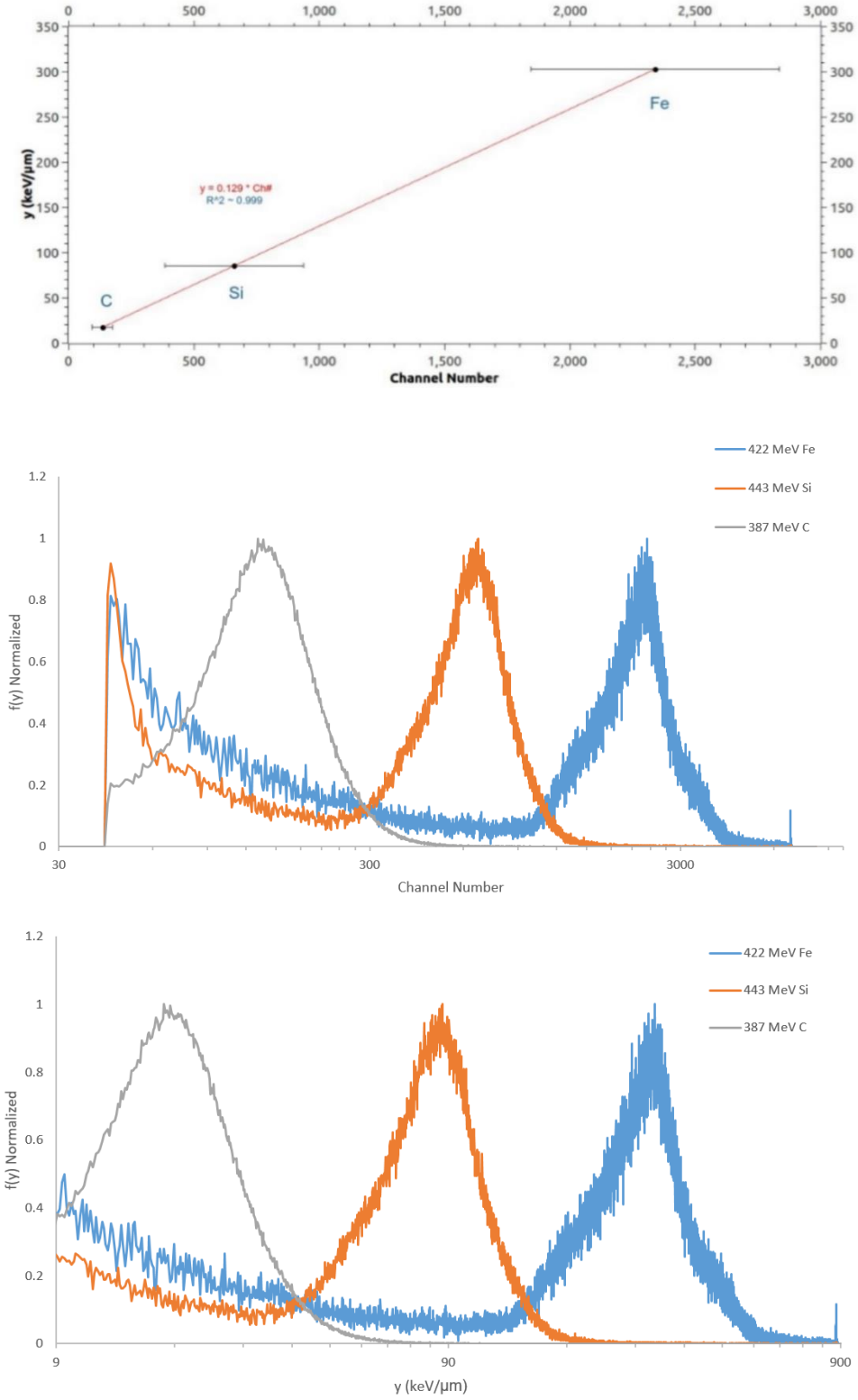


Figure 5.14: HIMAC calibration technique results. Top: the relationship of known beam lineal energy and the channel number of the corresponding peak. Middle: The initial measurements of normalized counts of the beams vs. channel number. Bottom: The same measurements after converting channel number to lineal energy via the calibration curve in the top of this figure.

In terms of the intercept of the calibration functions, using the electron edge from a gamma source and the proton edge from a neutron source yields results that are comparable to using nearly mono-energetic beams for calibrating TEPC. The calibration technique using both a neutron source and gamma ray sources agrees with the calibration results of the mono-energetic beam technique. There are two significant implications from these results. First, the calibration technique utilizing the neutron source and the gamma ray source is more practical for a calibration technique than using large accelerators for calibration of TEPC. Also, the method for calibration incorporating both the neutron source measurements and the gamma source measurements produce more accurate results than the neutron source only calibration technique.

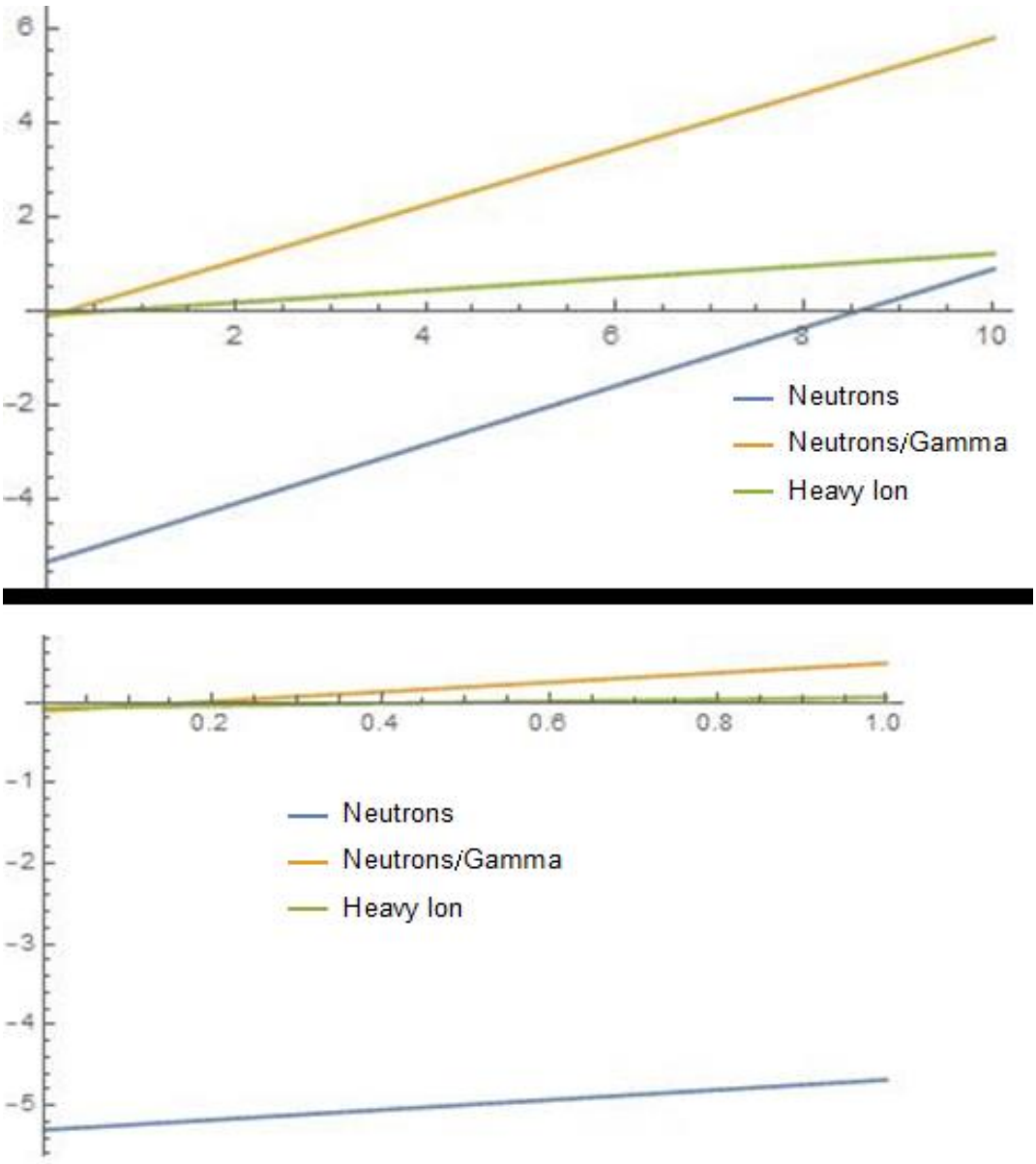


Figure 5.15: Top: calibration curves for the three calibration experiments. The slopes are a function of the amplification. Both calibration techniques that use neutrons had the same amplifier settings. However, the slopes for the two are slightly different. Moreover, the intercept is noticeably different between the two. However, the intercepts for the Neutrons/Gamma technique and the Heavy Ion technique are almost identical. This is made obvious in the bottom expanded representation of the calibration curves. This is an indication that there is an inherent problem with the neutron only technique when including the electron edge.

The problem with the calibration technique that only requires the neutron source arises from the inherent issues of using the neutron source to make an electron edge measurement. The neutron source's apparent electron edge has been shifted by incident

radiation with lineal energy greater than 12 keV/µm. The shifted electron edge can be explained by the superposition of signals that occurs in the neutron calibration technique. The neutrons from the PuBe source interact with the detector to produce charged particles with lineal energy ranging from less than 12 keV/µm to a maximum of 147 keV/µm. The integrated spectrum contains measurements of particles throughout this range[ICRU36 1985, Rossi 1996, Gersey 2018, Lucas 2018].

Let us examine a basic case of superposition to gain a better understanding of how this would shift the apparent electron edge associated with the neutron source. Figure 5.16 is a plot of two Gaussian distributions along with the summation of the two distributions. The result of the summation of the distributions is a distribution that has a peak that is shifted from the peak locations of both of its constituents. Superposition is the principle by which the electron edge in the neutron source integrated spectrum is shifted by measurements of ionizing radiation with lineal energy higher than the 12 keV/µm. The channel number associated with the 12 keV/µm maximum energy electrons can deposit in the detector volume is lost due to superposition.

Superposition does not shift the electron edge in the integrated spectrum of the gamma source because the gamma ray source cannot produce ionizing radiation with lineal energy higher than 12 keV/µm.

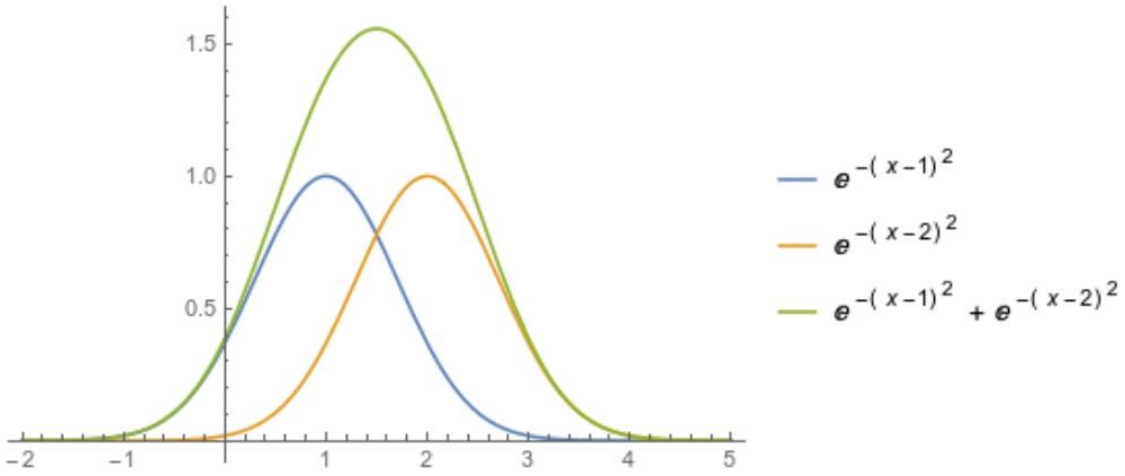


Figure 5.16: superposition of two Gaussian distributions. The summation of the two smaller distributions has a peak shifted from the location of both of its constituent parts. This is the principle by which the electron edge is being masked in the neutron source integrated spectrum.

*5.7 Conclusion*

ATED is capable of making accurate dosimetric measurements now that it is thoroughly characterized and calibrated. The uncertainties in ATED dose measurements have been thoroughly examined. Two major contributing factors to error are the temperature and pressure of the detector head during the gas-filling procedure. The other major contributing factor to dose measurements in ATED is the radius of the active volume within the detector. These factors lead to a final uncertainty in absorbed dose measurements that is shown to be approximately 8.4%.

Characterization of the Gaussian-shaping amplifier has shown two regions of amplification: a linear region and a non-linear region. The linear region is characterized and calibrated sufficiently to allow for resolved dose measurements of particles with lineal energies in the range of 1 keV/µm to 3000 keV/µm. The nonlinear region of this type of amplifier should be further investigated. A proper characterization of the

amplifier could lead to the upper end of the range of measured particles to exceed 4000 keV/μm.

The detection of particles with ultra-low lineal energy is a novel achievement of this detector. Detection of is, in part, because of the amplifier. However, much of this has to do with the design of the system. Noise issues were a great feat to overcome. Months were spent redesigning and reimagining the construction and structure of ATED. The noise was entering the analog signal path from external sources as well as from the power supplies within ATED. As shown in Chapter 4, all of the analog components of ATED are completely encompassed in grounded faraday cages. All analog signals are transmitted through a coaxial cable that is grounded to each of the components to which it is connected. The coaxial cable eliminates any external signals from interfering with the analog signal; this eliminates noise from entering the analog signal path and allows for low lineal energy particles to be detected. All power supplies are in separate Faraday cages. The Faraday cages eliminate any transmitted signals from these components from escaping and entering the analog signal path; this eliminates EMI noise from being transmitted by the power supplies. A star-ground system is used as well. The star ground scaled the noise to $1/5^{th}$ of its previous amplitude. Various orientations of grounding schemes were tested. The current grounding topology scaled the noise to ½ of its previous amplitude. The final resultant noise level was reduced to approximately $1/1000^{th}$ of the original design.

Calibration of ATED was performed using three different techniques: using high-energy particle accelerators, using a neutron source, and using a combination of a neutron source and gamma ray source. The technique using only a neutron source for

calibration is shown to have inadequacies. Basic principles of superposition of lineal energy measurements are used to describe the underlying physical problems associated with this method. The method of using a neutron source for the proton edge and a gamma source for the electron edge has been shown to be as accurate as the technique requiring the use of hard-to-come-by beam time at a high-energy particle accelerator. This method removes all of the impractical aspects associated with using a particle accelerator for calibrating TEPC [Moro 2015].

# CHAPTER VI

## RESULTS

ATED is a TEPC that can measure particles with lineal energies ranging from 1-3000 keV/µm. ATED consists of a tissue equivalent active detector head, a preamplifier, a Gaussian shaping amplifier, a spectrometer and a computer. The main components of ATED required extensive calibration and characterization to achieve such capabilities.

The software development kit for the spectrometer required extensive rewriting to ensure a maximum lineal energy range is detected while minimizing the noise. The controlling software was written and optimized to ensure that the unit accurately timestamps the spectra. A scheduler was also implemented to store the spectra on an external SD card daily. Though not quantifiable, the software and optimizations of the software allow for ATED to operate stand-alone as a fully embedded system.

The hardware design allows for measurement of particles with ultra-low lineal energy. The many faraday cages and grounding schemes inside ATED reduce the noise to a level which allows for measurement of 1 keV/µm particles.

Three main particle accelerator experiments were used to characterize and calibrate ATED: 1) a proof-of-concept examination of the hardware at Los Alamos

National Laboratory (LANL) in January 2017, 2) gain calibration, characterization, and optimization at HIMAC heavy ion accelerator in Chiba, Japan in February and March of 2017, and 3) dosimetric characterization and calibration at HIMAC heavy ion accelerator in Chiba, Japan in June 2017.

*6.1 Los Alamos*

The first prototype was tested at the Los Alamos Neutron Science Center (LANSC) pulsed spallation source at Los Alamos National Laboratory (LANL). The neutron energy spectrum of the beam-line is similar to that at aviation altitudes. The experiment is used to allow for an understanding of TEPC use and to gain a better understanding of the power distribution system of the TEPC.

During the experiment, the detector head was exposed to the beamline while the supporting electronics were placed out of the beamline to minimize any damage to the electronics from the intense neutron source. The beamline used is 30L (signifying the beamline is 30 degrees to the left of the 800 MeV proton beam used to create the spallation source). Shielding is placed in front of the detector head on some runs to shift the spectrum. The shielding is either aluminum, polyethylene, or both. Both the aluminum and polyethylene are approximately 5 g/cm$^2$. Two detector heads were used to compare data: a detector head with the traditional A150 spherical shell wall, and a detector head with an acrylic spherical shell wall.

This experiment yielded one main result beyond the proof-of-concept: an overhaul of the power system design was necessary to move forward with experimentation. The power supply used was overloaded. Overloading the power supply

resulted in an over-current in the circuitry of the high voltage bus. This over-current melted the signal leads in one of the preamplifiers.

### *6.1.1 Acrylic Active Volume*

Figure 6.1 shows measurements using the detector head with a 3mm acrylic wall surrounding the active volume of the detector. The high peaks below channel 1000 are noise. There is a peak near the far right end of the no shielding measurement. This peak moves to the left as shielding is increased in the beamline.

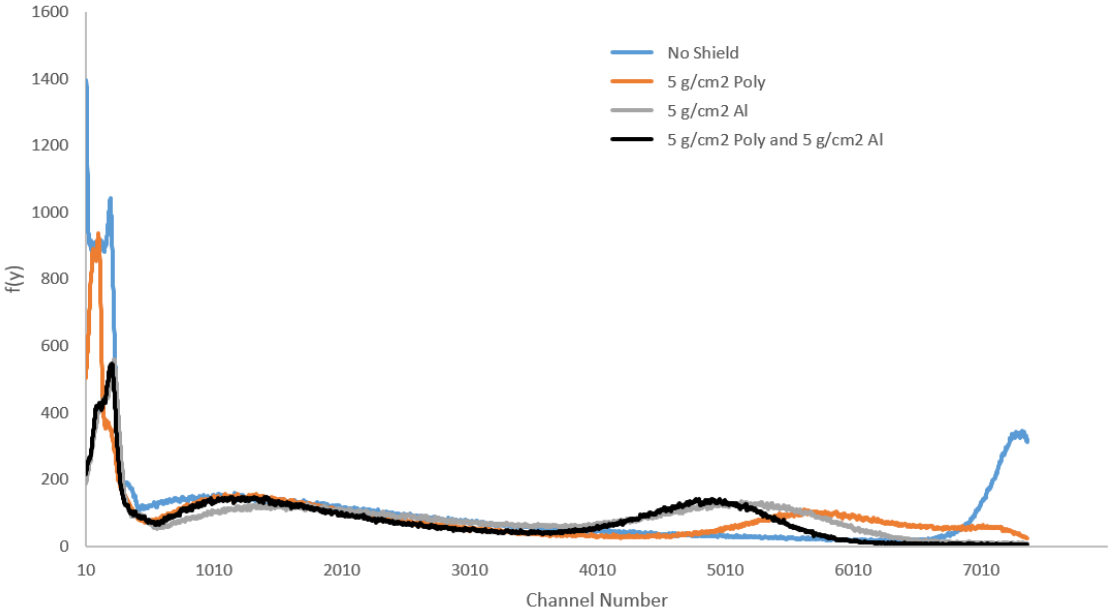


Figure 6.1: Lin-Lin plot of the Acrylic detector head exposures at LANSCE as measured by an ATED prototype.

### *6.1.2 A150 Active Volume*

Figure 6.2 shows measurements using the detector head with a 3mm A150 plastic wall surrounding the active volume of the detector. The high peaks below channel 1000 are noise. The counts vary between the spectra because the beamline was unstable. The

beamline produced approximately five times the flux during the measurement with the added shielding than it did during the measurement with no shielding.

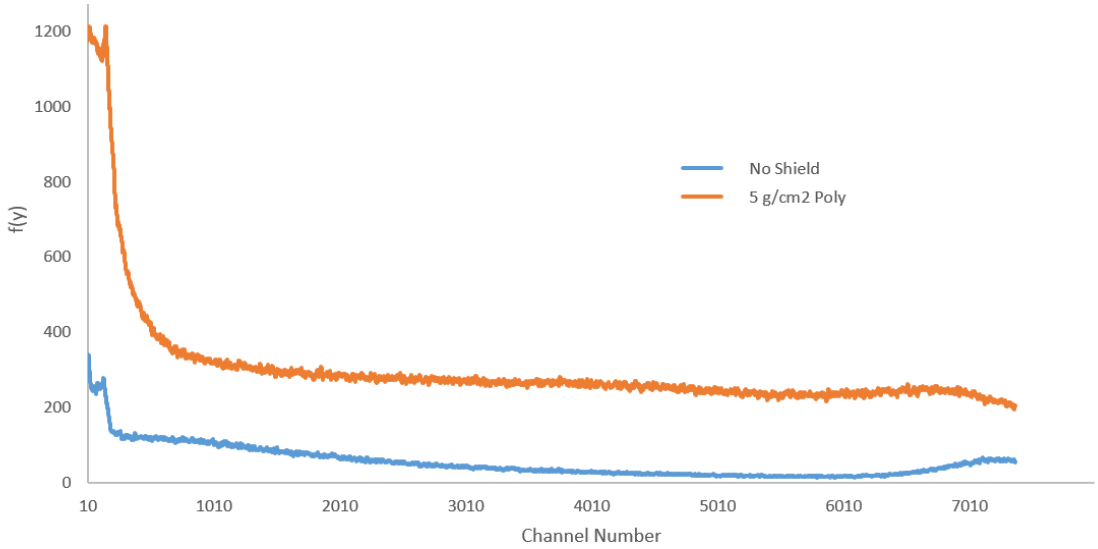


Figure 6.2: Lin-Lin plot of the Acrylic detector head exposures at LANSCE as measured by an ATED prototype.

*6.2 Japan February 2017*

This experiment takes place at the HIMAC heavy ion accelerator in Chiba, Japan. Time on four separate beams is granted for this experiment: 6 hours on 400 MeV/nucleon neon, 2 hours on 70 MeV protons, 6 hours on 500 MeV/nucleon iron, 6 hours on 400 MeV/nucleon carbon. Gain settings were adjusted on the amplifier circuit by adjusting the fine gain of the shaping amplifier throughout the experiment to find the optimal settings for gain. Two detector heads were used at different times throughout the beam exposures to ensure there was a backup in case of failure in one of the detector heads. The figures show measurements taken by only one of the detector heads because of the redundancy.

*6.2.1 70 MeV Protons*

Figure 6.3 shows normalized *f(y)* and *y*f(y)* spectra for a 70 MeV proton beam as measured by an ATED prototype at HIMAC heavy ion accelerator. The proton edge is apparent in the *y*f(y)* representation of the Log-Log plot. There is no signal below 6 keV/µm because there was a threshold setting used in the spectrometer which did not allow signals this low in lineal energy to be measured.

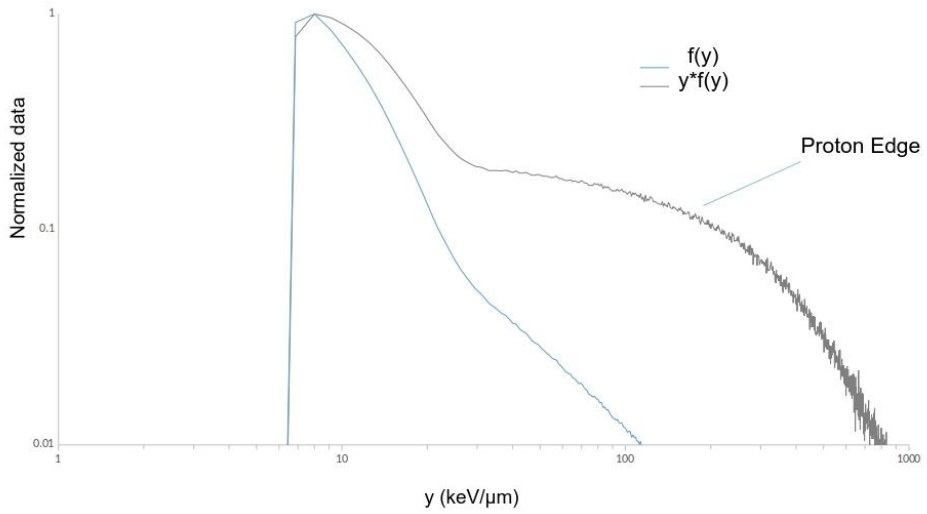


Figure 6.3: Log-Log Normalized 70 MeV proton beam lineal energy as measured by an ATED prototype.

Figure 6.4 shows the spectra of normalized counts as a function of channel number from the amplifier characterization portion of the proton measurement experiment. The results were measured after turning the fine gain potentiometer 360 degrees between measurements. The leading edge of the spectrum moved in channel number to the right as amplification was increased in the shaping amplifier.

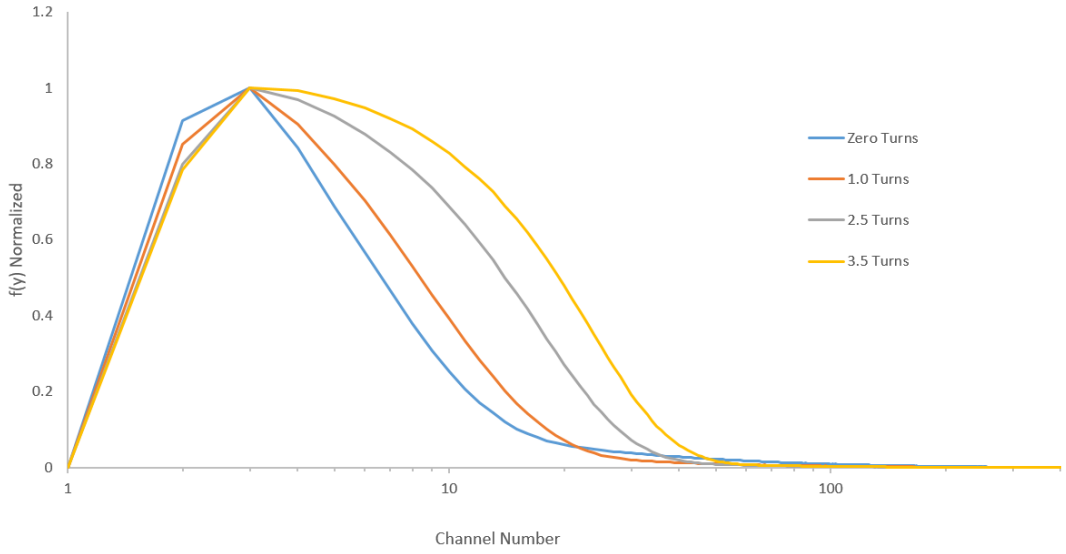


Figure 6.4: 70 MeV proton amplification settings as measured by an ATED prototype.

### *6.2.2 387 MeV Carbon*

Figure 6.5 shows the normalized *f(y), y*D(y),* and *y*f(y)* vs. lineal energy spectra. The high count rates at low lineal energy contribute a relatively low absorbed dose when compared to the counts at higher channel numbers; absorbed dose per incident particle increases as a linear function in lineal energy.

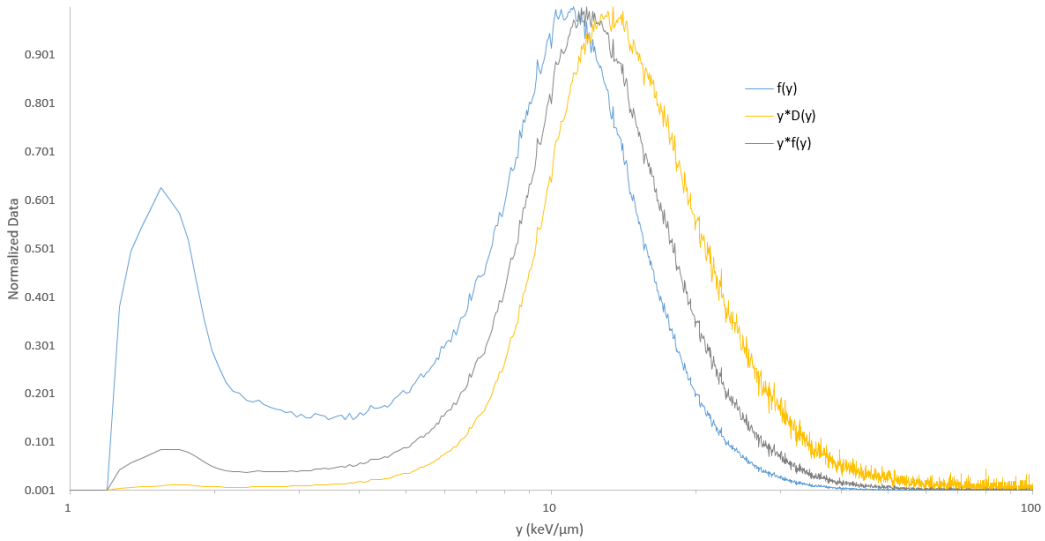


Figure 6.5: 387 MeV Carbon lineal energy as measured by an ATED prototype.

Figure 6.6 shows 387 MeV carbon *f(y)* spectra measurements made by an ATED prototype. The resulting lineal energy spectra of the beam were measured after traveling through three thicknesses of water equivalent binary filter. The beam was slowed down as it traversed the filter. The slowing down of the beam is indicated by the peak of the spectrum shifting to higher lineal energies as the beam passes through a thicker absorber. Fragmentation also occurs as a result of the beam traversing the binary filter. Some of the secondary particles are measured as lower lineal energy measurements; the counts increase in the low lineal energy region of the spectra with increasing thickness of the binary filter.

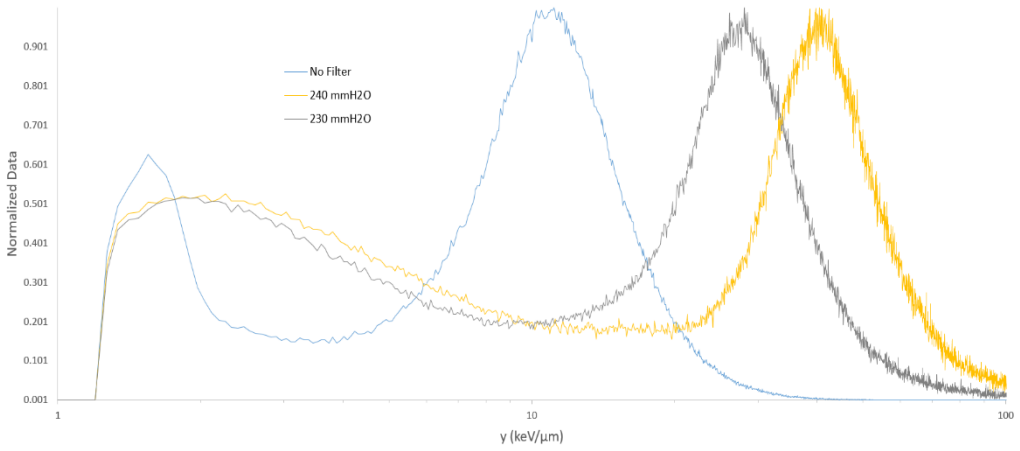


Figure 6.6: 387 MeV Carbon *f(y)* versus *y* for three thicknesses of the binary filter as measured by an ATED prototype.

### *6.2.3 370 MeV Neon*

Figure 6.7 shows the normalized *f(y), y*D(y),* and *y*f(y)* vs. lineal energy spectra. The high count rates at low lineal energy contribute a relatively low absorbed dose

when compared to the counts at higher channel numbers; absorbed dose per incident particle increases as a linear function in lineal energy.

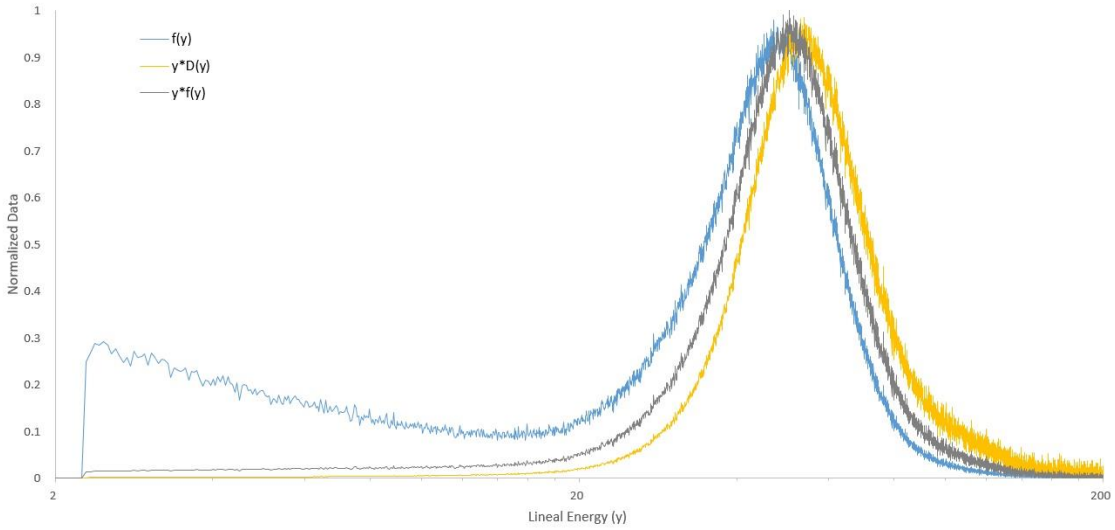


Figure 6.7: 370 MeV Neon lineal energy as measured by an ATED prototype.

Figure 6.8 shows 370 MeV neon *f(y)* spectra measurements made by an ATED prototype. The resulting lineal energy spectra of the beam were measured after traveling through three thicknesses of water equivalent binary filter. The beam was slowed down as it traversed the filter. The slowing down of the beam is indicated by the peak of the spectrum shifting to higher lineal energies as the beam passes through a thicker absorber. Fragmentation also occurs as a result of the beam traversing the binary filter. Some of the secondary particles were measured as lower lineal energy measurements; the counts increase in the low lineal energy region of the spectra with increasing thickness of the binary filter.

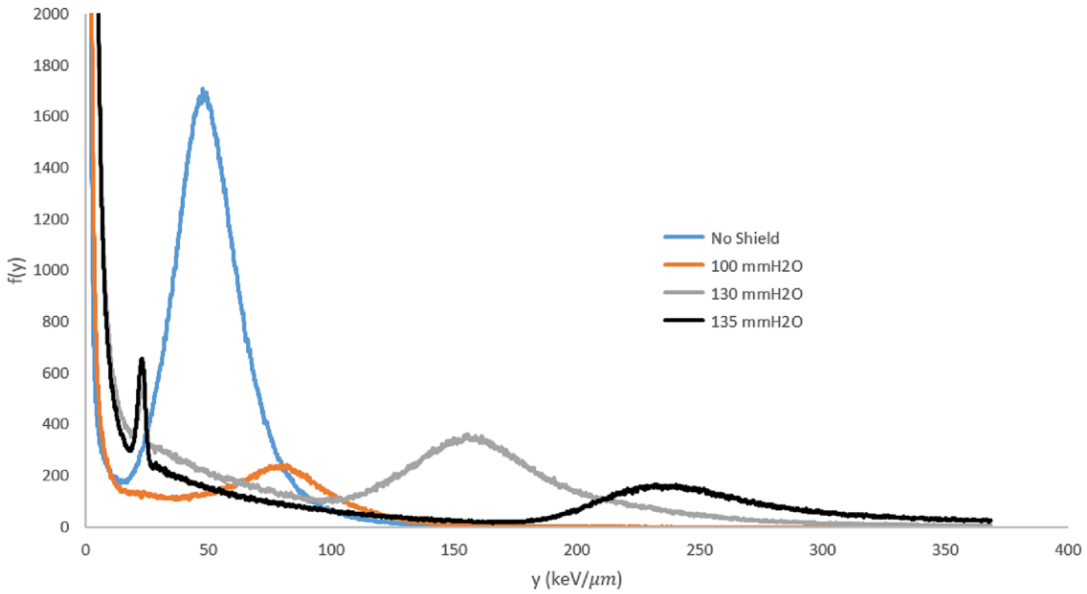


Figure 6.8: 370 MeV Neon f(y) versus y for three thicknesses of the binary filter as measured by an ATED prototype.

### *6.2.4 500 MeV Iron*

Figure 6.9 shows the normalized counts as a function of channel number spectra from the amplifier characterization portion of the 422 MeV iron measurement experiment. The measurements were taken after turning the fine gain potentiometer 360 degrees between measurements. The peak of the spectrum moved in channel number to the right as amplification was increased in the shaping amplifier.

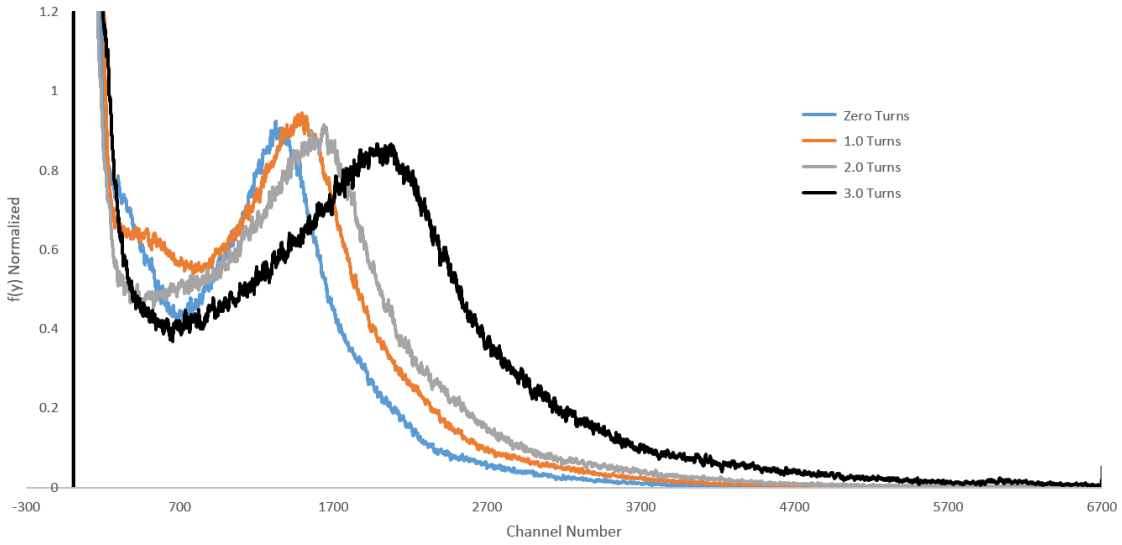


Figure 6.9: 70 MeV proton amplification settings as measured by an ATED prototype.

## *6.3 Japan June 2017*

This experiment took place at the HIMAC heavy ion accelerator in Chiba, Japan. Two detector heads were used at different times throughout the experiments. Time on four separate beams was used for this experiment: 6 hours on 443 MeV silicon, 143 MeV helium, 30 minutes on 387 MeV carbon, 6 hours on 422 MeV iron. The goal of this experiment was to show ATED operates as a dosimeter by measuring absorbed dose and dose equivalent from bare beam exposures.

### *6.3.1 Bare Beam Dosimetric Measurements*

Tables 6.1 and 6.2 show the results of bare beam measurements using detector head #3 and detector head #2, respectively. The helium beam absorbed dose measurements are significantly below the calculated results for absorbed dose. The discrepency between measurement and calculation is because the low-level threshold for accepted signals was set to approximately 6 keV/µm; only the front edge of the spectra

peak is counted in the dosimetric measurement of low lineal energy particles. The ATED model that is currently on ISS has a low-level threshold of approximately 1 keV/µm. The new low-level threshold will correct the issue with absorbed dose measurements of particles with low lineal energy.

The rest of the discrepancies were likely caused by how the absorbed dose and dose equivalent were calculated. The calculations were made with the assumption that each particle has the same energy and that no secondaries contribute to the absorbed dose or the dose equivalent. Many of the calculated absorbed dose calculations are within the uncertainty of the measurements. The measured data are trusted because of the extensive calibration and characterization of ATED.

| Ion | Lineal Energy (keV/µm) | Measured Absorbed Dose (µGy) | Calculated Absorbed Dose (µGy) | Measured Dose Equivalent (µSv) | Calculated Dose Equivalent (µSv) |
|---|---|---|---|---|---|
| 142.8 MeV Helium | 3.39 | 29. ± 2.4 | 60. | 74. ± 6.2 | 60. |
| 142.8 MeV Helium | 3.39 | 28. ± 2.3 | 49. | 79. ± 6.6 | 49. |
| 142.8 MeV Helium | 3.39 | 23. ± 1.9 | 39. | 62. ± 5.2 | 39. |
| 387 MeV Carbon | 16.8 | 530 ± 45. | 430 | 3300 ± 280 | 1400 |
| 443 MeV Silicon | 85.7 | 940 ± 79. | 920 | 26000 ± 2200 | 2900 |
| 443 MeV Silicon | 85.7 | 810 ± 68. | 700 | 22000 ± 1800 | 2200 |
| 443 MeV Silicon | 85.7 | 700 ± 59. | 640 | 19000 ± 1600 | 2000 |
| 422 MeV Iron | 303 | 3400 ± 280 | 3200 | 57000 ± 4800 | 56000 |
| 422 MeV Iron | 303 | 3300 ± 280 | 3300 | 57000 ± 4800 | 56000 |
| 422 MeV Iron | 303 | 3200 ± 270 | 3100 | 54000 ± 4600 | 53000 |

Table 6.1: Detector Head #3 Dosimetric Data June 2017

| Ion | Lineal Energy (keV/μm) | Run | Measured Absorbed Dose (μGy) | Calculated Absorbed Dose (μGy) | Measured Dose Equivalent (μSv) | Calculated Dose Equivalent (μSv) |
|---|---|---|---|---|---|---|
| 142.8 MeV Helium | 3.39 | 1 | 160. ± 13. | 220 | 290 ± 25. | 220 |
| 142.8 MeV Helium | 3.39 | 2 | 54. ± 4.6 | 73 | 98. ± 8.3 | 73 |
| 142.8 MeV Helium | 3.39 | 3 | 44 ± 3.7 | 59 | 86 ± 7.2 | 59 |
| 387 MeV Carbon | 16.8 | 1 | 520 ± 44. | 370 | 1700 ± 140 | 510 |
| 443 MeV Silicon | 85.7 | 1 | 1400 ± 110 | 830 | 16000 ± 1300 | 13000 |
| 443 MeV Silicon | 85.7 | 2 | 1200 ± 100 | 770 | 15000 ± 1200 | 12000 |
| 422 MeV Iron | 303 | 1 | 3400 ± 280 | 3600 | 77000 ± 6500 | 76000 |
| 422 MeV Iron | 303 | 2 | 3600 ± 300 | 4000 | 83000 ± 6900 | 84000 |
| 422 MeV Iron | 303 | 3 | 3500 ± 290 | 3700 | 80000 ± 6700 | 79000 |

Table 6.2: Detector Head #2 Dosimetric Data June 2017

*6.4 Calibration of ATED using Neutron Source and Gamma Ray Sources*

Two other calibration techniques were tested: 1) measuring the proton edge and electron edge using a neutron source, 2) measuring the proton edge with a neutron source and measuring the electron edge using gamma ray sources. The first method proved to be inaccurate because of the superposition of signals near the electron edge from low lineal energy particles that were not electrons. The second method removes the impracticalities associated with taking TEPC to particle accelerators.

ATED calibration using a PuBe neutron source to find the proton edge and gamma ray sources to find the electron edge. This method yields nearly identical results

to calibrating ATED using mono-energetic beams at particles accelerators. It may seem sufficient to use only the proton edge to calibrate the unit. However, an improper calibration will go unnoticed if the baseline DC offset of a TEPC is not properly set to zero and only a single point is used to calibrate the device.

There are two solutions to the DC offset problem. Someone that is not hardware inclined can adjust the spectrum calculations to account for the DC offset problem. Alternatively, a hardware technician can perform the other solution: adjust the DC offset in the analog signal. These solutions are not possible if the DC offset goes unnoticed as is possible with the one-point proton edge calibration.

*6.5 ISS Measurements*

Measurements began July 13, 2018 on the ISS. The first data downlink of measurements from the station occurred on July 19, 2018. Figures 6.10 and 6.11 are the representative spectra of the measurements made on the ISS in LEO.

Figure 6.10 shows 24 hour measurements of counts versus lineal energy. Figure 6.11 shows the *y*f(y) versus lineal energy* for the same 24 hour periods represented in Figure 6.10. The first three 24 hour measurements have counts that are two orders of magnitude higher than the later measurements. The higher count rates in the first days has two possible causes: either the ISS spent more time traveling through the SAA on the earlier measurements or the detector is in a transitional stage of stabilization. The cause for the large disparity in counts will be decided once location data for the ISS is obtained.

The data shows that most of the absorbed dose in LEO is from particles with low lineal energy. There are also more rare events in the higher lineal energy region of the

spectra. These are qualitative characteristics that are expected in measurements in LEO on ISS. A quantitative analysis of the data will yield many more details about the phenomena causing the absorbed doses.

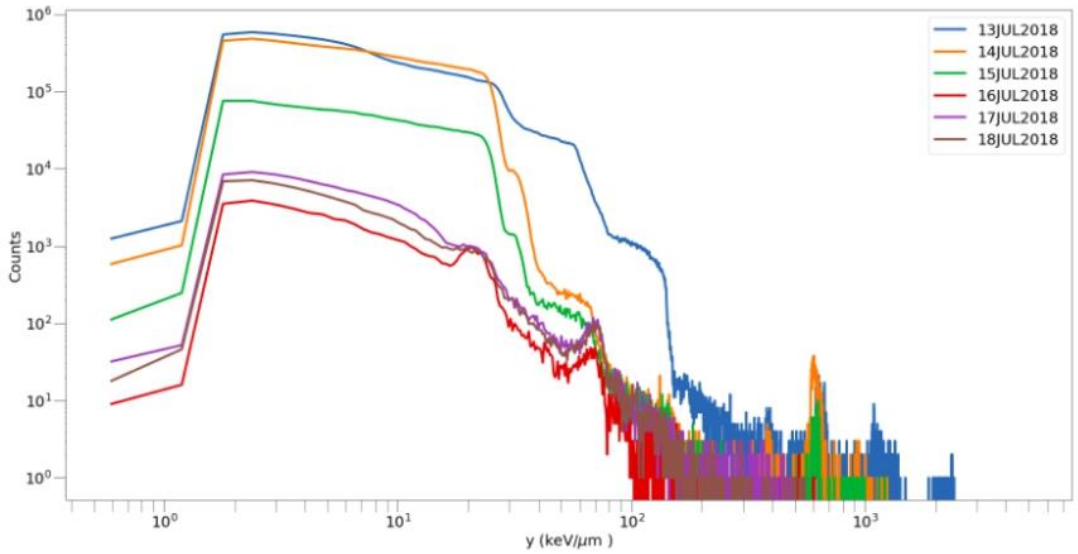


Figure 6.10 Counts versus lineal energy for 24 hour periods on ISS in LEO.

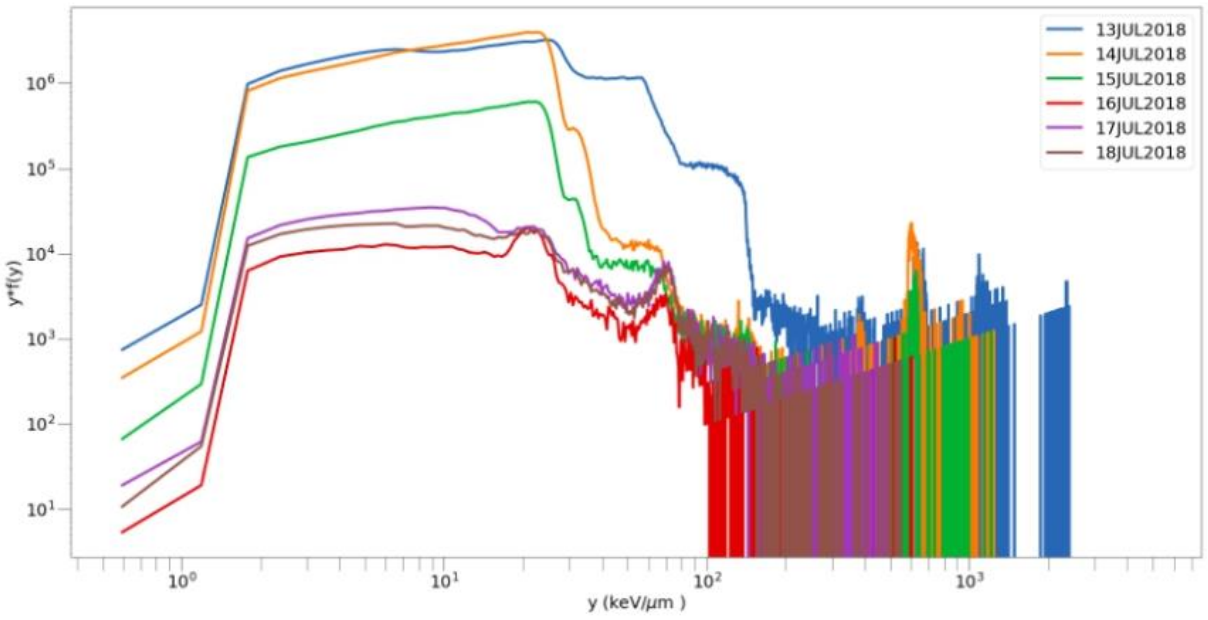


Figure 6.11 y*f(y) versus lineal energy for 24 hour periods on the ISS in LEO

*6.6 Future Work*

ATED's ability to measure particles ranging from ultra-low to high lineal energies is exciting. The data from the ISS experiment will help to answer some interesting scientific questions. The measurements will help us understand the absorbed dose rates at high latitudes from electrons in the magnetic cusps of Earth. ATED will also measure the effects of local shielding environments on absorbed dose rates on ISS.

After the ISS measurements, future models of TEPC will be produced to take measurements at aircraft altitude. Taking measurements in aircraft can address the possible high absorbed dose rates claimed to be associated with SPE and TGF.

ATED has some limitations that need addressing for future models of TEPC. Future TEPC should include two shaping amplifiers that produce two spectra. The two signals will have two different gains. The two gains increase the range of energies that can be measured thus allowing for measurement of particles with an increased range of lineal energies. A new spectrometer will be needed because ATED's current spectrometer only has one analog input. There are many options for replacing the spectrometer. An easy option is to replace the unit with a COTS spectrometer that has two analog inputs.

Designing a low-pass filter to eliminate noise due to transient signals would allow for measurements of particles with lower lineal energy than ATED is currently capable of measuring. The topology in some COTS low-pass filters is not compatible with use in ATED. ATED's signals are peaks that sit on sinusoidal noise. Designing a low-pass filter

that correctly handles this type of signal can yield at least another order magnitude of measurements at the low end of the spectrum.

It might be more useful to replace the spectrometer with a Field Programmable Gate Array (FPGA). An FPGA spectrometer will reduce the overall cost of ATED by more than half. Also, programming the FPGA allows for better control of how signals are converted from analog to digital. This control ensures higher confidence in measured data.

# REFERENCES


[Arimoto 2018] Arimoto, M., et al. (2018). “Development of a 32-channel ASIC for an X-ray Detector onboard the ISS.” Nuclear Instrumentation and Methods in Physics Research 882

[Badavi 2011] Badavi, F. F., et al. (2011). “The Low Earth Orbit validation of a dynamic and anisotropic trapped radiation model through ISS measurements.” Advances in Space Research 48: 8

[Badhwar 1997] Badhwar, G. D. (1997), “The radiation environment in low-Earth orbit.” *Rad. Res.* 148 S3-S10.

[Badhwar 2001] Badhwar, G. D., et al. (2001). “Validation of the galactic cosmic ray and geomagnetic transmission models.” Radiation Measurements 33: 3

[Badhwar 2002] Badhwar, G. D. (2002). "Shuttle radiation dose measurements in the international space station orbits." Radiation Research Society 157(1): 7.

[Benjamin 1968] Benjamin, P. W. e. a. (1968). "A high Resolution Spherical Proportional Counter." Nuclear Instruments and Methods 59: 9.

[Benton 2001] Benton, E. R. et al. (2001). "Space Radiation Dosimetry in low-Earth orbit and beyond." Nuclear Instruments and Methods in Physics Research B 184: 40.

[Benton 2004] Benton, E. R. (2004). “Radiation Dosimetry at Aviation Altitudes and in Low-Earth Orbit.” Ph.D. Dissertation. The National University of Ireland

[Berger 2017] Berger, T., et al. (2017). “DOSIS & DOSIS 3D: radiation measurements with the DOSTEL instruments onboard the Columbus Laboratory of the ISS in the years 2009-2016.” Journal of Space Weather and Space Climate 7

[Boag 1966] Boag, J. W., (1966). “Ionization Chambers.” Radiation Dosimetry II. Academic Press Inc.

[Braby 1985] Braby, L.A. (1985) “Portable dose equivalent meter based on microdosimetric techniques.” Nuclear Instrumentation and Methods 10-11

[Braby 2001] Braby, L.A., Badhwar, G.D. (2001) “Proportional counter as neutron Detector.” Radiation Measurements 33

[Brackenbush 1990] Brackenbush, L. W. (1990). "Using Tissue Equivalent Proportional Counters to Determine Dose Equivalent."

[Candidi 1984] Candidi, M., Meng, C. (1984) “Nearly simultaneous observations of the conjugate polar cusp regions.”

[Collums 2012] Collums, T. (2012). Comparison of Plastics Used in Tissue Equivalent Proportional Counter (TEPC) and Development of a Balloon Borne TEPC. Ph.D., Oklahoma State University.

[Cronin 1997] Cronin J.W., et al. (1997). "Cosmic Rays at the Energy Frontier." Scientific American: 6.

[Daglis 2007] Daglis, V. B. a. I. A. (2007). “Space Weather Physics and Effects.” Springer

[Dachev 2017] Dachev, T.P., et al., (2017). “Overview of the ISS Radiation Environment Observed during the ESA EXPOSE-R2 Mission in 2014-2016.” Space Weather 15:11

[DeWitt 2011] DeWitt, J. (2011). “Radiation Shielding for Future Space Exploration Missions.” Ph.D. Dissertation. Oklahoma State University.

[Dwyer 2005] Dwyer, J., Smith, D. (2005). “A Comparison between Monte Carlo simulations of runaway breakdown and Terrestrial Gamma-Ray Flash Observations.” Geophysical Research Letters 32

[Dwyer 2010] Dwyer, J., et al. (2010). “Estimation of the fluence of high-energy electron bursts produced by thunderclouds and the resulting radiation doses received in aircraft.” Journal of Geophysical Research 115

[FAA 2017] FAA (2017). https://www.faa.gov/air_traffic/by_the_numbers/media/Air_Traffic_by_the_Numbers_2017_Final.pdf

[Fatemah 2017] Fatemah R. et al. (2017). “Inferring the Heliospheric Magnetic Field Back through Maunder Minimum.” The Astrophysical Journal 837: 2

[Fennel 2015] Fennell, J., Claudepierre, et al. (2015). “Van Allen Probes show that the inner radiation zone contains no MeV electrons: ECT/MagEIS data.” Geophysical Research Letters, 42: 2

[Fry 1989] Fry, R.J.M (1989). “Risk assessment and late effects of radiation in low-earth orbits.” Symposium on radiation hazards in space and biological consequences 1989.

[Gersey 2018] Gersey, B. (2018, April 5). Personal Interview.

[Golding 2005] Golding, W.L. (2005). “Lightning Strikes on Commercial Aircraft: How the Airlines Are Coping.” Journal of Aviation/Aerospace Education & Research 15:1

[Gjesteland 2010] Gjesteland, T., et al. (2010). “Effects of dead time losses on terrestrial gamma ray flash measurements with the Burst and Transient Source Experiment.” Journal of Geophysical Research 115

[Grefenstette 2008] Grefenstette, B., et al. (2008). “Time evolution of terrestrial gamma ray flashes.” Geophysical Research Letters 35

[Howard 2014] Howard, T. (2014). “Space Weather and Coronal Mass Ejections.” Springer.

[ICRP60 1991] ICRP60 (1991). “1990 Recommendations of the ICRP.” International Commission on Radiological Protection.

[ICRP103 2007] ICRP103 (2007). “The 2007 Recommendations of the International Commission on Radiological Protection.” International Commission on Radiological Protection.

[ICRU28 1978] ICRU28 (1978). ”Basic Aspects of High Energy Particle Interactions and Radiation Dosimetry.” International Committee on Radiation Units and Measurements.

[ICRU36 1985] ICRU36 (1985). “Microdosimetry.” International Committee on Radiation Units and Measurements.

[ICRU85 2011] ICRU85 (2011). "Fundamental Quantities and Units for Ionizing Radiation.” International Committee on Radiation Units and Measurements.

[Kline 1985] Kline, S.J. (1985) “The Purposes of Uncertainty Analysis.” Journal of Fluids Engineering 107

[Kosterev 2016] Kosterev, V.V. et al. (2016) “Worker Radiation Exposure.” Atomic Energy 120: 2

[Kroupa 2015] Kroupa, M., et al. (2015). “A semiconductor radiation imaging pixel detector for space radiation dosimetry.” Life Science in Space Research 6

[Lucas 2018] Lucas, A., (2018, January). Personal Interview.

[Lugaz 2016] Lugaz, N., et al. (2016) “Earth’s magnetosphere and outer radiation belt under sub-Alfvenic Solar Wind.” Nature Communications 7

[Mcelroy 1975] Mcelroy, M. B., Noll, R. B. (1975). “The earth’s trapped radiation belts.” NASA-SP-8116

[Moro 2015] Moro, D. et al. (2015) “Lineal energy calibration of a spherical TEPC.” Radiation Protection Dosimetry 166

[NASA 2006] NASA (2006) https://www.nasa.gov/mission_pages/themis/auroras/sun_earth_connect.html

[NASA 2011] NASA (2011) https://www.nasa.gov/mission_pages/station/expeditions/expedition26/iss_altitude.html

[NCRP98 1989] NCRP 98 (1989) “Guidance on Radiation Received in Space Activities.” National Council on Radiation Protection and Measurements.

[NCRP116 1993] NCRP 116 (1993) “Limitation of Exposure to Ionizing Radiation National Council on Radiation Protection (1993)

[Pinsky 2014] Pinsky, L.S., et al. (2014). “Medipix in space on-board the ISS.” Journal of Radiation Research 55: 1

[Reames 2017] Reames, D. V. (2017). “Solar Energetic Particles.” Springer.

[Reedy 1996] Reedy, R. (1996). “Constraints on solar particle events from comparisons of recent events and million-year averages,” Proceedings of the National Solar Observatory/Sacramento Peak 16th International Workshop on Solar Drivers of Interplanetary and Terrestrial Disturbances

[Reitz 1993] Reitz, G., et al. (1993). “Radiation Protection Dosimetry: Radiation Exposure of Civil Aircrew.” Nuclear Technology Publishing 48:1

[Rossi 1996] Rossi, H.H., Zaider, M. (1996) “Microdosimetry and Its Applications.” Springer

[Schwadron 2017] Schwadron, N. A., et al. (2017). "Particle Radiation Sources, Propagation and Interactions in Deep Space, at Earth, the Moon, Mars, and Beyond: Examples of Radiation Interactions and Effects." Space Science Reviews 212(3-4)

[Shcherbakov 2015] Shcherbakov, V., et al. (2015). “On the distribution function of the geomagnetic field intensity according to the model of a giant Gaussian process and empirical data.” Physics of the Solid Earth 51:5

[SIDC 2015] SIDC (2015). “sidc.be/news/269/welcome/html”

[Smart 2006] Smart, D.F., et al. (2006). “A geomagnetic cutoff rigidity interpolation tool: Accuracy verification and application to space weather.” Advances in Space Research 37: 6

[Smart 2009] Smart, D.F, et al. (2009). “Fifty years of progress in geomagnetic cutoff rigidity determinations.” Advances in Space Research 44

[Smith 2016] Smith, M.B., et al. (2016). “Bubble-detector measurements of neutron radiation in the international space station: ISS-24 to ISS-37.” Radiation Protection Dosimetry 168: 2

[Srag 2016] Srag. (2016). https://srag.jsc.nasa.gov/spaceradiation/What/What.cfm

[Turner 2000] Turner, R. (2000). "Solar particle events from a risk management perspective.” IEEE *Transactions on Plasma Science*, 28: 6

[Svanto 2015] Svanto, P., et al. (2015). “Onboard cross-calibration of the Pille-ISS Detector System and measurement of radiation shielding effect of the water filled protective curtain in the ISS crew cabin.” Radiation Measurements 82

[Tobiska 2014] Tobiska, K.W., et al. (2014). “U.S. Government shutdown degrades aviation radiation monitoring during solar radiation storm.” Space Weather 12: 1

[Tsoulfanidis 1972] Tsoulfanidis, N. (1972). “Measurement and Detection of Radiation.” Hemisphere Publishing Corporation.

[Van Allen 1959] Van Allen, J. A. (1959) “Radiation Belts around the Earth.” Scientific American 200: 3

[Wilson 1997] Wilson, J. W., et al. (1997). "Shielding Strategies for Human Space Exploration." NASA Conference Publication 3360: 493.

[Zaconte 2010] Zaconte, V., et al. (2010). “High energy radiation fluences in the ISS-USLab: Ion discrimination and particle abundances.” Radiation Measurements 45: 2

[Zhao 2014] Zhao, L. L., et al. (2014). “Modulation of galactic cosmic rays during the unusual solar minimum between cycles 23 and 24.” Journal of Geophysical Research: Space Physics 119: 3

VITA

Oliver Ian Causey

Candidate for the Degree of

Doctor of Philosophy

Thesis: ACTIVE TISSUE EQUIVALENT DOSIMETER: DEVELOPMENT OF A DOSIMETER FOR THE INTERNATIONAL SPACE STATION

Major Field: Physics

Biographical:

Education:

Completed the requirements for the Doctor of Philosophy in Physics at Oklahoma State University, Stillwater, Oklahoma in July, 2018.

Completed the requirements for the Bachelor of Science in Physics at The University of Tulsa, Tulsa, OK in 2014.